Magnetotransport Studies of Iron-Pnictide Superconductors

A thesis
submitted in partial fulfillment of the requirements
for the degree of

DOCTOR OF PHILOSOPHY

by

Rohit Kumar

Roll No.: 20123226

IISER PUNE

Indian Institute of Science Education and Research
Pune - 411008. India

2018

December, 2018

CERTIFICATE OF THE SUPERVISOR

Certified that the work incorporated in the thesis entitled "**Magnetotransport Studies of Iron-Pnictide Superconductors**", submitted by **Rohit Kumar** was carried out by the candidate, under my supervision. The work presented here or any part of it has not been included in any other thesis submitted previously for the award of any degree or diploma from any other University or institution.

Pune
Date: December 31, 2018

Dr. Sunil Nair
(Supervisor)

CERTIFICATE OF THE SUPERVISOR

Certified that the work incorporated in the thesis entitled "**Magnetotransport Studies of Iron-Pnictide Superconductors**", submitted by **Rohit Kumar** was carried out by the candidate, under my supervision. The work presented here or any part of it has not been included in any other thesis submitted previously for the award of any degree or diploma from any other University or institution.

Pune
Date: December 31, 2018

Dr. Surjeet Singh
(Co-supervisor)

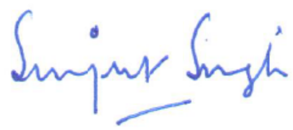

DECLARATION BY THE CANDIDATE

I declare that this written submission represents my ideas in my own words and where other's ideas have been included, I have adequately cited and referenced the original sources. I also declare that I have adhered to all principles of academic honesty and integrity and have not misrepresented or fabricated or falsified any idea/data/fact/source in my submission. I understand that violation of the above will be cause for disciplinary action by the Institute and can also evoke penal action from the sources which have thus not been properly cited or from whom proper permission has not been taken when needed.

Pune
Date: December 31, 2018

Rohit Kumar

Dedicated to the loving memory of my beloved grandmother

Acknowledgemnts

It gives me immense pleasure to acknowledge the following individuals who have been a part of this long, arduous journey.

First and foremost, I would like to express my sincere gratitude for my thesis supervisors; Dr. Sunil Nair and Dr. Surjeet Singh. During this long Journey, Sunil has been very encouraging, patient and supportive. He taught me a great deal, be it how to write scientific papers or, approach a difficult problem. His insights on the magnetotransport in strongly correlated electron systems (but not limited to) have had a profound impact on me, and I wish to continue to draw from his vast knowledge store. The lessons I learned from him, both on a personal and academic level, will be my guiding principles in the years to come.

Also, it is my distinct pleasure to acknowledge my thesis supervisor Dr. Surjeet Singh. He introduced me to the ABCs of research. I still remember, when he 'himself' for the time showed me how to seal a quartz ampoule, how to make contacts for transport measurements, how to extract single crystals and the list goes on. He introduced me to many experimental techniques I know today, but also kept a healthy distance so that I can also learn to think critically. However, most of all, I thank him for believing in me.

I thank Dr. Luminita Harnagea for important tips and suggestions about single crystal growth, and the physics of iron-based superconductors in general. I also thank her for providing me with the high-quality single crystals of several iron-based superconductors.

I would like to thank my research advisory committee members; Dr. Arijit Bhattacharyay and Dr. Aparna Deshpande for their important suggestions over the years. Dr. Arijit Bhattacharyay has been particularly helpful and encouraging in his efforts as a research advisor.

I would like to thank Dr. Archana Lakhani for support during the magnetotransport measurements at IUC, Indore.

Also, I would like to thank Dr. Mukul Kabir, for his exceptional teaching efforts in the advanced condensed matter physics course. The concepts he taught us has been very useful in my Ph.D. research and understanding of condensed matter physics in general.

It is my pleasure to acknowledge my lab members, past and present; Jitender, Shruti K., Rabindra, Prachi, Dibyata, Deepak, Devarajan, Devika TD, Devika VS, Shruti Chakravarty, Kaustav, Giri, Avirup, Ashoka, Arup, Koushik, Pravu Prasad Dhal, Saurabh, Vignesh, Vikram, Anupam, Kshiti, Shanu, Panja, and Charu.

Also, I would like to thank the technical staff at IISER Pune, especially Nilesh Dumbre, Prashant Kale, Yathish, Parveen Nasa and Anil Shetty for their support in different measurements and services to the physics department in general. I am also thankful to the physics office members; Prabhakar Anagare, Dhanashree Sheth, Kalpesh Pednekar, and Tushar Kurulkar for their help on several occasions. I also thank IISER administration, library, transport, housekeeping, and security staff.

Special thanks to Jitender for his continuous support and motivation at all fronts of life. He has been a good friend and my well-wisher. His presence at IISER made my life easy and cheerful.

Also, it is my pleasure to acknowledge my dearest friends at IISER, who has been incredibly supportive and encouraging, without whom this journey would not have been so incredible. Special thanks to Jitender, Rakesh, Satish, Sachin, Rishabh, Manu, Mohit, Jagadeeswararao, Pravin and Aman. We had spent an incredible amount of time together in IISER, be it late night tea sessions, Pune Darshan, visiting a fort or a museum, or the Osho Garden, late-night trekking, watching movies, celebrating Holy, cooking, the list goes on. I will have a special place for these people in my heart and will have many memories to carry with me.

I would also like to thank my friends Amandeep, Avdhoot, Rohit Babar, Sanku, Kunal, Shishir, Namrata, Ravi Prakash Nath, Aditi and Harshini for support and encouragement.

I would like to take this opportunity to thank my mother, for her patience, support, and love. Also, I would like to thank my brother Ankit, for his support and encouragement. Also, I would like to extend my sincere thanks to my uncle Satendra Singh and Pushpendra Singh for their support and care.

I would like to thank my grandfather, for his immense support throughout my life. I wish to live up to his expectations. Also, I would like to thank, Anuruti, Upendra and Shweta, for their patience and encouragement.

Also, I would like to thank little ones at home; Avi and Disha. I wish I had spent more time with them, and be a part of their childhood memories.

Finally, I would like to thank the entire IISER community for being nice and creating a healthy and nurturing environment. Sweet memories of this great institution will always be with me.

Two roads diverged in a yellow wood,
And sorry I could not travel both
And be one traveler, long I stood
And looked down one as far as I could
To where it bent in the undergrowth;

Then took the other, as just as fair,
And having perhaps the better claim,
Because it was grassy and wanted wear;
Though as for that the passing there
Had worn them really about the same,

And both that morning equally lay
In leaves no step had trodden black.
Oh, I kept the first for another day!
Yet knowing how way leads on to way,
I doubted if I should ever come back.

I shall be telling this with a sigh
Somewhere ages and ages hence:
Two roads diverged in a wood, and I,
I took the one less travelled by,
And that has made all the difference.

– Robert Frost
In, The Road Not Taken

Contents

List of Figures

List of Tables

Chapter 1

Introduction

Superconductivity is the phenomena where the resistance of a material vanishes at a critical temperature (T_C), and the magnetic field is expelled from its bulk below this temperature [10]. Superconductivity was discovered by Dutch Physicist Heike Kamerlingh Onnes in the element Mercury in 1911 [11]. The second integral component of superconductivity, the Meissner effect was discovered 23 years later in 1933 by the German physicists Walther Meissner and Robert Ochsenfeld [10]. Since then, a large number of metals and compounds were found to harbor a superconducting ground state [1] among which high-T_C cuprates, heavy fermions and the iron-based superconductors (FeSCs) are some of the most studied classes of superconducting materials.

Superconducting materials can be broadly classified as conventional and unconventional superconductors [1, 12]. Most elemental superconductors and many complex compounds can be considered as conventional superconductors and can be successfully described by the BCS theory (named after its inventors John Bardeen, Leon Cooper, and John Robert Schrieffer) of superconductivity and its extensions. In BCS theory, the pairing between electrons is mediated by the quantized lattice vibrations, i.e., the phonons. Also, the symmetry of the superconducting order parameter of the conventional BCS type superconductors is of 's' wave type. 's' wave order parameter is spherically symmetric, does not have any nodes, and the Cooper pairs carry zero angular momentum. Conventional superconductors have low T_C's, for example, the maximum T_C observed in any conventional superconductor so far (in MgB_2) is $\sim$ 40 K [13]. In unconventional superconductors (also called non-BCS superconductors), the pairing between the electrons is thought to be mediated by mechanism more exotic than lattice vibrations, e.g., spin fluctuations. Also, any superconductor having a non 's' wave order parameter (p wave, d wave or s^{+-} wave type) is generally considered an unconventional

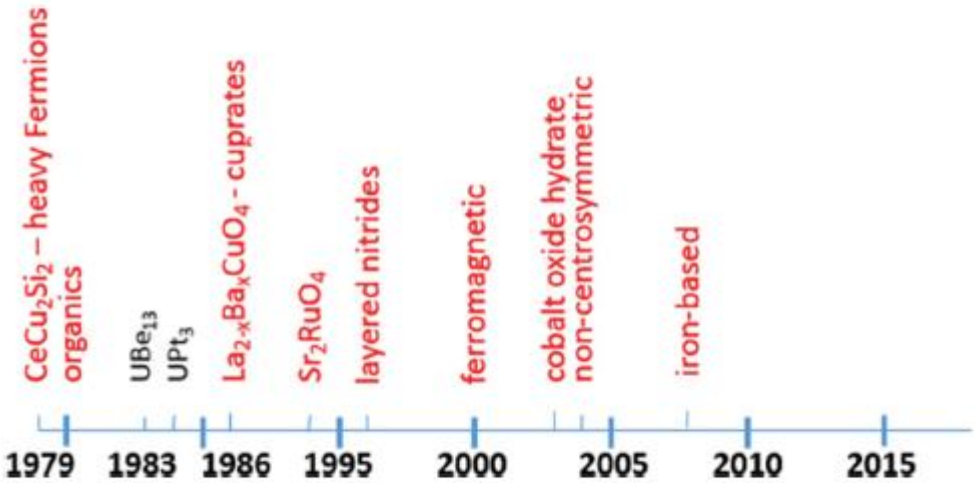

Figure 1.1: Some unconventional superconductors are listed according to the time of their discovery. Figure Courtesy: Taylor & Francis Group, reprinted from [1].

superconductor. Heavy fermions, high-T_C cuprates, iron-based superconductors, and organic superconductors are some of the most remarkable unconventional superconductors. The record of highest T_C amongst all superconductors known to date is held by a cuprate $HgBa_2Ca_2Cu_3O_{8+x}$ being $\sim$135 K at ambient pressure [14]. In Figure1.1, many classes of unconventional superconductors are listed according to the time of their discovery (taken from reference [1]). The first unconventional superconductor $CeCu_2Si_2$ ($T_C \approx 0.6$ K), a heavy fermion system, was discovered by F. Steglich in 1979. A recent addition to the list of unconventional superconductors are the iron-based superconductors. It should be noted that the list of unconventional superconductors in Figure 1.1 is not comprehensive and some (e.g., topological superconductors) have not been included.

The first iron-based superconductor; LaOFeP ($T_C \sim 4$ K) was discovered in 2006 by Kamihara and co-workers [15]. This discovery did not get much attention until 2008 when superconductivity at $\approx$ 26 K in a related system $LaO_{1-x}O_xFeAs$ was discovered by the same group [16]. Within months, many new superconducting compounds of the same family were discovered, and maximum T_C was raised to $\approx$ 56 K [17, 18, 19]. Simultaneously, several related superconducting families were also discovered. In most of these systems, FeAs layers are crucial to superconductivity similar to the High-T_C cuprates where CuO_2 layers are the main ingredient for superconductivity [20, 18, 2, 19]. To date, many families of iron-based superconductors (FeSCs) have been discovered, and five of these families are summarized in Figure 1.2 with a representative example from each family listed. Depending on the chemical composition of their parent compounds, these families are called 11, 111, 122, 1111 and 32522 families respectively. For instance, parent compounds $BaFe_2As_2$, $CaFe_2As_2$ $SrFe_2As_2$ $EuFe_2As_2$ and their doped variants are all collectively referred to as the 122 family. However, to distinguish them from each other, notations like Ba122 (which represent 122 family derived from $BaFe_2As_2$), Sr122, etc., are also often used. Superconductivity in iron-based superconductors can be induced by substitutions at any of three cites, i.e., doping at transition metal, rare earth, pnictogen (chalcogen), and Oxygen site [18, 19]. Additionally, pressure can also induce superconductivity in many members of iron-based superconductors [21, 22, 23, 24, 25]. This flexibility of tuning parameters makes the FeSCs promising candidates to study the fundamental issues in superconductivity. There are many similarities and differences between iron-based superconductors and high-T_C cuprates. For instance, cuprates are Mott insulators where the single band approximation is a good starting point to understand their electronic properties. On the other hand, most parent compounds of FeSCs are multiband semimetals that order anti-ferromagnetically (Spin density wave) below a certain temperature. After doping or application of pressure (or both), magnetic/structural transition temperatures decrease, and superconductivity emerges at low temperatures. Additional doping/pressure further suppresses the magnetic/structural transition temperatures and T_C increases and reaches a maximum value near the spin density wave endpoint. Doping even further leads to the suppression of superconductivity and eventually T_C reduces to zero at a certain doping/pressure level. This leads to a dome-shaped temperature-composition phase diagram for most of the iron-based superconducting families (see Figure 1.3, taken from reference [3]), reminiscent of cuprates and heavy fermion systems [26, 12, 27, 28, 29, 30]. In this thesis we have focused on the magnetotransport studies in three distinct regions of the phase diagrams of $Ba(Fe_{1-x}Co_x)_2As_2$ and $Sr(Fe_{1-x}Co_x)_2As_2$ systems. Additionally, the physical properties of $(Eu_{1-x}Ca_x)Fe_2As_2$ were also determined using the thermodynamic and transport probes. FeSCs display many non-Fermi liquid properties which include pronounced linear temperature dependent resistivity, the presence of a linear magnetoresistance in magnetic state and strongly temperature dependent Hall coefficient to name a few.

The term 'Fermi liquid' is used to refer to the systems whose physical properties can be adequately described within the framework of the Fermi liquid theory proposed by physicist Lev Davidovich Landau [31]. This theory

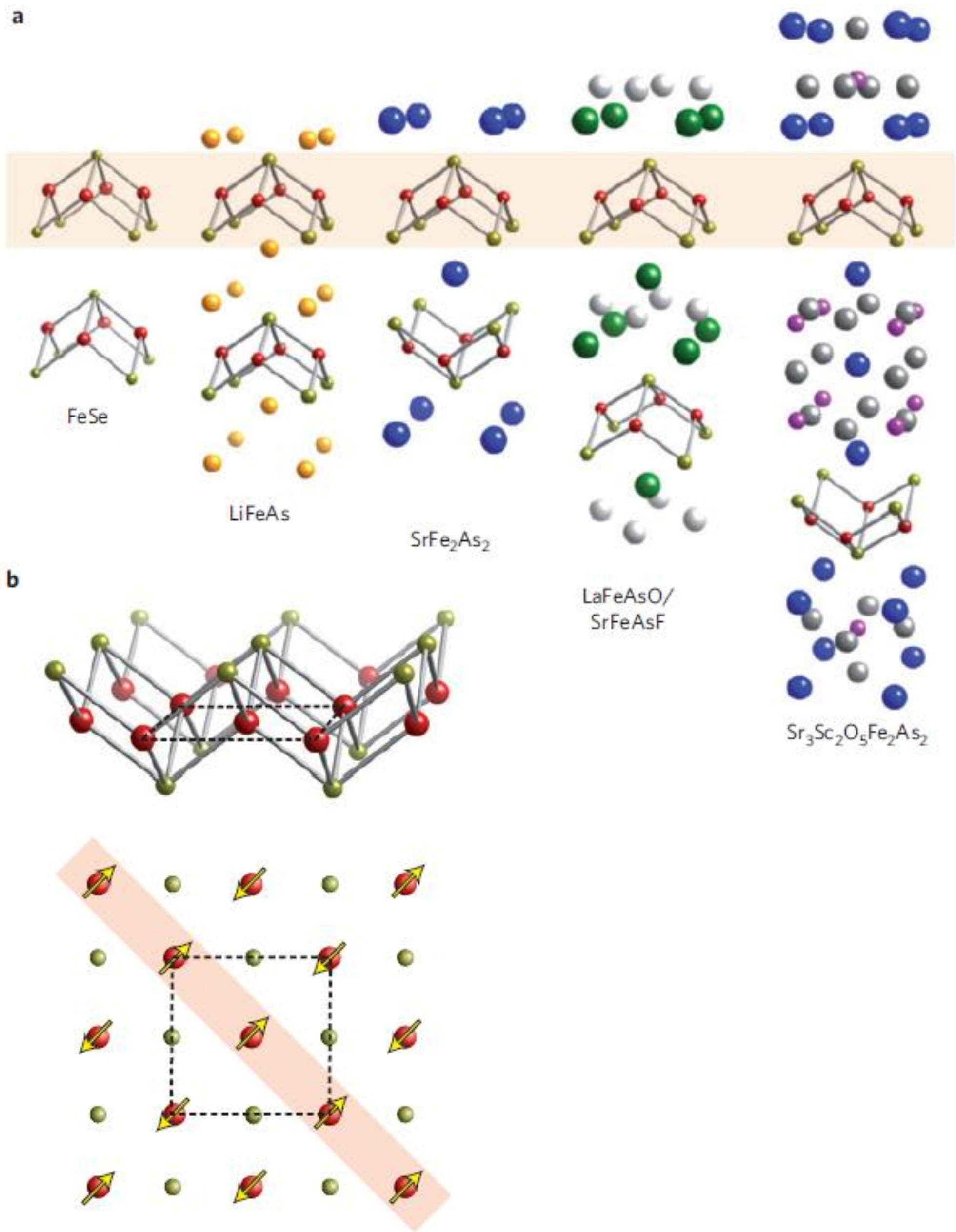

Figure 1.2: (a) Unit cells of the five families of FeSCs are shown with one member of each family listed below. (b), FeAs layer is shown with Fe atoms in red and As in gold color. The dashed line represents the unit cell of Fe square lattice. For clarity, the lower panel of Figure (b) represents the same FeAs layer without bonds, however with Fe moments denoted by arrows. Colored patch in the lower panel of Figure (b) depicts the Fe moments aligned ferromagnetically. Reprinted by permission from the Springer Nature: Nature Physics, Paglione at al., [2] ©2010.

can successfully describe, how the systems where the electronic interactions are not negligible, behave remarkably similar to free electron metals. Landau showed that when the interactions among the electrons are increased slowly (adiabatic continuity), the eigenstates of the interacting system remain the same as that of the non-interacting system, but now the eigenstates are associated with what he called the electron (hole) quasiparticles. A quasiparticle is the modified electron (hole) whose properties like mass are now renormalized as a result of electronic interactions. In certain strongly correlated systems, the Fermi liquid description breaks down, and physical properties can no longer be described in the context of weakly interacting quasiparticles. These systems are called non-Fermi liquids, and the region of their phase diagram where the Fermi liquid description is inadequate is called the non-Fermi liquid region or the strange metal phase [31].

In this thesis, an effort is made to put FeSCs in perspective with cuprates and heavy fermion systems on the basis of their magnetotransport behavior. Scaling techniques of magnetotransport are employed, which are a powerful tool to find similarities amongst different classes of superconductors. Detailed magnetotransport studies in magnetic as well as in the normal state of these systems suggest that the FeSCs behave differently than many cuprates and heavy fermions systems, except in a small underdoped region of the temperature-composition phase space.

We have also discovered for the first time, a linear magnetoresistance in the paramagnetic phase of some of these systems [32]. Linear magnetoresistance (LMR) is well reported in the magnetically ordered state of parent and underdoped compositions of many FeSCs (see section 1.1.4), but LMR in the paramagnetic phase is striking, and it can have important implications for the superconducting ground state in these systems. A number of possible models are discussed to explain the LMR in the paramagnetic state of these systems (Chapter 3 and 4). Our analysis also suggests that the Abrikosov's model of linear magnetoresistance which is often employed to address the LMR in the magnetic state of FeSCs may not be applicable to these systems.

In the rest of this chapter, we give a brief account of the magnetic, crystallographic, and electronic structure of FeSCs, with special emphasis on 122 family and its electron-doped variants (section 1.1.1). In the next section, the magnetotransport scaling techniques; the Kohler and Modified Kohler's rule are discussed in detail. To help highlight the commonality/differences among the high-T_C cuprates, heavy fermions and the systems in the present study, a summary of the scaling analysis of the magnetotransport of some heavy fermions and high-T_C cuprate superconductors is given. The 'pseudogap' is introduced in the next section (section 1.1.3), and a very brief account of its existence/absence in other systems like cuprates and heavy fermions is

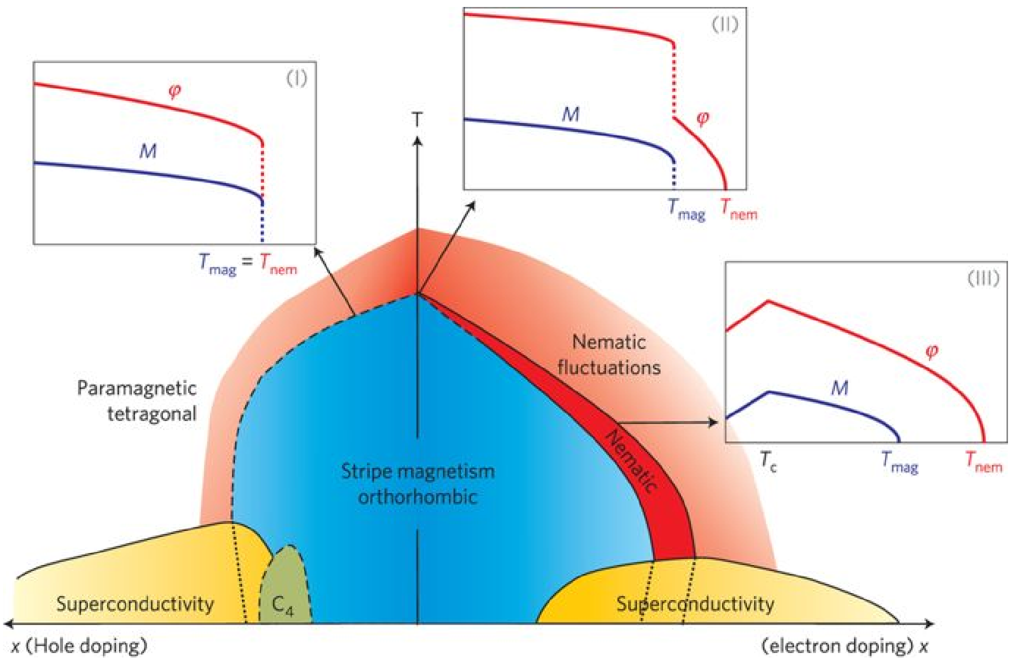

Figure 1.3: Phase diagram for electron and hole doped derivatives of $BaFe_2As_2$. Yellow and blue regions correspond to the superconducting and magnetic ground states respectively. Dark Red regions corresponds to the electronic nematic region where pronounced anisotropy in transport and other properties is observed. ϕ and M represent the nematic and magnetic order parameters and their behavior in regions (I), (II), and (III) as depicted in the boxes. The green region labeled as C_4 corresponds to the systems which undergo a magnetic transition without an accompanying structural (tetragonal) transition. Hole doped systems have rather weak anisotropies in the tetragonal regime which is indicated by the lighter shade of red color (left part of the figure). Reprinted by permission from the Springer Nature: Nature Physics, Fernandes at al., [3] ©2014.

presented. The Dirac cone states and linear magnetoresistance along with a brief account of Abrikosov's model of linear magnetoresistance are discussed in the last section (section 1.1.4).

Magnetotransport studies of $Sr(Fe_{1-x}Co_x)_2As_2$ and $Ba(Fe_{1-x}Co_x)_2As_2$ are reported in chapters three and four respectively. Chapter five discusses the thermodynamic and transport measurements of the $(Eu_{1-x}Ca_x)Fe_2As_2$ series. In this system, Eu moments order antiferromagnetically at low temperatures, in addition to the antiferromagnetic ordering of Fe moments in the crystallographic '*ab*' planes at higher temperatures. This series shows a subtle coupling between the Eu and Fe sublattices. For instance, doping Ca in $(Eu_{1-x}Ca_x)Fe_2As_2$ series does not affect the ordering of Fe moments in the crystallographic '*ab*' plane up to a critical concentration. However, doping further leads to the suppression of the magnetostructural transition associated with the ordering of Fe moments. In chapter six, we discuss the scope of future work along with the conclusions drawn from the work presented in this thesis.

1.1 Key concepts & issues

In this section, we first describe the crystallographic, electronic and magnetic structure of FeSCs. In the following subsections, we discuss several topics: nematic order, pseudogap, linear magnetoresistance, magnetotransport scaling behavior, etc., which are the central theme in FeSCs. Doing so will also help us interpret our experimental results in later chapters.

1.1.1 Crystallographic, magnetic & electronic structure of FeSCs

There exist several families of FeSCs, which have many similarities and differences amongst each other. Parent compounds in most cases crystallize in a tetragonal $ThCr_2Si_2$ type (space group $I4/mmm$) structure for the 122 family and $P4/nmm$ for the 1111 family. Fe atoms are bonded with pnictogens/chalcogens in a distorted edge sharing tetrahedral coordination with Fe atoms forming a 2D square lattice in crystallographic '*ab*' plane. Alkaline earth atoms (Ba, Sr, etc.) are coordinated with eight pnictogen/chalcogen (As, Se, etc.) atoms. There is no direct chemical bonding between neighboring FeAs layers [33]. Unit cells of some representative families are depicted in Figure 1.2. The '11' family, is the simplest of all, with only one Fe-pn/ch

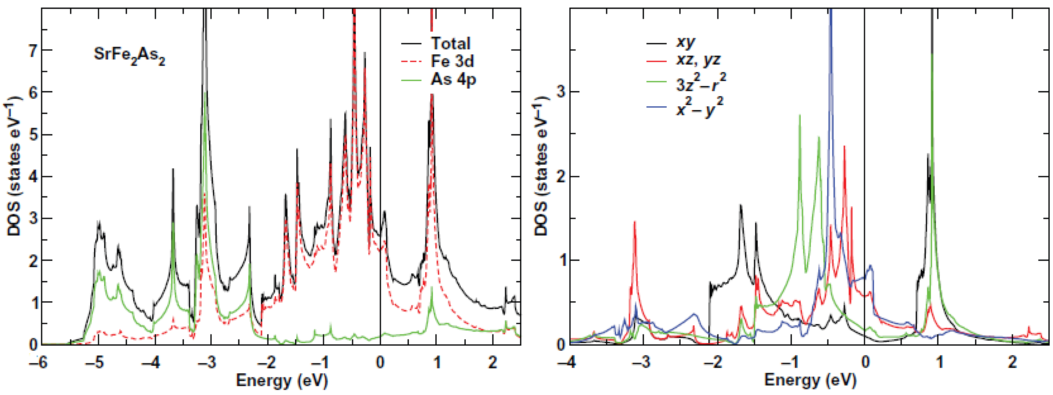

Figure 1.4: Left panel: Electronic structure of $SrFe_2As_2$ calculated using DFT within LSDA+U approximation utilizing the experimental lattice parameters. Right panel: Orbital resolved electronic structure of the $SrFe_2As_2$, demonstrating that almost all of the contribution to the density of states at the Fermi level comes from the Fe *d* orbitals. Reproduced from Ref. [4]

layer per unit cell[1], Whereas in all other families the FeAs layers are sandwiched between charge reservoir layers (LaO, Ba, etc.). Here 'pn' and 'ch' refers to the pnictogens (As, P) and the chalcogens (Se, Te) respectively. The 'c' lattice parameter is roughly 4 Å, 8.5 Å and 13 Å, in 11, 1111 and 122 families respectively [18]. This is expected since the 11 family has no spacer or buffer layers in the unit cell, 1111 family has only one FeAs layer per unit cell, and 122 family has two FeAs layers along with buffer layers. Not surprisingly, the 'a' parameter remains roughly the same in all families since the existence of spacer layers does not affect the crystallographic 'ab' plane or FeAs layers [18]. A similar argument can be extended to other families as well. Figure 1.4 shows the density of states for $SrFe_2As_2$ system calculated by first principle density functional calculations using the experimental lattice parameters (taken from reference [4]). Most of the contribution to the density of states comes from the FeAs layers, suggesting that the physical properties are determined predominantly by FeAs layers. Also, it was shown that the superconductivity depends on the details of the crystallographic structure. For instance, Lee et al. [34, 5], plotted the As-Fe-As tetrahedral bond angle for many families of FeSCs and found that the T_C shows a maximum when the bond angle is close to its ideal value: 109.47°, see Figure 1.5. Later, a correlation between the height of pnictogen atoms above the Fe square lattice with T_C was discovered, see Figure 1.5. It was found that the maximum T_C is observed for the systems for which the height of pnictogen atoms above the

[1]hereafter, we will refer to these as FeAs layers unless otherwise stated.

Fe plane is ≈1.38 Å [6, 35]. Later on, a microscopic justification was given by Kuroki et al. [36], suggesting that the higher pnictogen height leads to stronger spin fluctuations, which can give rise to higher T_C's in the scenario of spin fluctuation mediated superconductivity.

At low temperatures (100−200 K), parent compounds undergo magnetic and structural transitions which are combined in most 122 families and distinct in some families (e.g., 1111 type) [18, 19]. In most FeSCs, the magnetic transition is closely followed by (at slightly high temperatures) the structural transition which changes their symmetry from high-temperature tetragonal I4/mmm space group to a distorted orthorhombic Fmmm space group at low temperatures. After doping and/or under the application of pressure, these transitions gets suppressed and separated. Nature of magnetostructural transitions is debated; for instance in the $BaFe_2As_2$ system, there are reports where both magnetic and structural transitions are second-order [37], and there are reports with the magnetic transition being first-order [38, 39]. It has been emphasized that doped $BaFe_2As_2$ systems show second-order magnetic and structural transitions [40, 41, 42]. A theoretical study suggested that the parent compounds of some FeSCs are near a tricritical point [43], which would support the second order nature of magnetic/structural transitions in doped $BaFe_2As_2$ systems. Presence of a tricritical point was confirmed in high resolution magnetic and thermodynamic measurements [44, 39].

Typical values of ordered moments are $\sim 0.9\mu_B$ for $BaFe_2As_2$ [37, 45] and $\sim 0.36\mu_B$ for LaOFeAs [46] respectively. Magnitude of ordered moment decreases after doping, for instance, Fe moment in $Ba(Fe_{1-x}Co_x)_2As_2$ reduces to $0.35(\pm 0.1)\mu_B$ and $0.2(\pm 0.1)\mu_B$ after 2.5% and 4.7% cobalt doping, respectively [40, 47]. These ordered moments (of Fe) are considerably small compared to its value of $2.2\mu_B$ in iron metal [46, 48] or the value of $3.32\mu_B$ observed in ionic insulators [18].

Highly reduced values of the Fe moments raise questions about the nature of magnetism in FeSCs. Magnetism certainly is not of the local moment type which would lead to higher values of Fe moments. It has been suggested that the frustration or spin fluctuations can be the reason for low values of magnetic moments. Early on, it was suggested that the competing nearest neighbor and next nearest neighbor interactions lead to frustration in FeSCs which were suggested to be on the verge of becoming a Mott insulator [49, 50]. Clues were taken from the room temperature resistivity of parent compounds of FeSCs which were $\sim 5\ m\Omega$ cm for LaOFeAs polycrystalline samples, suggesting that FeSCs are neither very good metals nor Mott insulators like cuprates. However, in later studies on single crystals, lower room temperature resistivities of ~ 0.8 mΩ cm were reported [18]. It

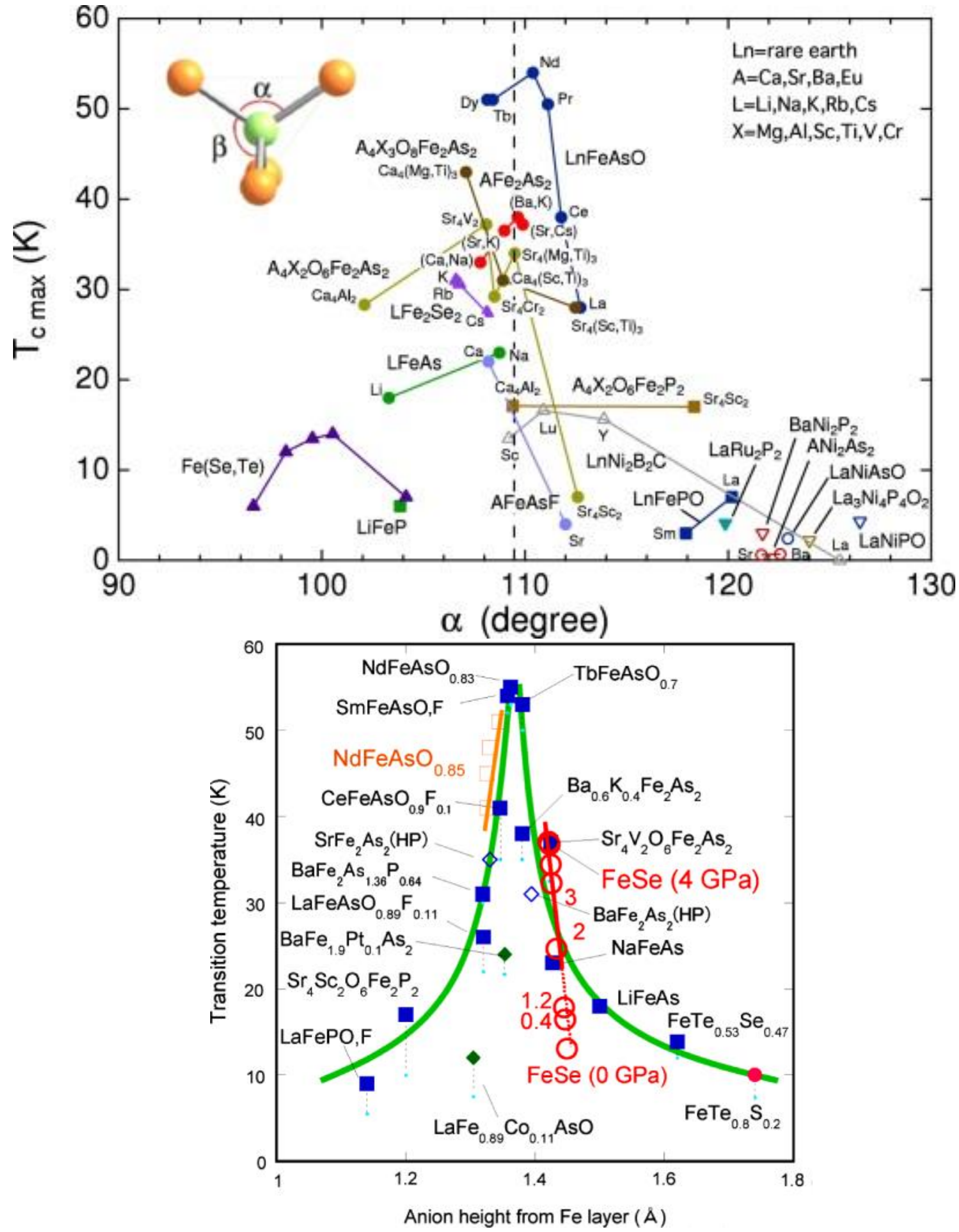

Figure 1.5: Upper panel depicts the correlation between tetrahedral bond angle α (as illustrated in the inset) and maximum T_C observed in different families of FeSCs. In the lower panel, the correlation between the height of pnictogen/chalcogen atoms above the Fe square lattice and maximum T_C is shown for FeSCs. Upper panel in this Figure: reprinted with permission from Elsevier, Solid State Communications, Lee et al., [5] ©2012. Lower panel: reprinted with permission from IOP Publishing, Mizuguchi et al., [6] ©2010.

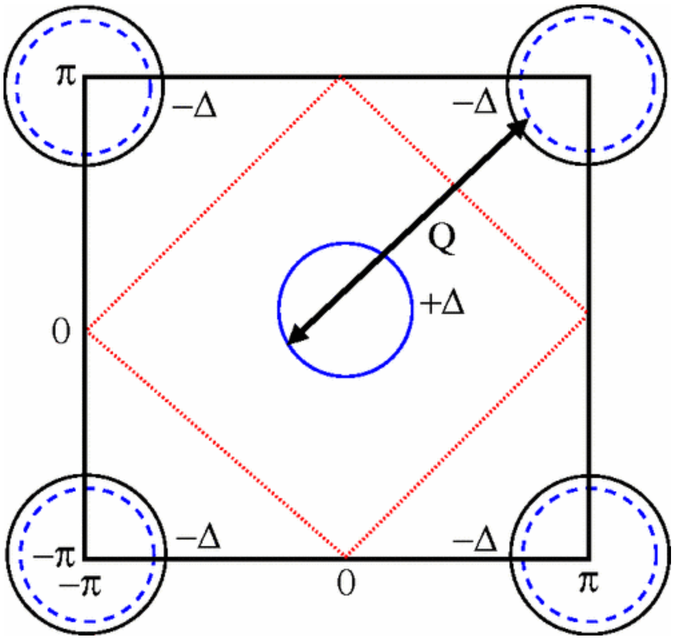

Figure 1.6: A simplified geometry of the Fermi surface for the parent compounds of FeSCs. Blue dashed circles represent the electron pockets around (π, π) and the solid blue circle around $(0, 0)$ represent the hole pocket of similar size. In this idealized system, there is perfect nesting between electron and hole pockets, i.e., translating the hole pockets by (π, π), as represented by the nesting wave vector Q, one obtains a complete overlap of these Fermi surfaces. $+\Delta$ and $-\Delta$ represent the superconducting gaps on the hole and electron Fermi surfaces, respectively. Reprinted with permission from the American Physical Society, Physical Review **B**, Chubukov et al., [7] ©2008

is now believed that FeSCs may not be good conductors like simple metals (e.g., copper), but may not be on the verge of Mottness either. Presently, itinerant electrons are thought to be responsible for the Spin density wave (SDW) type antiferromagnetic order of FeSCs, which arises as a consequence of nesting between disconnected parts of Fermi surface [7, 2], see Figure 1.6.

1.1.2 Magnetotransport: Scaling techniques

Magnetotransport is a sensitive probe of the electronic structure and Fermi surface of metals. It has played a pivotal role in the study of high-T_C cuprates and heavy fermions. For instance, motivated by the universality observed in the magnetotransport behavior of cuprates, where, the Hall angle showed qualitatively similar behavior in a number of cuprates led to similar studies in several heavy fermion materials and more recently in some iron-based superconductors [51]. Magnetotransport, particularly, the scaling techniques can serve the purpose of finding the universal features among diverse classes of superconducting materials, providing us with important insights into the phenomena of superconductivity. Importantly, these studies do not always require extreme conditions, e.g., strong magnetic fields or very low temperatures, though having access to such extreme conditions can provide more information about the systems under investigation. Since magnetotransport is a sensitive probe of the Fermi surface; it can provide important insights for the theoretical studies. For instance, the anomalous magnetotransport behavior of cuprates led to the development of theories where an anisotropic reconstruction of the Fermi surface is invoked [52, 53, 54]. Due to this anisotropic scattering across the Fermi surface, transport coefficients behave differently than what is expected in conventional theory. Similar theories of anisotropic reconstruction of the Fermi surface were later invoked to interpret the results of magnetotransport in heavy fermions and FeSCs [55, 56, 57]. Magnetotransport studies have been decisive in characterizing the nature of quantum critical points in heavy fermions. For, instance, the evolution of Hall coefficient across the quantum critical point can distinguish between two types of (QCPs) that have been controversially discussed in different heavy fermion materials [58]. In one type of QCP, where the many body Kondo state remains intact when the QCP is approached, the Fermi surface is supposed to evolve continuously, which in turn reflect in the smooth variation of inverse Hall coefficient [59]. On the other hand, in the unconventional QCP scenario where the Kondo state breaks down while approaching the QCP; and, as a consequence, the volume of Fermi surface changes rather abruptly [58]. The Hall coefficient was indeed experimentally observed to change abruptly across this unconventional QCP in the heavy fermion superconductor $YbRh_2Si_2$ [60]. In this thesis, we have employed the scaling techniques of the magnetotransport to investigate some 122 families of FeSCs. We discuss these scaling techniques in detail in the following sections.

The Kohler's Rule

Normal state magnetotransport of metals is a powerful tool to study their electronic structure. However, scaling techniques have proven to be an even more powerful tool to find the commonalities between different classes of unconventional superconductors, like cuprates, heavy Fermions and recently iron-based superconductors. We begin by discussing the magnetotransport

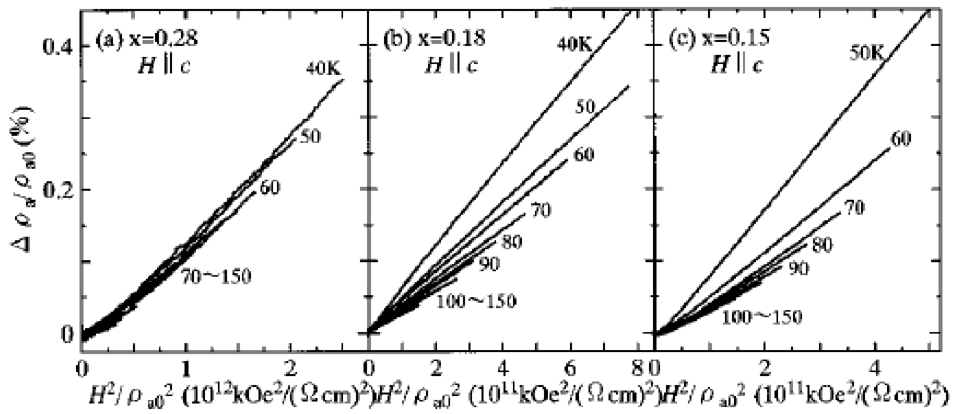

Figure 1.7: Kohler's scaling for three compositions of $La_{2-x}Sr_xCuO_4$. The suffix 'a' on the Y axis refers to the fact that current was applied along the crystallographic 'a' axis, whereas magnetic field was along the 'c' axis, as depicted in the insets. In (a), all magnetoresistance isotherms almost collapsed on a single curve, indicating that the Kohler's rule is valid for $x =$ 0.28. However, in (b) and (c), Kohler's rule is violated for both $x = 0.18$ and 0.15 respectively. Reprinted with permission from the American Physical Society, Physical Review **B**, Kimura et al., [8] ©1996

scaling method most often employed in simple metals, and even in complex materials like high-T_C cuprates: the Kohler's rule [61, 62, 63]. It states that the orbital magnetoresistance (MR) of a material can be expressed as a function of Hτ.

$$MR = [\rho(H) - \rho(0)]/\rho(0) = \Delta\rho/\rho(0) = F(H\tau)$$

The magnetoresistance is defined as the change in electrical resistivity after the application of magnetic field: $[\rho(H) - \rho(0)]/\rho(0)$. Here, $\rho(H)$ is the resistivity at a magnetic field H, ρ_0 is the resistivity at zero magnetic field and τ is the transport relaxation time. In literature, the Kohler's law is often represented as MR $\propto$ H/ρ or $(H/\rho)^2$. This can be seen by using the zero field resistivity in Drude picture: $\rho_0 = m/ne^2\tau$, hence the above equation 1.1.2 becomes

$$\Delta\rho/\rho(0) = F(H\tau) = F(Hm/\rho_0 ne^2) = G(H/\rho_0)$$

Here m is the effective electronic mass, e is the electronic charge and 'G' is a function of material's electronic structure and geometry [64].

Kohler's scaling is based on certain preconditions, some of which are apparent from the definition itself. First, the relaxation rate (τ^{-1}) should be constant across the whole Fermi surface and should not change with temperature (or change in the same manner across the whole Fermi surface). Secondly, there should be only one species of charge carrier that dominate the transport, i.e., multiple species of charge carriers with different relaxation rates will lead to the violation of Kohler's scaling. Also, the change in the electronic concentration with temperature will lead to the violation of Kohler's rule. In another scenario, the magnetoresistance and the zero field resistivity may be governed by different relaxation rates, hence leading to the violation of Kohler's rule [65]. The Kohler's rule has been found to be valid for a number of simple metals [62, 63], and even in the Fermi liquid regime of the high-T_C cuprates, and heavy fermion superconductors [8, 51, 66]. Similarly, it was found to be obeyed in the Fermi liquid state of some iron-pnictides as well [67, 68]. Not surprisingly, the Kohler's rule is often violated in the non-Fermi liquid regime of cuprates, heavy fermions and FeSCs [65, 8, 67, 69, 70, 71, 72, 8, 66]. Figure 1.7 demonstrates the crossover in the Kohler's scaling behavior in a cuprate, where it is obeyed at higher doping levels and violated at lower doping levels[2] [8]. A similar evolution of magnetotransport from the under-doped to overdoped compositions was observed in some iron-pnictides [67] and heavy fermion systems[51].

The Modified Kohler's rule

As discussed in the previous section, the Kohler's scaling works remarkably well for many conventional metals, and even in some region of the phase space of cuprates. However, it was reported to be violated in the strange metal phase of a number of cuprates, as shown in Figure 1.7 for x = 0.18 and 0.15 in $La_{2-x}Sr_xCuO_4$ [8]. A new scaling method was put forth by Harris et al., where the magnetoresistance ($\Delta\rho/\rho(0)$) scales not as a function of Hτ or $(H/\rho)^2$ but by the Hall angle tanθ_H, i.e.,

$$[\rho(H) - \rho(0)]/\rho(0) = \Delta\rho/\rho(0) = F(tan^2\theta_H)$$

This was termed the Modified Kohler's rule [65]. Here, tan$\theta_H = \rho_{xy}/\rho_{xx}$, ρ_{xy} is the Hall resistivity and ρ_{xx} is the magnetoresistivity. Modified Kohler's scaling was then observed to be valid in a number of cuprates. Later, it was found that this new scaling works well for many heavy fermion systems as well [66, 72, 73, 74, 75] suggesting that the heavy fermions and cuprates bear many similarities at least as far as the magnetotransport is concerned [66]. The violation of Kohler's rule and the validity of Modified Kohler's rule in

[2] these doping levels are where the most pronounced non-Fermi liquid behaviors are observed.

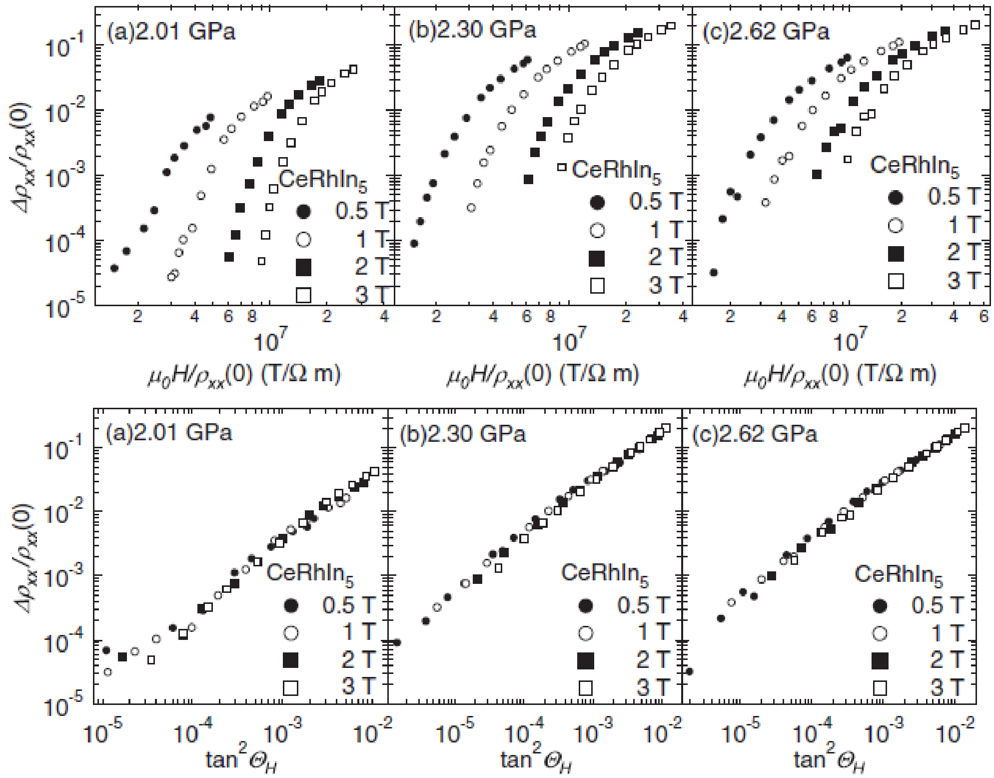

Figure 1.8: Violation of Kohler's rule for $CeRhIn_5$ is depicted in the upper panel. The bottom panel depicts the validity of modified Kohler's rule at same pressure values as in the upper panel. These pressure values correspond to the non-Fermi liquid regime of $CeRhIn_5$. ©(2007) The Physical Society of Japan.

the strange metals phase of the heavy fermion system $CeRhIn_5$ is depicted in Figure 1.8.

The modified Kohler's rule is a corollary based on a rather radical idea put forth by theoretical physicist P. W. Anderson [76]. He proposed that in a Luttinger Liquid, electronic charge and spin degrees of freedom can get decoupled, leading to two relaxation times [76]. In this scenario, the two relaxation rates τ_H^{-1} and τ_{tr}^{-1} govern the Hall angle $\cot\theta_H$ and resistivity respectively. These relaxation times were a natural explanation for the violation of the Kohler's rule in cuprates. The spinon-spinon scattering relaxation time τ_H was proposed to vary as T^2 which is typical of fermionic scattering processes. Transport relaxation rate τ_{tr} was presumably thought to be proportional to temperature i.e., $\tau_{tr} \propto$ T since cuprates had the linear temperature dependent resistivity, especially near optimal doping where the non-Fermi liquid behaviors are pronounced. However, the idea of different relaxation times governing the resistivity and the Hall angle is often thought be valid as long as they have different temperature dependencies. It should be noted that in free electron scenario, $\cot\theta_H$ and ρ_0 are supposed to have same temperature dependence, because they are dictated by same relaxation rate (τ^{-1}):

$$cot\theta_H = \rho/HR_H = (m/ne^2\tau)/(H/ne) \;\; \propto \;\; \tau^{-1} \qquad \because R_H = 1/ne$$

and

$$\rho = m/ne^2\tau \;\; \propto \;\; \tau^{-1}$$

whereas in two relaxation rate scenario, resistivity and Hall angle θ_H are governed by different relaxation rates:

$$cot\theta_H = \rho/\rho_{xy} \propto \tau_{tr}^{-1}/(\tau_H^{-1}\tau_{tr}^{-1}) \propto \tau_H$$

An interesting ingredient of the theory is that the relaxation times appear in products in the Hall resistivity: $\rho_{xy} = (\tau_H\tau_{tr})^{-1}$ [77]. This suggests that it is the Hall angle which is of fundamental importance and not the Hall resistivity. This assumption was further bolstered by experiments, where despite the complex temperature dependencies of Hall coefficients in different cuprates (and later heavy fermions), cotangent of Hall angle almost always had T^2 dependence

$$cot\theta_H \propto \tau_H = AT^2 + B$$

Here, A is a measure of Hall relaxation rate τ_H^{-1} and the B depends on impurity concentration. This T^2 dependent Hall angle was observed in a large number of cuprates and was found to be quite resistant to impurity content. In Figure 1.9, $cot\theta_H$ is plotted against T^2 for five different types of dopants in $La_{1.85}Sr_{0.15}Cu_{1-x}A_xO_4$, where A = Fe, Co, Ni, Ga and Zn [9]. A straight line is observed, attesting to the T^2 dependence of Hall scattering rate (τ_H^{-1}). Also, it is clear that varying the doping content for all five dopants does not affect the slope of T^2 plots, but merely shifts the curves by a constant amount determined by the impurity concentration. This robust T^2 behavior of the Hall angle was observed for many families of cuprates [78, 79] and later in heavy fermions [80] and even in organic superconductors [81]

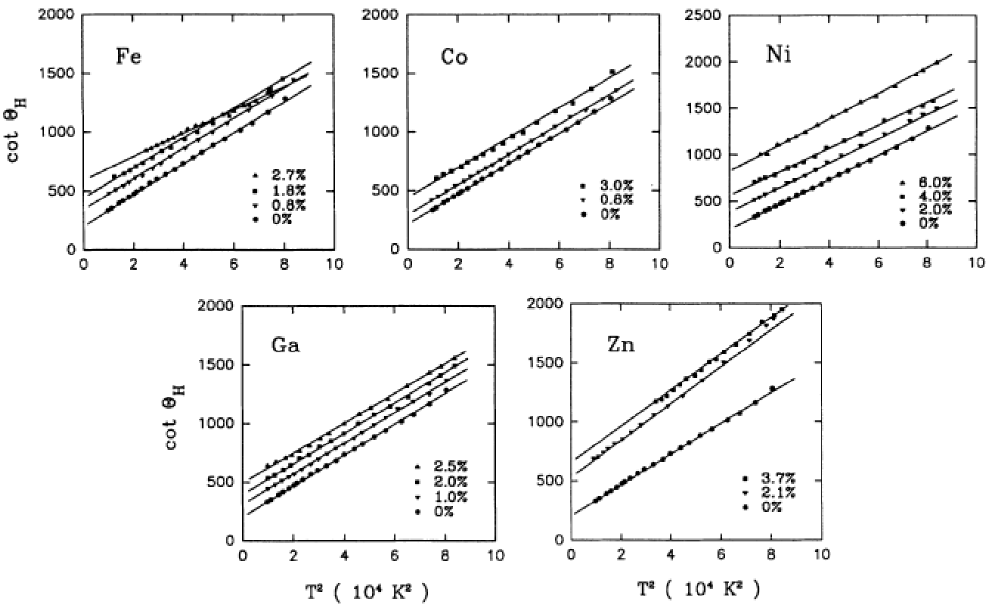

Figure 1.9: $cot\theta_H$ is plotted as a function of T^2 for five types of dopants in $La_{1.85}Sr_{0.15}Cu_{1-x}A_xO_4$, as indicated in respective insets. Reprinted with permission from the American Physical Society, Physical Review **B**, Xiao et al., [9] ©1992

Interestingly, thermopower and Nernst effect measurements also suggested the existence of two relaxation rates in cuprates [82, 83]. Magnetotransport scaling techniques are not as extensively applied in FeSCs as is the case in cuprates and heavy fermions. There are only a few reports that discuss the scaling analysis of magnetotransport [84, 67]. In addition to the cuprates, heavy fermions, and FeSCs, few other systems also demonstrated the evidence for two relaxation times, for example, in three dimensional Mott insulator $V_{2-y}O_3$, resistivity and $\cot\theta_H$ were shown to have different temperature dependencies [85]. Also, away from the half filling[3], resistivity and Hall angle had the same temperature dependence, which was accompanied by a temperature independent Hall coefficient bearing a striking similarity to cuprates and heavy fermions [80, 51]. Recently two dimensional electron liquids at the interfaces of oxide heterostructures ($SrTiO_3/RTiO_3$, R= Sm and Gd) were also reported to show 'two lifetimes' in transport studies [86, 87, 88]. Additionally, some ruthenates (9 layered $BaRuO_3$ (9R) and $CaRuO_3$) also depicted the existence of two relaxation rates [89, 90].

It is clear from the discussion so far that the existence of two relaxation times seems to appear in diverse classes of materials, not just in cuprates or heavy fermions as originally thought. No single theory can explain these results in a unified manner, which again depicts the complexity of magnetotransport behavior in these systems. Although, the original idea of modified Kohler's rule or T^2 dependent Hall angle[4] was derived from the 'Luttinger liquid' formalism of Anderson, there are a couple of alternative theories which attempted to interpret the existence of two relaxation times in some variants of Fermi liquid theories [77]. We will now briefly mention some of them.

In addition to the spin-charge separation theory of Anderson, theories based on the Fermi liquid ground state where the anisotropic scattering on the Fermi surface(s) determine the Hall and transport scattering rates were put forth to explain the anomalous transport behavior of cuprates by David Pines and others [91, 92, 93]. The concept of hot and cold spots was coined, where 'hot spot' is the region on the Fermi surface where carrier lifetime is unusually short, whereas, on the 'cold spot', the scattering rate has weaker temperature dependence than the hot regions. Here, resistivity and Hall resistivity are determined by the scattering rates on hot and cold spots as

[3] $V_{2-y}O_3$ becomes more metallic at higher 'y' (~ 0.033). This highly doped region is analogous to the overdoped regime of cuprates, heavy fermions, and some FeSCs, where conventional Fermi liquid behaviors are recovered.

[4] Magnetoresistance and Hall angle are governed by the same scattering time: τ_H

follows [77]:

$$\rho \propto \Gamma_{hot} \ and \ \rho_{xy} \propto \Gamma^2_{cold}$$
$$also, \ \Gamma_H = \Gamma^2_{cold}/\Gamma_{hot}$$

It is clear that Hall relaxation rate (Γ_H) is not universal and is determined by the balance between the scattering from cold and hot spots.

In another Fermi liquid approach (or Nearly Antiferromagnetic Fermi liquid (NAFL)), Kontani et al., have developed the theory for transport coefficients [94, 95, 96, 97, 54]. They include the current vertex correction (CVC) that arises due to strong scattering of spin fluctuations, which are ignored in relaxation time approximation (RTA). Total current is modified by the backflow effect due to CVC's leading to the unconventional behavior of transport coefficients in NAFL metals [98]. The scattering due to spin fluctuations can strongly renormalize the transport coefficients, which can lead to the violation of Kohler's rule as well as the apparent presence of two relaxation rates.

1.1.3 Pseudogap

There are two prevailing definitions of the pseudogap in literature. In one scenario, it is the gap associated with the formation of the phase incoherent Cooper pairs that form above the superconducting transition. In this case, it is believed that the pseudogap is a precursor to the superconducting ground state [99, 100, 101]. In another scenario, it is a partial gap in the electronic structure, much above the superconducting transition and even in systems that do not show superconductivity [102], leading to a decreased density of states. Some studies suggested that pseudogap is a distinct energy scale that competes with superconductivity [103, 104]. This complication persists due to the reports of contradictory results from different experimental techniques [102]. The microscopic origin of pseudogap may be debatable, but its existence in many FeSCs just like it is for high-T_C cuprates has been strongly agreed upon. Signatures of the pseudogap has been observed in many FeSCs by various probes: resistivity [105, 106, 107], Hall angle [105, 108], optical transport [109, 110], NMR [111], NQR [112], thermopower [113], magnetic susceptibility [114], Photoemission [115, 116, 117] and thermal transport [118]. However, like cuprates, its emergence and termination (points in the phase diagram) vary between different families and techniques adding to the confusion. For instance, in $Ba(Fe_{1-x}Co_x)_2As_2$, pseudogap transition temperature determined from the interplane transport and NMR measurements suggest that the pseudogap temperature T^* decreases from parent compound to overdoped compositions. On the contrary, for the hole-doped $Ba_{1-x}K_xFe_2As_2$, T^* determined from the same techniques remains almost constant with doping.

Of particular interest here are the Hall angle studies of the pseudogap. Hall angle is sensitive to the electronic structure and mass renormalization effects among others. Historically, deviations from the T^2 dependent Hall angle were used to infer the possibility of the pseudogap in cuprates [119, 120, 121, 122, 78, 123, 124]. Although the Hall angle studies of FeSCs have been limited to date, few reports of such analysis exists. In $NaFe_{1-x}Co_xAs$, deviations from the power law resistivity and Hall angle matched very well, and T^* determined from this deviation was referred to as the pseudogap temperature [105]. Similar deviations were reported for $SmFeAsO_{1-x}F_x$ [106]. We have also observed the signatures of the pseudogap in the Hall angle above magnetic/structural transitions in an underdoped composition of $Ba(Fe_{1-x}Co_x)_2As_2$ [108], which will be discussed in Chapter 4.

1.1.4 Quantum linear magnetoresistance & Dirac states

In the antiferromagnetic spin density wave state of FeSCs, an anomalous positive linear magnetoresistance (LMR) is observed [125, 126, 127, 128, 129, 24, 130, 131, 132, 133, 134, 69, 135, 136]. This LMR is pronounced at low temperatures and is strongest in undoped specimens i.e., parent compounds. It is believed that this LMR originates from the Dirac cone states [133, 113, 126, 128], which were theoretically predicted [137, 138, 139] and experimentally observed using a number of probes such as ARPES [140] and quantum oscillations [141, 142, 143, 144, 145, 146] among others [147, 132, 148, 149, 150, 151]. Dirac cones in FeSCs are formed (in pairs) due to the d band folding within the nodal spin density wave state [139, 132]. Dirac states have been observed in a number of FeSCs, like $BaFe_2As_2$ [140], $SrFe_2As_2$ [141], LaFeAsO [125], PrFeAsO [128], etc. Though the existence of Dirac cone states in FeSCs is well established, the manifestations of their existence for the superconducting ground state are not clear (not studied). In an isolated (probably the only study) study, it was suggested that the high mobility Dirac carriers might act as a strong Josephson link between superconducting islands providing protection against the phase fluctuation effects, and consequently bring about a robust high-T_C superconducting ground state [131]. Often, in literature, the origin of this LMR has also been explained, using the Quantum linear magnetoresistance (QLM) model of Abrikosov [135, 152, 136]. It should be noted that in addition to FeSCs, Abrikosov's QLM model has been applied to many other materials like silver chalcogenides [153], CaC_6 [154] and graphene [155].

In 1969, Abrikosov developed the theory of galvanomagnetic phenomena in metals [156] where he calculated the magnetoresistance in quantum limit: the condition in which all carriers occupy the lowest Landau band (see 1.1). Theory predicted a linear magnetoresistance in quantum limit. The original formulae in that study were [157]:

$$\rho_{xx} = N_i H/n^2 e, \quad \rho_{xy} = H/ne$$

the above equations are valid if the following conditions called the 'Extreme Quantum Limit (EQL)' are met:

$$n \ll (eH\hbar)^{3/2}, \quad T \ll eH\hbar/m^* \tag{1.1}$$

Here, H is applied magnetic field, n is the carrier concentration, e is the electronic charge and ρ_{xx} is the resistivity at magnetic field H. Clearly, high magnetic field, low effective carrier masses and low temperatures are the favorable conditions for Extreme Quantum Limit. Abrikosov, later, using his theory, explained the LMR observed in different classes of materials [158, 159, 160]. He suggested to call it the quantum linear magnetoresistance. In his own words: "In order to distinguish this phenomenon from other kinds of unusual magnetoresistance phenomena (they all lead to negative magnetoresistance!) I suggest that it be called quantum magnetoresistance." [157]. Although the Quantum limit conditions are the same, the LMR observed in different systems takes different forms depending on the electronic and material structure. We will give examples below, where Abrikosov personally gave some ideas as to how the quantum limit conditions can be fulfilled in these cases and his model can be applied.

Some off-stoichiometric silver chalcogenides (e. g. $Ag_{2+\delta}Se$ and $Ag_{2+\delta}Te$) were shown to exhibit LMR from magnetic fields as low as 10 Oe up to many Tesla's [161, 153], without any sign of saturation. Since these systems are inhomogeneous semiconductors, Abrikosov proposed that due to the phase segregation, regions of very low and high carrier densities are formed; hence the 'Extreme Quantum Limit' conditions can be satisfied within the regions of low carrier concentration.

Another class of materials, called rare-earth di-antimonides (RSb_2, R = Ce-Sm) were also shown to exhibit the nonsaturating linear magnetoresistance [162]. To explain the fulfillment of Extreme Quantum Limit conditions, Abrikosov compared these materials[5] with graphite [163]. Graphite is a semimetal with many properties similar to the di-antimonides, e.g., strong

[5]Band structure of rare-earth di-antimonides was not known at that time.

anisotropy between in and out of plane properties. He suggested that two-dimensional materials, in certain parts of the band structure, will have a linear dispersion, at least close to the transition. These linearly dispersing bands will give rise to low carrier density and low effective carrier masses, hence EQL conditions may be fulfilled [160]. This situation is very close to what is observed in FeSCs. We will now discuss the quantum magnetoresistance model for FeSCs and then see how the band structure of FeSCs can support LMR in view of the Abrikosov's model.

For FeSCs, parent compounds of which are semi-metals, the LMR takes the following form[158]:

$$\rho_{xx}(H) = H/f(n)N_i ne \tag{1.2}$$

MR for the uncompensated (doped) FeSCs would take the form[158]:

$$\rho_{xx}(H) = f(n)N_i H/(n_e - n_h)^2 e \tag{1.3}$$

Here, *f(n)* is some function, whose value is close to unity [158], $n_e - n_h$ is the effective carrier concentration and N_i the concentration of scattering centers. LMR is apparent from the above mentioned formulae, however, see the difference how concentration of scattering centers (N_i) appear in two formulas. Let us now return to the question of how the presence of Dirac cone states can support the LMR in the context of Abrikosov's QLM model.

LMR can be observed in the parabolic (E $\propto K^2$) as well as the linearly dispersing bands (E $\propto K$), as long as the QLM conditions (equation (1.1)) of the Abrikosov's model are fulfilled. However, as we shall shortly see, it is possible to fulfill QLM conditions even under the typical laboratory conditions under which LMR is typically reported in FeSCs [157, 132]. The quantum limit conditions are reached when all the carriers occupy the lowest Landau level. This condition for a linear band occurs when the energy level splitting between the first and zeroth Landau levels becomes greater than the thermal energy: $E_{\pm 1}$-E_0 = $\pm$ $V_F\sqrt{2e\hbar H}$ > K_BT. Energy level splitting for a parabolic band is: $E_{\pm 1}$-E_0 = $eH\hbar/m^*$ > K_BT, where H is the magnetic field, m^* is effective electronic mass. It is evident that in the linearly dispersive bands, the QLM conditions can be fulfilled at lower fields compared to parabolic bands, because in the former case splitting is proportional to the square root of the magnetic field, whereas, in the later, it is proportional to the magnetic field. Clearly, QLM conditions are more accessible in Dirac systems. Since these Dirac pockets are reported to be small and have a very low carrier density of the order 10^{-3} per Fe [142], it also favors the QLM condition (see equation (1.1)), which is probably why the linear magnetoresistance is widely believed to be arising due to the existence of Dirac cone states, which is supported by the fact that LMR is pronounced in the magnetic state, where Fermi surface reconstruction results in the formation of small Dirac pockets [143, 140, 164, 146, 165].

In summary, we briefly introduced the iron-based superconductors. Also, some key concepts and issues in iron-based superconductors are highlighted. The structure of this thesis has been outlined in this chapter. In the following chapters, the work carried out in this thesis is presented.

Chapter 2

Single crystal growth, Characterization & Techniques

2.1 Introduction

Single crystals are vital to study the intrinsic physical properties of materials. Certain physical phenomena are almost always masked by the presence of even small amounts of impurities and imperfections, which are more common in polycrystalline specimens than single crystalline ones. For example, the presence of variously oriented grains masks the intrinsic anisotropic properties of crystalline materials. Similarly, the presence of grain boundaries introduces undesirable effects in the transport measurements.

A number of crystal growth techniques exist; however, the melting behavior of material largely dictates the choice of growth technique. Some systems can be grown by melting the material and letting it cool slowly; this is called the melt growth. In some cases, where a substance decomposes into other phases upon heating, other techniques, like, vapor transport can be employed. In solution growth methods, the desired material is dissolved in a solvent (also called flux) to the extent of supersaturation. Upon slow cooling, the single crystals of the desired material are precipitated out of the solution. High-temperature solution growth requires dissolving the targeted material in a solvent at high temperatures; however, at temperatures lower than the melting point. It is suitable for the growth of both congruent as well as non-congruently melting materials. Growing single crystals at temperatures lower than their melting temperature lead to a lesser density of defects. However, choice of an appropriate solvent (or flux) is vital in this case. If the solvent used is a component of the material under consideration then it is called the self-flux method. For example, if $BaFe_2As_2$ is grown using FeAs as a solvent, then it is called a self-flux method. But a solvent which is not a component of the material to be grown is also frequently used. An example of this is the growth of $BaFe_2As_2$ using Sn as a solvent [166]. Another variant of solution growth is the hydrothermal technique. In a hydrothermal growth, extreme conditions like high temperatures and pressures are often employed. This method is particularly suitable for materials which are difficult to grow using other techniques, or are unstable at ambient conditions, and/or have a high vapor pressure. High pressure synthesis technique, using FeAs as a solvent has been employed to grow sub-millimeter size single crystals of $ReFeAsO_{1-x}$ (Re: rare earth metal) [167, 168] and $SmFeAsO_{1-x}F_x$ [169].

All single crystals studied in this thesis were grown using the high-tempera -ture solution growth technique using FeAs self-flux. In this method, FeAs, which is taken in excess, acts as a solvent. In literature, other fluxes like Sn [170, 171], NaCl/KCl [172, 173], NaAs [174] and Pb [175] were also used to grow iron-based superconductors (See [176] for a summary). However, these solvents not only tend to wet the surface of the grown crystals [177], but, even replace Fe [170] or Ba [171] in the crystal structure. Also, the magnetostructural transitions are reported to be highly suppressed in the non-self-flux grown single crystals [166, 45]. In essence, often (not always) the single crystals grown using a self-flux are relatively purer than the crystals grown using other solvents [177]. We had tried several combinations of starting materials to grow the single crystals of $Ba(Fe_{1-x}Co_x)_2As_2$. Two of them were most successful, and both of them are described in this chapter. However, before describing the single crystal growth methods, the synthesis of precursor materials used in different methods of crystal growth is explained.

2.2 Synthesis of FeAs, Fe_2As and Co_2As

All three of these precursors were synthesized in a very similar manner. The purpose was not to make poly or single crystalline phases of these precursors but to react As with Fe or Co, to avoid the high vapor pressure of elemental Arsenic during the crystal growth which can rupture the quartz ampoule. Arsenic is known for its toxicity and high vapor pressure even below its sublimation point. Thus taking unreacted Arsenic can pose a severe security risk to the environment as well as lab members. Starting materials were as follows: Fe powder (99.9+%, Alfa Aesar) or granules (99.98%, Alfa Aesar), As lumps (Alfa Aesar 99.9999%) and Co powder (99.8% Alfa Aesar). Fe (or Co) and As lumps were ground and mixed using an agate mortar and pestle inside an Argon filled Glovebox. This powder was then transferred to an alumina crucible which was housed in a quartz ampoule. This ampoule was

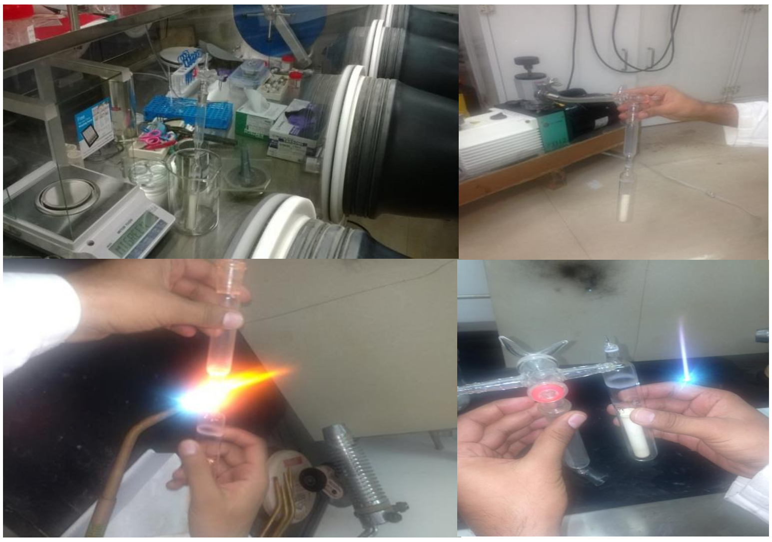

Figure 2.1: Upper left panel depicts the interior of an eight-port Argon filled Glove Box from MBRAUN, Germany. The entire process of weighing, mixing and grinding was carried out in this Glove Box. Upper right panel shows the evacuation process using a rotary pump dedicated for ampoule sealing work. The lower left panel depicts the sealing of a quartz ampoule using an acetylene-oxygen torch. In the lower right panel, a sealed ampoule is shown.

then closed using airtight (vacuum compatible) cock and brought outside for evacuation. After evacuation (10^{-3}-10^{-5} Torr, the partial pressure of Argon)[1], ampoule was sealed using O_2-Acetylene flame. This entire process of storage, mixing, grinding, and sealing is summarized in Figure 2.1. Typically, the ampoule was heated to 450-550°C for 6 hours and kept there for 12 hours. This was done to make sure that some Arsenic is already reacted before the temperature is further increased in the next step of the reaction where it was subsequently heated to 700-750°C within 3-4 hours and kept there for 12-24 hours. After that, the furnace was quickly cooled down to room temperature at 300°C/h. The result of the reaction was a solidified ingot which was not very difficult to grind. The temperature profile used for the reaction was very similar for FeAs, Fe_2As and Co_2As. Binary phase diagram of Fe-As and Co-As is shown in Figure 2.2 and 2.3 respectively. These diagrams provide essential information about the melting behavior of these systems, which is crucial to not only synthesize these precursors but even in the synthesis of single crystals of many iron-pnictide systems including the $Ba(Fe_{1-x}Co_x)_2As_2$

[1]to obtain pressures of $\sim 10^{-5}$ Torr, a different vacuum pump: HiCube 80 Classic, PFEIFFER, Germany was employed.

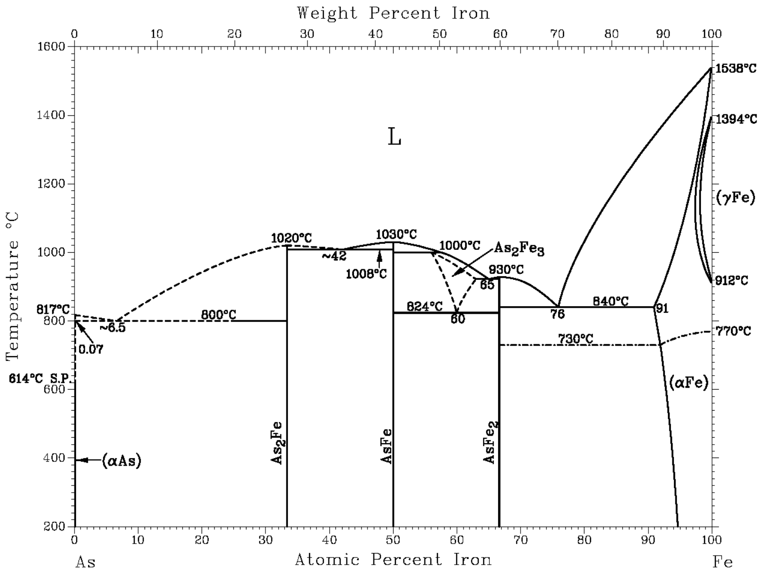

Figure 2.2: Binary As-Fe phase diagram (Copyright ©1996 ASM International [ASM (1996)])

system whose growth we will discuss in this chapter.

2.3 Synthesis of BaAs$_x$: (x = 1, 3.2)

BaAs was synthesized using the vapor transport method similar to the one used by Aswartham et al., [178]. High purity As (Alfa Aesar, 99.9999%, lumps) and Ba(99+%, Alfa Aesar, metal basis, rod) were utilized in all the reactions of barium and arsenic. Since the reaction of arsenic and alkaline earth metals (Ba, Sr etc.) is extremely exothermic and explosive, they could not be reacted directly. A special ampoule was designed for this purpose. In this ampoule, the Ba pieces were kept in a thick-walled and long alumina crucible[2] (which was housed in a thick quartz ampoule) and arsenic was kept in the space between alumina crucible and the quartz ampoule, as shown schematically in Figure 2.4. The ampoule was sealed at 10^{-3} - 10^{-5} Torr partial pressure of Argon. In this specially designed ampoule, As and Ba pieces are physically separated to avoid direct contact. The reaction was carried out in a slow and controlled manner. The ampoule was heated to 500-590°C in 10-12 hours and the setup was kept at this temperature for 12 hours. Even though the Arsenic sublimes at 615°C, it has considerable vapor

[2]Length, diameter and thickness = 6 cm, 3.6 cm and 2.5 mm respectively.

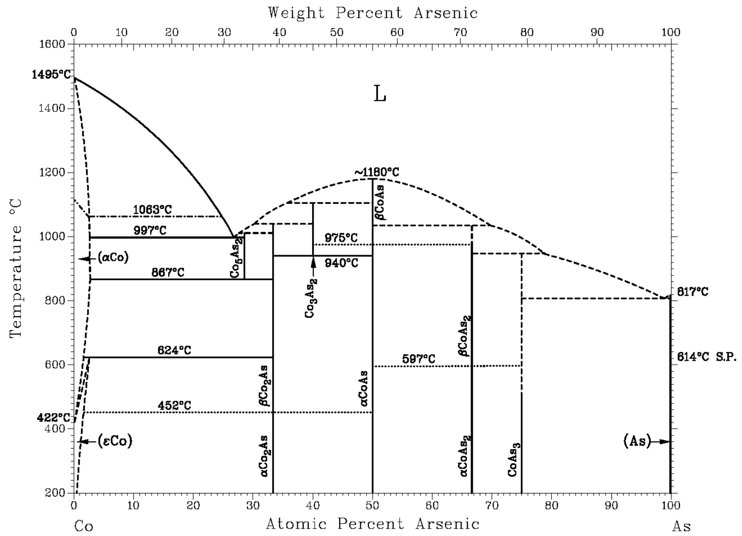

Figure 2.3: Binary Co-As phase diagram. (Copyright ©1996 ASM International [ASM (1996)])

pressure even at lower temperatures (for instance, 1 kPa at 433°C [179]). At these temperatures, Arsenic vaporizes and is adsorbed on the surface of Ba pieces, this ensures that vapor pressure of Arsenic remains low enough. It is essential since large amounts of heat and internal pressure may lead to explosion of the quartz ampoule (which can happen if temperature is raised rapidly to its sublimation point: 615°C). The temperature was then increased to 650-700°C at 10°C/hour and kept there for another 2-4 days. The furnace was cooled down to room temperature at 150-200°C/hour. Barium metal which is quite malleable and sticky turns brittle and easy to grind after the reaction. We observed that if bigger pieces of Ba are taken in the reaction, their interior remains unreacted even if all the Arsenic used in the reaction is exhausted. It suggests that As reacts on the surface of Ba granules and once a layer of $BaAs_x$ is formed, it prevents further diffusion of As into the Ba granules. Waiting at 650-700°C for longer time periods leads to less (or no) unreacted Barium. $BaAs_{3.2}$ was synthesized using the same method as described above, but with a different temperature profile. It is because the amount of As used to synthesize $BaAs_{3.2}$ is larger compared to what is used to synthesize BaAs. Hence, the highest temperature used in the synthesis of $BaAs_{3.2}$ was much lower than that was used in the synthesis of BaAs. The ampoule was heated to 370°C in 6 hours, and this temperature was maintained for 1.5-2 days. In the next step, the temperature was increased to 520°C in 30 hours. This temperature was maintained for 2.5-3 days. The

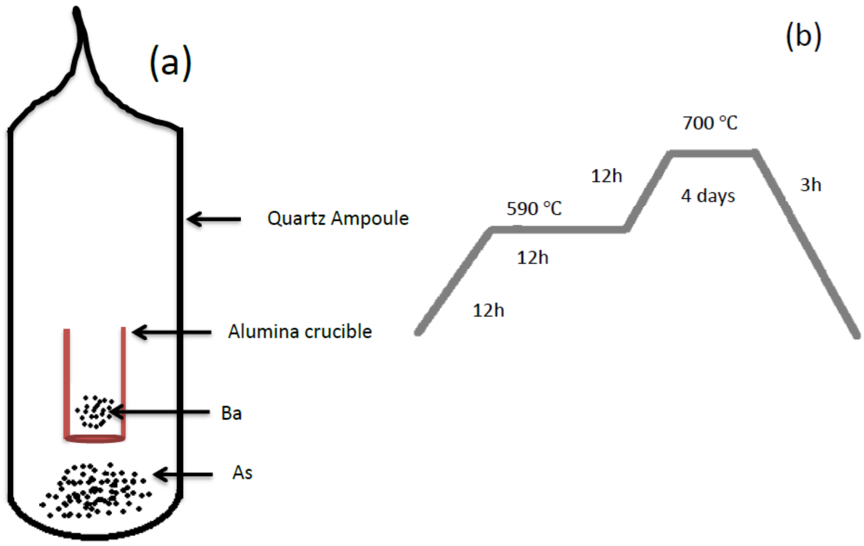

Figure 2.4: In (a), Schematic of the ampoule used to synthesize the $BaAs_x$ (x = 1, 3.2) is shown. In (b), a typical temperature profile used during the synthesis of $BaAs_x$ is shown.

furnace was then cooled down to room temperature in 3-4 hours. Other compositions of $BaAs_x$ (x other than 3.2 or 1) were also prepared during the process of optimization of crystal growth parameters. It is interesting to note that although only a few stable phases of Ba and As (Ba_3As_{14}, $BaAs_3$, Ba_3As_2 and Ba_5As_3 and Ba_2As [180]) are known to exist, (binary phase diagram of Ba-As, Ba-Co is not known [180]), however, strong affinity of As to react with Ba makes it easy to prepare the mixture (not a compound) of virtually any composition of $BaAs_x$ ($1 \leq x \leq 5.5$ in our experiments).

2.4 Single crystal growth of $Ba(Fe_{1-x}Co_x)_2As_2$: Method one

In this method, starting precursors were: BaAs, FeAs and Fe_2As. An additional precursor Co_2As was also used when Co substituted $BaFe_{2-x}Co_xAs_2$ was made. Many times instead of making Co_2As, Co and As powders were simply added to the mixture of the rest of the precursors. The composition of the entire mixture was $BaFe_{3.2-x}Co_xAs_{3.2}$(here x is the desired composition). All the precursors were grounded thoroughly and mixed using an Agate mortar and pestle inside an Argon filled glove box, which utilizes a highly purified Ar gas (99.999% purity from INOX, India) and maintains O_2 and moisture levels below 0.1 parts per million at all times. This mixture was then transferred to an alumina crucible and was gently pressed using a glass rod to avoid the loss of finely ground powder during the evacuation process. It is should be noted that Alumina crucible was already housed in an especially designed quartz tube. The ampoule was sealed using an O_2-Acetylene torch at 10^{-3}-10^{-5}torr partial pressure of Argon. In a typical crystal growth experiment, the mixture was heated to 700°C in 7-10 hours and held at this temperature for 6-10 hours. After that, the temperature was raised to ~1180°C in 5 hours and this temperature was maintained for 24 hours. Waiting for 24 hours at 1180°C ensures the homogenization of the melt. After that, slow cooling of the melt (1-2°C/h) is initiated until the temperature reaches ~1000°C. Crystal growth takes place in this temperature window (1180-1000°C). Growth was kept at this temperature for another 1-3 hours, and then a rapid cooling (~300°C/h) was initiated to cool the furnace to room temperature. The chemical equation summarizing the single crystal growth is as follows:

$$\begin{aligned} BaAs + (1-x)Fe_2As + xCo_2As + 1.2(FeAs) &\longrightarrow BaFe_{3.2-2x}Co_{2x}As_{3.2} \\ &\longrightarrow Ba(Fe_{1-x}Co_x)_2As_2 + leftover \end{aligned}$$

The end result was a solidified ingot. Crystals were extracted mechanically using a razor blade. Some representative images of grown crystals are shown in Figure 2.5.

2.5 Single crystal growth of $Ba(Fe_{1-x}Co_x)_2As_2$: Method two

In this method, $BaAs_{3.2}$ was used as precursor instead of BaAs. Other precursors like FeAs and Fe_2As were not needed. Fe and/or Co powders were simply added to $BaAs_{3.2}$ and ground together. Rest of the process is very similar to method one i.e., temperature profile, sealing procedure, the vacuum level in the ampoule, etc. were kept same. The chemical equation that summarizes the reaction is:

$$\begin{aligned} BaAs_{3.2} + (3.2-2x)Fe + 2xCo &\xrightarrow[\text{end result: homogeneous melt}]{\text{dwell 24 h at 1180°C}} BaFe_{3.2-2x}Co_{2x}As_{3.2} \\ &\xrightarrow[\text{crystals begin to form}]{\text{slow cooling starts here}} Ba(Fe_{1-x}Co_x)_2As_2 + leftover \end{aligned}$$

Because of its simplicity, we had used method 2 more than method 1. Another advantage of method 2 is that Arsenic only needs to be reacted with

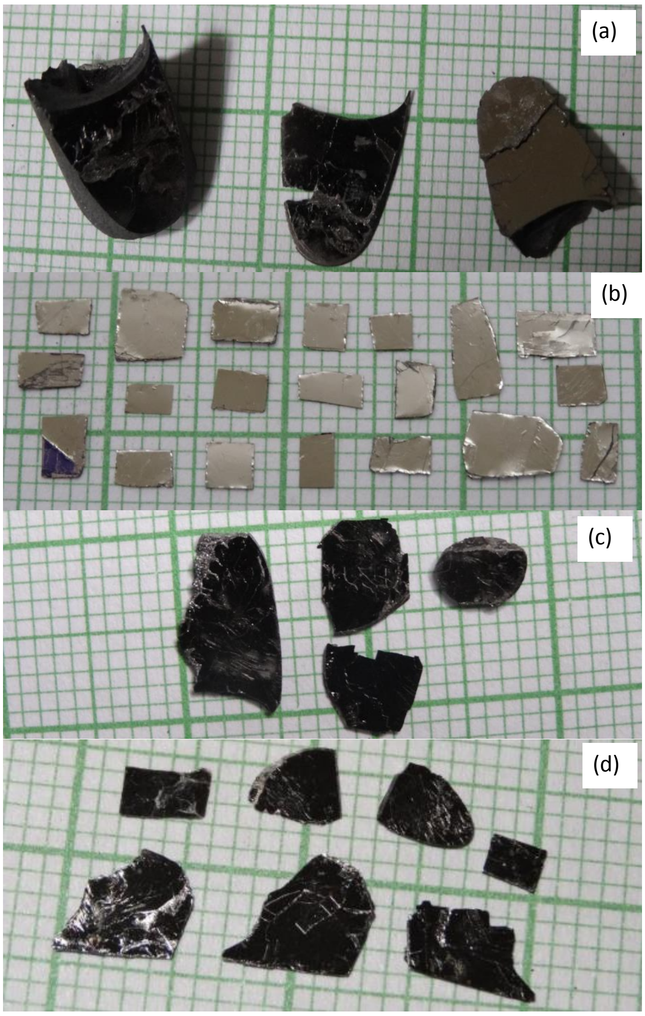

Figure 2.5: Some representative images of grown crystals are shown here. Panel (a) shows a cleaved ingot (3.8% Co) along the length of the crucible, implying that the diameter of the crucible limits the size of grown crystals. Panel (b) depicts the flux-free crystals extracted from the same ingot and cut in rectangular geometry. (c) depicts some extracted single crystals from the growth of an optimally doped composition (7.4% Co). Panel (d) shows the single crystals of $BaFe_2As_2$ obtained from a different growth. In this growth the size of the grown crystals was not large, but the yield was better.

Ba (which seems to have a strong affinity for Arsenic), so chances of having unreacted Arsenic in crystal growth experiments are lesser, which makes the growth a little more predictable and safer if rest of the growth parameters are already optimized. It should be noted that the properties of crystals synthesized by both methods are identical. Single crystals of most 122 families grow along the crystallographic *ab* plane, have plate like morphology, and tend to exfoliate easily. Also, the crystals of $Ba(Fe_{1-x}Co_x)_2As_2$ are brittle and break easily.

2.5.1 Some important steps taken while preparing quartz ampoules for synthesis work

Almost always, quartz ampoules were sonicated using an organic liquid like Acetone or Ethyl Alcohol to remove any impurities that may be present on the surface of alumina crucible and quartz ampoules.

These washed ampoules were preheated (up to 900°C) overnight to remove moisture that may be adsorbed on the walls of alumina crucible and/or quartz ampoules. Sometimes the ampoules were also evacuated (while being preheated) using a vacuum pump. The pressure of the ampoule was monitored using a pressure gauge. It was found that pressure increases when the temperature reaches approximately 300°C. It suggests that adsorbed moisture gets desorbed at this temperature. Keeping the ampoule at higher temperatures (800-900°C) overnight ensures that all the adsorbed moisture (and possibly other impurities too) is desorbed and sucked out through the evacuation process. We observe that preheating the quartz ampoule too fast often leads to the blackening of alumina crucible inside it. This is so because the leftover organic liquid (Acetone or Ethyl Alcohol) used in the sonication process, burns when heated quickly and leaves Carbon as a residue. Such impurities can get added to the crystals and should be avoided. Keeping the ampoules at 70-80 °C for half an hour before heating to higher temperatures solves this problem entirely. However, an additional method for preheating was also used. In this method, the quartz ampoule was heated at 900°C in a tube furnace (from Nabertherm). It was then pulled out to the open end of the furnace and kept there for some time to allow it to cool down to a temperature close to 100°C. At this point, it was closed using a cork and transferred immediately to the antechamber of the Glove Box, which was quickly evacuated and refilled with high purity Argon gas.

2.6 Characterization & Techniques

Many experimental techniques were employed to characterize single crystals before they could be used in detailed magnetotransport measurements. Typically, the EDAX analysis, Powder X-Ray and Laue diffraction were carried out first. Subsequently, the transport, magnetization (7 T MPMS, Quantum Design, cryo-free), and thermodynamic measurements (9 T PPMS, Quantum Design, cryo-free) were carried out. In addition to this polarized light microscope was extensively used to screen single crystals before selecting for magnetotransport, specific heat, and magnetization measurements.

2.6.1 X-Ray & Laue diffraction

X-Ray Diffraction

The X-ray diffraction on the powdered single crystals was carried out using a Bruker D8 advance X-Ray diffractometer using the Cu K_α radiation. The purpose was to check the phase purity of the crystals and to determine the lattice parameters and their consistency with the literature. Several crystals pieces extracted from the as grown ingot were ground using Agate mortar and pestle. The diffraction pattern of a representative parent compound is shown in the left panel of Figure 2.6. The diffraction pattern was analyzed by the Leibel method using the FULLPROF suite [181]. All the peaks can be very well fitted by the tetragonal I4/mmm space group consistent with literature [182, 183, 184]. The single crystal specimens were mounted with their ab-plane as the diffraction plane in Bragg-Brentano geometry. In this case, only the (0 0 2l) reflections were observed as can be seen in the right panel of Figure 2.6. Lattice parameters for three representative compositions of the series are shown in Figure 2.7. As is evident, most prominent change is observed in the 'c' parameter which gets suppressed quickly by cobalt doping. The lattice parameter 'a' remains almost unchanged, as reported in these systems [183, 184, 182].

Laue Diffraction

Laue diffraction on the single crystals was regularly carried out using a diffractometer from Photonic Science. It utilizes a Tungsten white source (0.35 Å-2.5 Å). Typically, in the Laue method, a single crystal specimen is illuminated with white X-rays, and backscattered radiation is collected by a detector. Primarily, Laue pattern is used to align the single crystals, which is essential for the determination of intrinsic anisotropic properties of single crystals. Laue pattern can also indicate the symmetry of a single crystal.

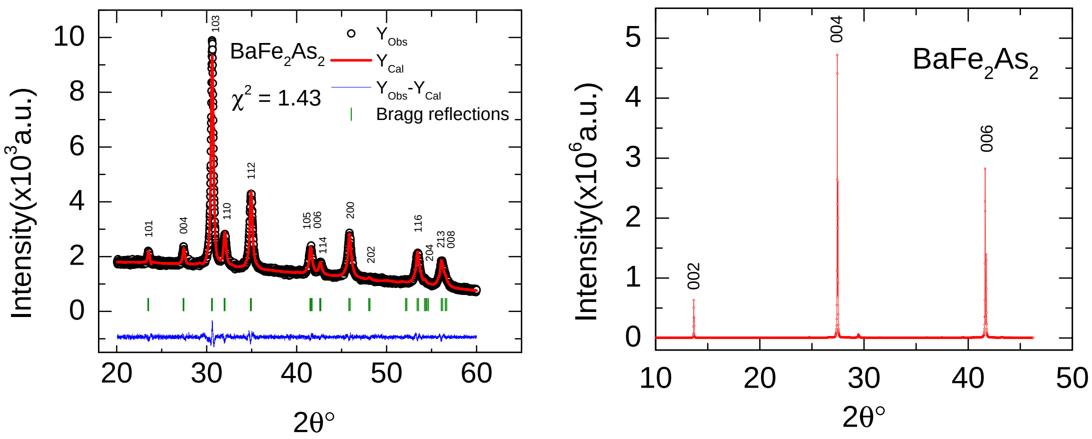

Figure 2.6: Left panel shows the XRD pattern analysis. Y_{Obs} and Y_{Cal} represent experimental data and simulated pattern. Y_{Obs}-Y_{Cal} is the difference between the experimental data and the simulated pattern. Small vertical bars (Olive color) represent the positions of the expected Bragg reflections. Most peaks are labeled: for clarity, few peaks which are very small and/or are very close to the neighboring peaks are not labeled. The right panel depicts the X-Ray diffraction pattern of a single crystal, which was mounted with its crystallographic *ab* plane as the plane of diffraction in the Bragg-Brentano geometry.

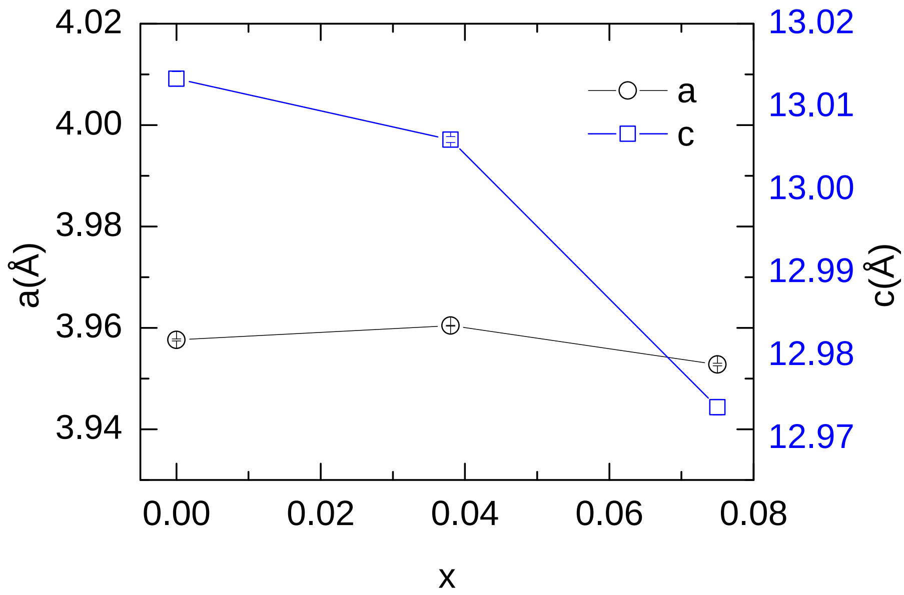

Figure 2.7: Lattice parameters a (black) and c (blue) are plotted on the left and right axes respectively. x represent the doping level in $Ba(Fe_{1-x}Co_x)_2As_2$.

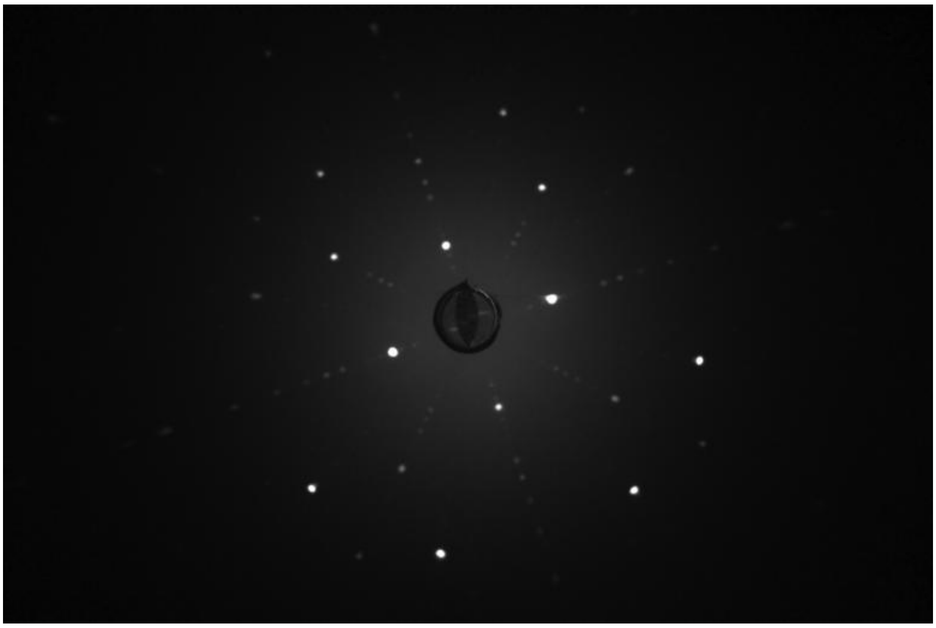

Figure 2.8: Laue diffraction pattern for an underdoped specimen ($x = 0.038$) of $Ba(Fe_{1-x}Co_x)_2As_2$ series.

For example, if a specimen is mounted in such a way that only the (1 1 1) planes are facing the white light, Laue spots will have threefold symmetry. Also, as mentioned previously, iron-based superconductors have a plate like morphology, i.e., their crystallographic c axis is perpendicular to the crystals. So, a crystal mounted in such a way that white X-ray radiation falls on its ab plane perpendicularly; a fourfould symmetric Laue pattern will be observed which arises from the diffraction from a set of parallel (0, 0, 2l) planes (see Figure 2.6, right panel.).

Laue diffractograms can also provide information about the quality of a single crystal. For instance, good quality crystals are known to produce sharp spots, whereas Laue spots from the deformed samples are elongated. Figure 2.8 shows Laue diffraction pattern for a representative specimen of underdoped composition ($x = 0.038$) of $Ba(Fe_{1-x}Co_x)_2As_2$ series. Sharp spots suggest that this is a good quality specimen.

2.7 Energy Dispersive X-Ray Spectroscopy (EDX)

Each batch of crystals growth was characterized using the EDX technique (Energy Dispersive X-Ray Spectroscopy) to determine the actual composition of grown crystals and to analyze the surface morphology. When a sample is bombarded with high energy electrons; it can knock out electrons from the inner shells of the atoms. This can lead to a cascade of transitions, and in the process, X-Ray photons are emitted from the sample. Since the X-rays emitted from an element are characteristic of it, measuring the energy and intensity of the emitted X-Rays allows for the determination of elements present in the sample. EDX can be used to investigate the incorporation of flux and other possible contaminants on the surface of crystals. Sometimes, other secondary phases which might show a different color contrast than the sample can also be detected. Determining the composition of these secondary phases can not only provide valuable information about them but can also help in eliminating these phases in future crystal growth experiments.

Crystals were mounted on a double-sided conducting carbon tape before loading onto a metallic sample holder. Few drops of Acetone or Isopropanol are enough to set carbon tape loose; hence it is a good choice to be used as a conductive adhesive ($BaFe_{2-x}Co_xAs_2$ single crystals are easily cleaved along ab plane; hence mechanical pulling is not recommended). The samples were then inserted into the sample chamber of the Scanning Electron Microscope. After several purging and refilling (using an inert gas) cycles, samples are

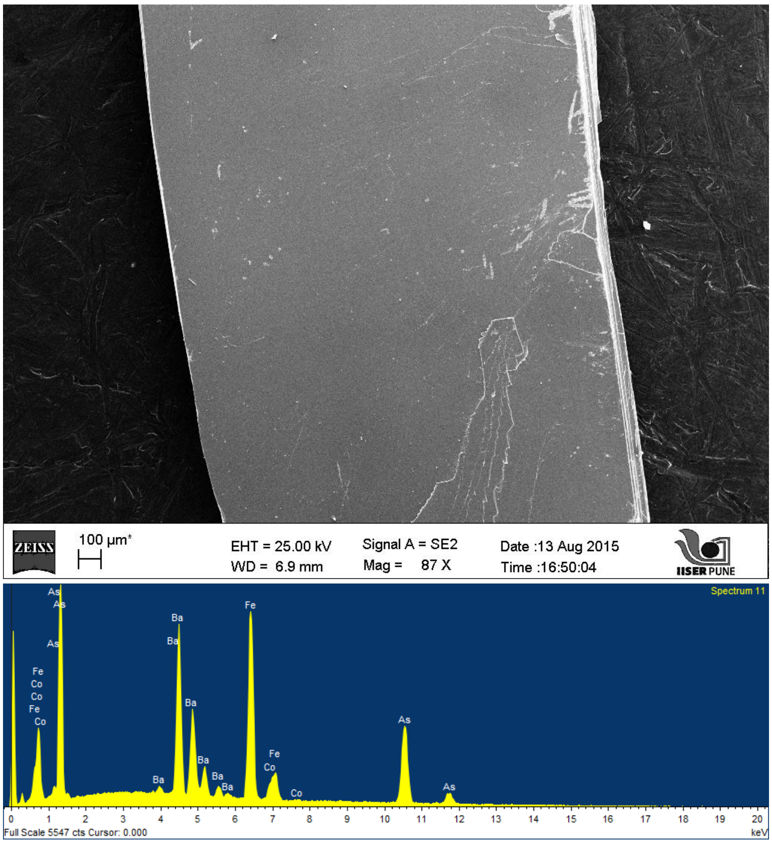

Figure 2.9: Upper Panel: SEM image of a single crystal $Ba(Fe_{1-x}Co_x)_2As_2$ with $x = 0.074$. Relevant parameters are listed at the bottom of Image. Lower panel: representative EDX spectra, indicating that no foreign phases are present in the sample.

brought to the focus, ready to be bombarded by the electron beam. We typically used one minute integration time (the time for which sample surface is exposed to the electron beam) at each spot on the sample surface, and the used voltages were in the range 20-25 KV. Data was collected on 8-20 data points on the surface of each sample and composition was determined by taking the average of these data points. The upper panel of Figure 2.9 shows a representative SEM image of a portion of an optimally doped ($x = 0.074$) $Ba(Fe_{1-x}Co_x)_2As_2$ single crystal. It is clear that the crystal surface is free from any foreign impurities or flux. The lower panel shows representative EDX spectra taken at one point (out of 10-20 data points) on the surface. No signs of impurities or other elements (i.e., other than Ba, Fe, Co and As) could be detected. Figure 2.10 shows the variation of cobalt concentration (as determined from EDX) plotted against nominal cobalt concentration. The

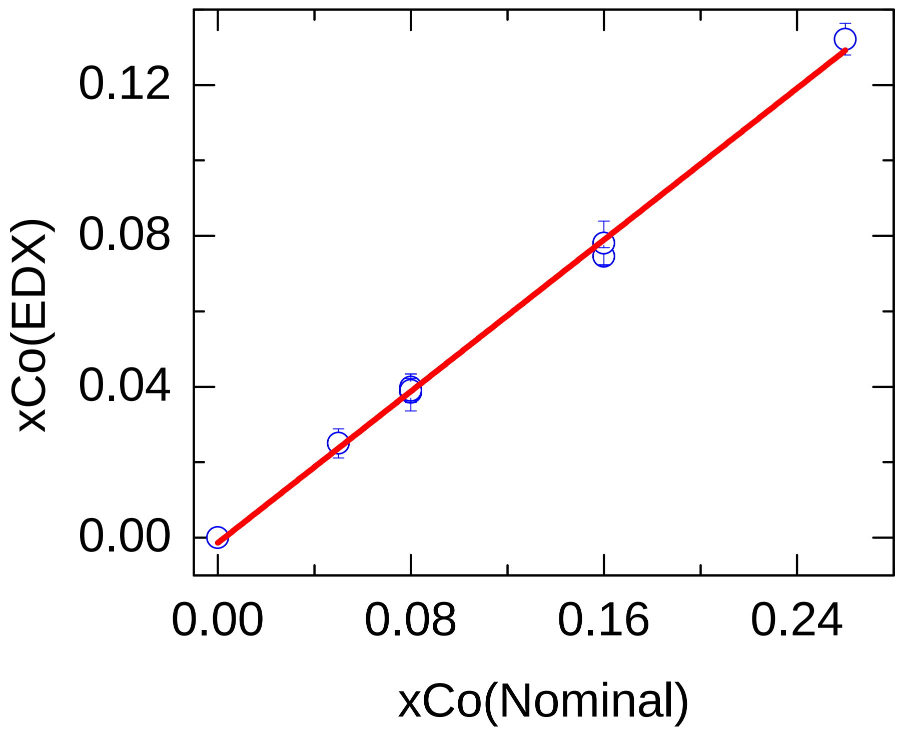

Figure 2.10: Co concentration in $Ba(Fe_{1-x}Co_x)_2As_2$ as determined from EDX is plotted on Y axis whereas nominal composition is on X axis. Data on both axes is plotted in atomic%.

plot is a straight line with slope ~ 0.5. Error bar for each composition is the standard deviation of the data taken at 8-20 different points of the crystal. Note that the several samples of very similar compositions from different batches of underdoped ($\approx 3.8\%$ Co) and optimally doped ($\approx 7.4\%$ Co) compositions are shown in Figure 2.10, which is the reason for some overlapping data points. This indicates that samples are very homogeneous. In rest of the manuscript, we will use (and refer to) only the actual compositions of these crystals determined by EDX, and not the nominal ones.

2.8 Magnetization

Magnetic measurements were carried out using a ± 7 Tesla Quantum Design Magnetic Property Measurement System (MPMS XL) using the Reciprocating Sample Option (RSO) [185, 186]. MPMS employs an rf-SQUID, which forms a closed loop with the so-called pickup coils. Pickup coils are a group of 4 coils, with inner two coils in close proximity. This is done to cancel external magnetic field fluctuations. These pickup coils are located at the center of a superconducting solenoid, which is the source of the magnetic field needed for magnetic measurements. Sample motion through the pickup coils leads to the change in flux associated with them and this flux change leads to a current. The SQUID output is this current converted into voltage, which is used to compute magnetic moment of the sample. To avoid magnetic field fluctuations due to environmental noise, the SQUID is encased in a superconducting material (Niobium). SQUID is a very sensitive tool for detecting magnetic fields. It has a sensitivity of $\approx 5\times10^{-9}$ emu (sensitivity decreses to $\approx$ 6 $\times10^{-6}$ emu for magnetic fields above 2.5 T [187]) in the RSO option when sample is centered at the center of pickup coils [185]. In this case, sample oscillates around the center of pickup coils (using the servo motor).

Magnetic measurements are vital not only for the characterization of samples, but also to track the improvement in the crystal growth conditions as well. In all magnetic measurements, the magnetic field was applied along the crystallographic *ab* plane (unless otherwise stated). Figure 2.11 shows the magnetic measurements carried out on three different samples of parent compound, i.e., $BaFe_2As_2$ from three different growth experiments. Parent compound undergoes a combined magnetic/structural transition at $\sim$ 134 K [37], which is evident by the drop in susceptibility (see Figure 2.11(a)) at 134 K. Inset of Figure 2.11(a) shows the derivative of susceptibility for all three samples, which again shows that only one anomaly at 134 K is present, suggesting that magnetic and structural transitions coincide. Figure 2.11(b) depicts, M-H isotherms at 300 K for all three specimens shown in Figure 2.11(a). Linear isotherms suggest that there are no ferromagnetic impurity phases present whose ordering temperatures are around 300 K; otherwise, we would see a small hysteresis loop in M-H isotherms. The anomaly at $\sim$ 50 K for the sample BFBS110D is due to the oxygen contamination of the sample chamber. When parent compound is doped with electrons (by replacing Fe with Co), magnetostructural transitions, which were concomitant in the parent compound, gets suppressed and separated, and superconductivity emerges out of the magnetically ordered ground state [18, 188, 189]. Further doping leads to complete suppression of magnetic/structural transitions at around x $\sim$ 0.07, at which point the maximum superconducting transition temperature is observed in this series ($BaFe_{1-x}Co_xAs_2$) at $\approx$ 25 K.

Figure 2.12 shows magnetic measurements on several samples from the same batch of underdoped composition (3.8%Co). Figure 2.12(a) shows χ vs. T from 2-300 K for two different samples of the same composition from

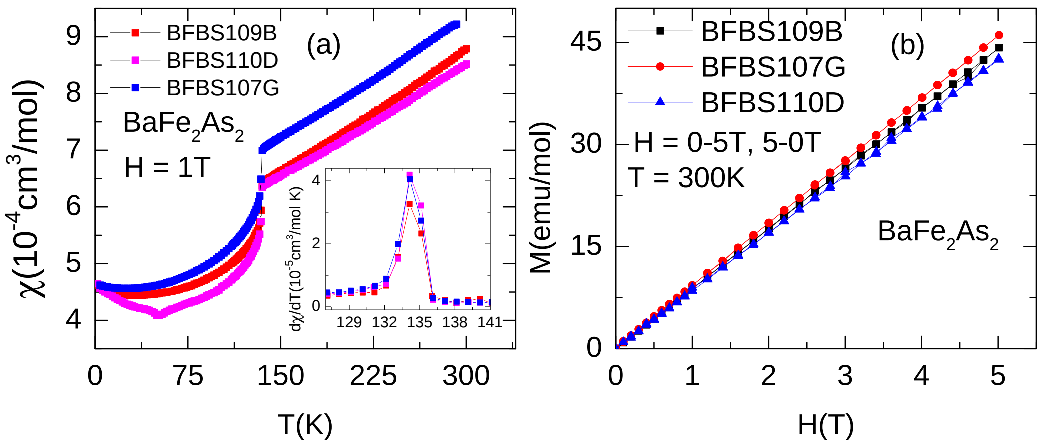

Figure 2.11: Magnetic susceptibility as a function of temperature for three representative single crystalline specimens of parent compound $BaFe_2As_2$ is shown in the left panel of Figure 2.11. The derivative of magnetic susceptibility for respective specimens is shown in the inset. The right panel shows M-H isotherms from 0-5 Tesla and 5-0 Tesla magnetic field cycle. The magnetic field was applied along the crystallographic *ab* plane. All three samples of $BaFe_2As_2$ in Figure 2.11 are from different batches of crystal growths. BFBS109B etc. are the names of samples.

the same batch. The inset shows the derivatives of susceptibility for only one sample: BFBS115D. Two obvious anomalies in the derivative can be identified with structural (T_S) and magnetic transitions (T_S). It should be noted that the anomalies identified by the derivatives of resistivity and susceptibility are in agreement with neutron diffraction experiments carried out on similar compositions [47, 40]. The right panel of Figure 2.12 shows superconducting transition temperatures for three different samples (including the two samples shown in Figure 2.12(a)). It is clear from Figure 2.12(b) that superconducting transition temperatures are in agreement in all three samples. Also, the value of volume susceptibility reaches ≈ -1 for all specimens, which indicates highly homogenous samples with 100% superconducting volume fraction. Our results are similar to the literature reports for similar compositions [44, 188, 189, 178]. In the optimally doped systems, magnetostructural transitions are fully suppressed, and superconductivity is strongest [18]. Figure 2.13 shows ZFC & FC plots at 20 Oe magnetic field. The superconducting transition occurs at around 20.5 K. Volume susceptibility (χ_v) is a dimensionless quantity in Gaussian units (see [18] for discussion). When multiplied by 4π, one gets the superconducting volume fraction. For a superconductor, superconducting volume fraction should be -1 when Meiss-

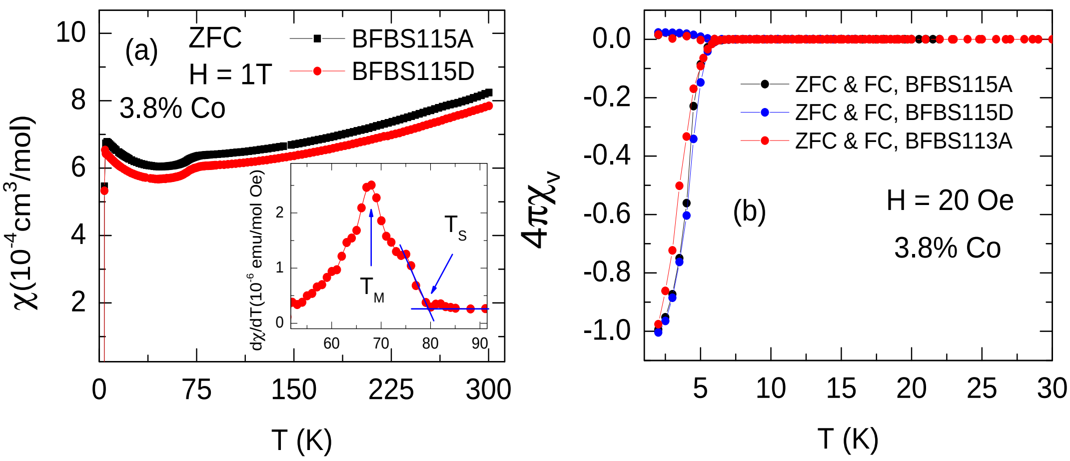

Figure 2.12: In (a), zero field cooled (ZFC) magnetic susceptibility χ is plotted as a function of temperature for two samples of underdoped composition (3.8% Co). Inset of (a) depicts the first temperature derivative of χ, which clearly shows two anomalies designated as T_M and T_S corresponding to magnetic and structural transition temperatures respectively. In (b) Field cooled (FC) as well as zero field cooled (ZFC) volume susceptibility (multiplied by 4π) for three samples of the underdoped composition is plotted as a function of temperature. $4\pi\chi_v$ gives a direct estimate of superconducting volume fraction. The magnetic field was applied along the crystallographic ab plane in both (a) and (b)

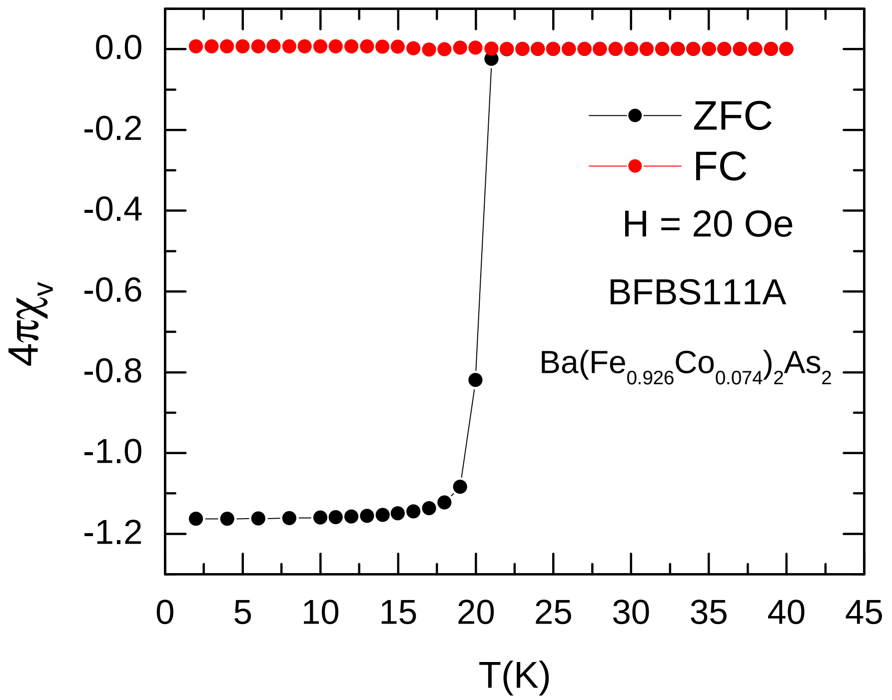

Figure 2.13: Volume susceptibility in Zero Field Cooled (ZFC) and Field Cooled (FC) sweeps for a single crystal specimen BFBS111A of an optimally doped system ($x = 0.074$). These measurements were carried out in 20 Oe magnetic field, as depicted in the inset. The magnetic field was applied along the crystallographic ab plane.

ner screening is complete. However, as we can see from Figure 2.13 that the superconducting volume fraction is more than -1. It can be due to the demagnetization effects. Volume fraction in excess of -1 are often reported in literature [188, 190, 191, 192, 193]. It is usually found that optimally doped systems have $4\pi\chi_v > -1$ more so than underdoped systems. It is because superconductivity is much strong in optimally doped systems; which combined with demagnetization effects can lead to apparently larger Meissner fractions.

2.9 Electrical Transport

Transport measurements were routinely carried out to characterize samples. A ±9 Tesla Quantum Design Physical Property Measurement System (PPMS, model 6000) was used for this purpose. Measurements were either carried using DC resistivity option in standard four-probe geometry (I = 5 mA) or the ACT transport option (I = 5 mA, f = 17 Hz) in five probe geometry. DC option allows for the simultaneous measurements of three samples in four probe configuration, where a precision current source is used to supply the excitation current in 5 nA - 5 mA range, with an output voltage sensitivity of 20 nV. In the ACT option, where two samples can be measured simultaneously, an AC current in 10 μA - 2 A with frequency range 1 Hz - 1 kHz can be applied, and it has a voltage sensitivity of 1 nV (at 1 kHz). Five probe method allows for the simultaneous measurement of magnetoresistance as well as Hall resistivity (ρ_{xy}) which are the symmetric and asymmetric components of the signal: $\rho_{xx} = [\rho(+H) + \rho(-H)]/2$ and $\rho_{xy} = [\rho(+H) - \rho(-H)]/2$. Here +H and -H represent the magnetic field applied parallel or antiparallel to the crystallographic c axis. All magnetotransport measurements were carried out in the transverse geometry, where H $\perp$ I, and $\parallel$ c. Contacts on the sample surface were made using a gold wire (25μ diameter) and silver epoxy. Contact resistance varied between <1Ω to 2 Ω. Contacts were cured for 5 minutes at $\sim$ 90°C in an oven or 10-30 min. in a dry box filled with silica gel.

We often carried out resistivity measurement on multiple samples before choosing the right sample for further comprehensive magnetotransport measurements. We observed that the sample quality can vary slightly even amongst the specimens of the same composition from the same batch. It can be due to various reasons. For instance, some samples can have more micro cracks (which are introduced during extraction, cutting and shaping these crystals for transport measurements [194]) than others. Also, some crystals might have little more surface oxidation as compared to the crystals

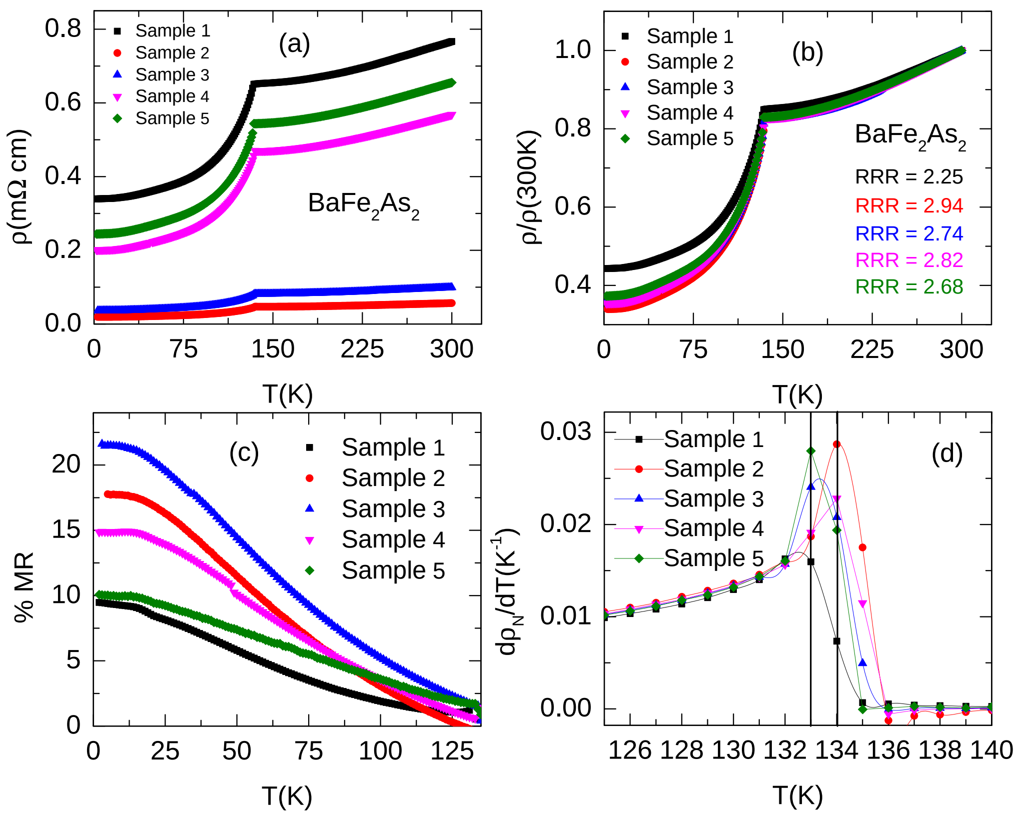

Figure 2.14: In (a), resistivity for five samples of parent compound $BaFe_2As_2$ from 3 different batches is shown. In (b), normalized resistivity ($\rho/\rho(300$ K) is plotted for all five samples. In (c) magnetoresistance for all five samples is shown in the low temperature magnetic state. In (d), first derivative of normalized resistivity (Figure 2.14(b)) is plotted. Vertical lines are drawn at respective magnetostructural transition temperatures.

from other batches (possibly, due to some leakage during the sealing process). However, in the later more advanced stages of crystal growth experiments, we were able to achieve consistency in the crystal yield as well as their physical properties. Figure 2.14 shows zero field resistivity of five samples of parent compound $BaFe_2As_2$ from three different batches. It is clear from Figure 2.14(a) that absolute values of resistivity have considerable spread amongst different samples. However, as we can see from 2.14(b), most of this spread is eliminated by plotting the normalized resistivity ($\rho/\rho(300K)$. Normalizing the resistivity removes the uncertainty arising from the geometrical structure factor which may come from a number of reasons. One reason would be from the uncertainty in determinations of sample dimensions as well as voltage probe contact area with the sample surface, which can affect the accurate determination of probe spacing. Additionally, the micro cracks, which can get created in these systems during the cutting and extraction process can also contribute to the geometrical structural factor; this effect has been discussed in the literature [194]. In the Inset of Figure 2.14(b), residual resistivity ratios (RRR) are depicted. Here, RRR is the ratio of resistivity at 2 K and 300 K (ρ(300K)/ρ(2K)).

RRR is a good measure of sample quality for simple metals. Though it is not true about complex multiband systems such as iron-based superconductors; it can still serve the purpose of comparing the quality of different samples from the same iron pnictide system. In Figure 2.14(c) magnetoresistance of all five samples is plotted in the antiferromagnetic state (2-135 K). Interestingly, highest magnetoresistance is not observed for the samples with the highest RRR ratio (see inset of Figure 2.14(b)). However, there is still some correlation between RRR values and magnetoresistance at low temperatures. For example, samples with lowest RRR values (Sample 1 and 5) indeed have the lowest magnetoresistance. It indicates that one should at least carry out transport as well as magnetic measurements on these systems before carrying out any detailed investigation of fundamental issues. In Figure 2.14(d) first derivative of resistivity is plotted near magnetostructural transition (T_{MS}≈134 K) for all five samples. The disorder seems to have a less pronounced effect on magnetostructural transition as compared to magnetoresistance. However, the sample with low RRR values (2.25 and 2.68) do have a low magnetostructural transition temperature (T_{MS} ≈133 K), whereas the samples with higher RRR values (2.94, 2.82 and 2.74) have higher T_{MS} (≈134 K). Transport measurements for underdoped and optimally doped compositions are summarized in Figure 2.15. Normalized resistivity (ρ/ρ(300K)) of two representative samples for underdoped composition is shown in Figure 2.15(a) and for three representative samples of the optimally doped composition is depicted in Figure 2.15(b). Normalized resistivity plots for multiple samples (of both compositions, independently) collapsed on top of each other, similar to what was seen for the parent compound. Magnetic and structural transitions can be identified in the derivative of resistivity (see inset of (a)) for the underdoped composition, just like they could be identified in the derivative of susceptibility (see inset of Figure 2.12(a)). Magnetic transition (T_M) occurs at ≈71.5 K whereas structural transition (T_S) is estimated at ≈84 K. The superconducting transition is defined at the onset of resistivity drop. It is taken at the intersection of two straight lines drawn on the data in the normal state just above the transition and the data during the superconducting transition. T_C is ≈ 11 K for both samples of the underdoped composition. T_C is ≈ 22 K for all three samples

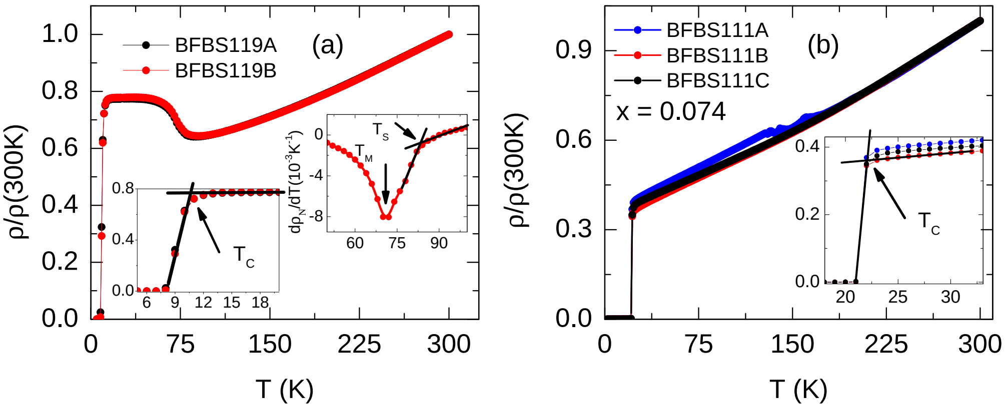

Figure 2.15: In (a), the normalized resistivity of two samples for the underdoped composition (3.8% Co) is plotted. In the upper inset, the first derivative of normalized resistivity is plotted. Arrows mark the structural (T_S) and magnetic (T_M) transitions. The lower inset depicts the estimation of superconducting transition temperature (T_C) which is marked by the arrow. In (b), normalized resistivity for three samples of the optimally doped composition is plotted. The inset depicts the expanded view of the superconducting region.

of the optimally doped composition (7.4% Co) which is shown in the inset of Figure 2.15(b). Extremely similar results for multiple samples of the same composition amongst different techniques (Magnetic and transport so far) again confirm the high quality of our crystals.

2.10 Heat Capacity

Thermodynamic measurements were carried out using a 9 Tesla, Quantum Design PPMS [195]. QD PPMS uses a relaxation technique to determine the heat capacity. Samples of mass between 1-200 mg can be used. It is recommended to use samples with a flat surface, to reduce the thermal path of the heat through the sample. To avoid any thermal leaks due to residual gas, a high vacuum is created in the sample chamber by using a charcoal cryopump (located above the sample puck). This results in pressures lower than 10^{-5} Torr. To determine the heat capacity of the sample, first, the heat capacity of the addendum is determined. The Addendum in our case is sample platform and high vacuum Apiezon N grease. Puck frame acts as a heat sink (see Figure 2.16). Eight thin conducting wires provide a thermal link between the sink and sample platform and also provides support to the

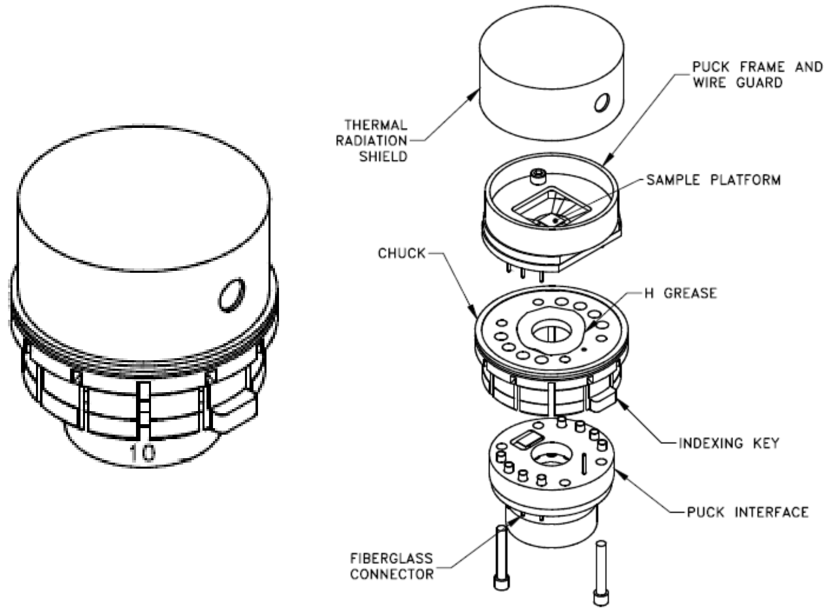

Figure 2.16: Heat capacity puck is shown in the left part of the figure. An exploded view of the puck is shown in the right portion of the figure. Image Source: User's manual, Heat Capacity option, Quantum Design PPMS (USA).

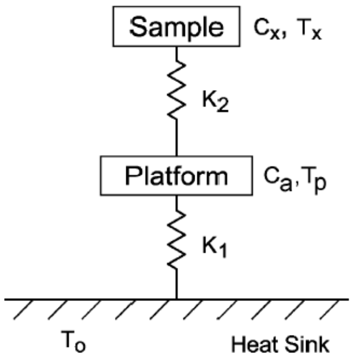

Figure 2.17: Heat flow diagram of a conventional relaxation calorimeter.

sample platform as well as the power to the thin film heater located at the platform [195]. Heat flow diagram of a conventional relaxation calorimeter is shown in Figure 2.17 (after [196]). C_x and C_a refers to the specific heat of the sample and platform respectively whereas T_x and T_p represent the respective temperatures. When the temperature of the platform is increased from T_0 to T in small steps of ΔT, and if the power to the heater is turned off, its decay can be fitted by the equation of the form:

$$T(t) = T_0 + \Delta T e^{(-t/\tau_1)} \tag{2.1}$$

Where $\tau_1 = C_a/K_1$, and K_1 is the thermal conductance between heat sink and the sample platform. When the sample has a very good thermal contact with the platform and sink, such that $K_2 \gg K_1$ (where K_2 is the sample-platform interface thermal conductance) then equation 2.1 still hold except, $\tau_1 = (C_a+C_x)/K_1$. However, if the thermal contact between sample and platform is not very good, i.e., the condition $K_2 \gg K_1$ is not satisfied then the temperature decay equation takes the form:

$$T(t) = T_0 + A^{(-t/\tau_1)} + B^{(-t/\tau_2)} \tag{2.2}$$

Here two time constants are given by: $\tau_1 = C_a/K_1$ and $\tau_2 = C_x/K_2$. This is called the two-tau method. QD PPMS software fits the above equation using the procedure given by [197]. Applicability of the method can be judged by a coupling parameter defined (and reported at each measurement) by $100\times K_2/(K_1+K_2)$. Sample Coupling should be close to 100 for a good measurement. Figure 2.18 shows the specific heat data for two compositions: $Ba(Fe_{0.975}Co_{0.025})_2As_2$ and $Ba(Fe_{0.925}Co_{0.075})_2As_2$. These samples are named SN163 (2.25% Co) and BFBS11D (7.5% Co). Underdoped sample (2.25% Co) does not show superconductivity (left panel of Fgure 2.18), which is

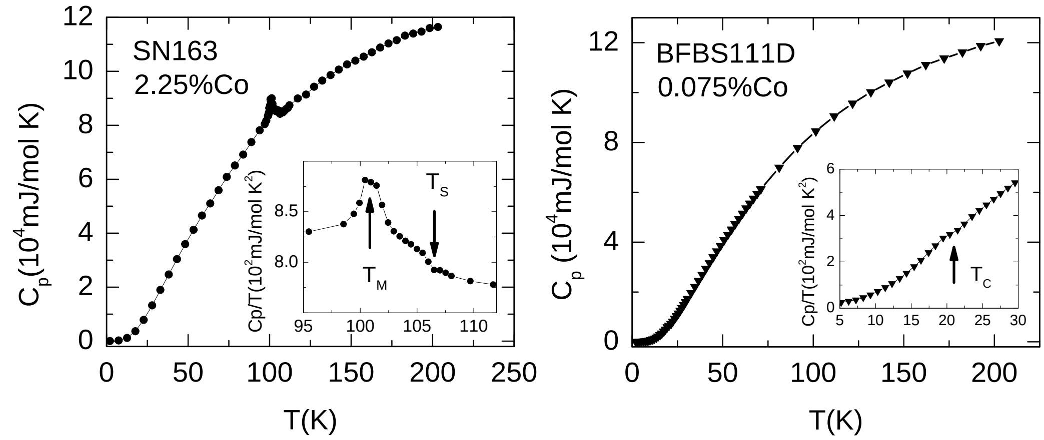

Figure 2.18: Left panel shows the specific heat for the underdoped non-superconducting sample. The inset depicts the magnetic and structural anomalies. In the right panel, specific heat for the optimally doped sample is shown. The Inset highlights the superconducting anomaly.

known to appear at around 3% in this series [18, 19]. The inset shows the C_p/T as a function of temperature. Two distinct anomalies associated with the magnetic (T_M) and structural (T_S) transitions can be identified, just like what was seen in the resistivity and magnetization measurements of underdoped specimens in previous sections. T_S and T_M are ≈106 K and ≈101 K respectively. The right panel of Figure 2.18 depicts C_p as a function of temperature for the sample BFBS110D. This sample does not show any signatures of magnetic/structural transitions, which is expected at this doping level [198, 188, 199]. The superconducting anomaly at ≈ 20.5 K can be observed in the inset where C_p/T is plotted as a function of temperature. It should be noted that the anomalies associated with the superconducting transition are rather feeble in this series of iron pnictides [198, 200].

2.11 Conclusions

In this chapter, we have described several experimental techniques used in this thesis to grow, characterize, and study 122 family of FeSCs in single-crystalline form. All examples were focused on the $Ba(Fe_{1-x}Co_x)_2As_2$ series. The high quality of the grown crystals is apparent in transport, EDX, Laue, magnetic and thermodynamic measurements. We have emphasized upon points which we think are useful for reproducibility. The steps involved in the single crystal growth experiments are explained in detail.

Chapter 3

Magnetotransport studies of $Sr(Fe_{1-x}Co_x)_2As_2$

In this chapter, we report on the extensive magnetotransport studies of the $Sr(Fe_{1-x}Co_x)_2As_2$ series. Three compositions that correspond to three distinct regions in the phase diagram of these materials are studied, i.e., the parent compound, an underdoped composition (x = 0.06) and an optimally doped composition (x = 0.12). We carried out the scaling analysis of the magnetotransport in this series, which is surprisingly non-existent to date. Based on the scaling analysis of the magnetotransport, we have tried to put these systems in perspective with high-T_C cuprates and some heavy fermions.

3.1 Introduction

$Sr(Fe_{1-x}Co_x)_2As_2$ is one the most studied families of iron-based superconductors, primarily due to the availability of relatively large single crystals; however, magnetotransport studies, particularly the scaling analysis of the magnetotransport is still lacking. Although large single crystals of these systems have been grown by a number of groups; to date, no study either on the parent compound or its electron-doped variants has reported the scaling of magnetotransport in these systems. This series (like many other FeSCs) display many non-Fermi liquid like properties, including, a quasi-linear resistivity, and a temperature dependent Hall coefficient among others [201, 202, 84, 203]. The $Sr(Fe_{1-x}Co_x)_2As_2$ system has some unique properties unlike some of the other 122 members. For instance, the magnetic and structural transitions remain concomitant and do not split even upon doping or after the application of pressure [204, 192, 205], which is in contrast to its close cousins $Ba(Fe_{1-x}Co_x)_2As_2$ and $Eu(Fe_{1-x}Co_x)_2As_2$ [188, 189, 41, 206, 207].

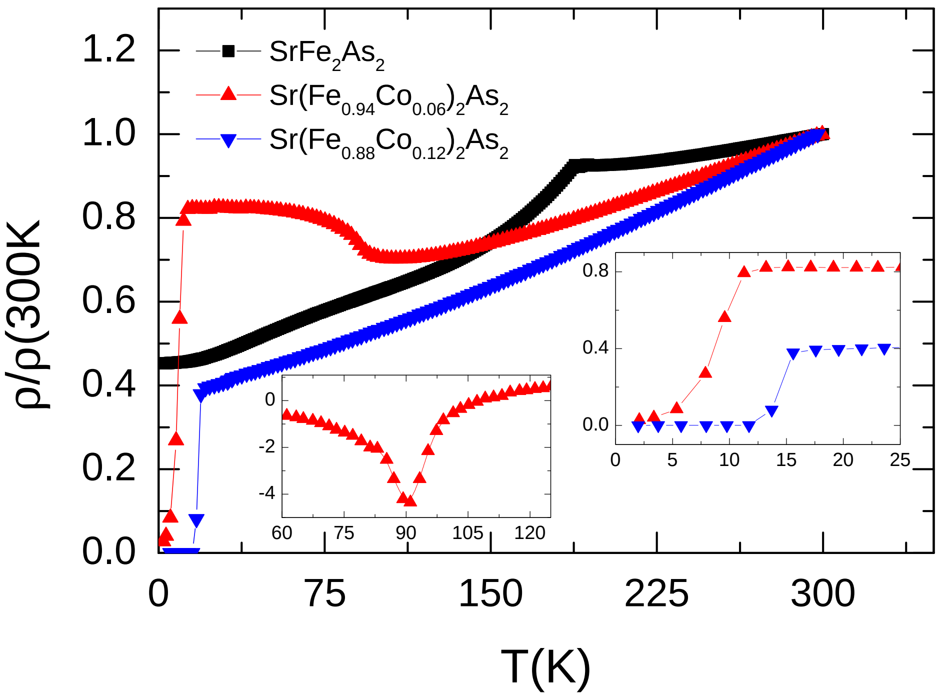

Figure 3.1: Main panel depicts the normalized (ρ/ρ_{300K}) zero field in plane resistivity for Sr(Fe$_{1-x}$Co$_x$)$_2$As$_2$ (x = 0, 0.06 and 0.12) from 2-300 K. Upper inset shows the resistivity near superconducting transition. Onset of superconducting transition for the x = 0.12 and 0.06 is observed at 16 K and 11 K respectively. The lower inset depicts the first temperature derivative of normalized resistivity for the underdoped composition x = 0.06. Magnetostructural transition occurs at $\sim$ 91 K.

On the contrary, the electron doped $Sr(Fe_{1-x}Ni_x)_2As_2$ system (similar to $Ba(Fe_{1-x}Ni_x)_2As_2$ system [191]) does show the separation of magnetic and structural transitions [42, 208]. This is surprising, since the Co and Ni both dope electrons, and are nearest neighbors in the periodic table. Although, it is not clear why does the magnetic and structural transitions separate after doping, it has been suggested that Ni doping at Fe site reduces the c axis exchange coupling in $Ba(Fe_{1-x}Ni_x)_2As_2$ system, which induces the quasi-2D spin fluctuations in the system [42]. Consequently, it was suggested that transition from 3D spin waves to quasi-2D spin excitations are important for the separation of magnetic and structural transitions [42]. Interestingly, isovalent substitution at Fe site (e.g., replacing Fe with Ru), also does not lead to the separation of magnetic and structural transitions [67, 209]. This is in contrast to the isovalent substitution at As site (e.g., replacing As with P), where the separation of magnetic/structural transition is observed [84, 68, 210, 211]. Hole-doped systems (e.g., $Ba_{1-x}K_xFe_2As_2$) also do not show any separation of magnetic/structural transition [212, 213]. Any theory attempting to explain these behaviors should coherently explain as to why the magnetic/structural transitions get separated after doping in some of the FeSCs while remain concomitant in others.

We report the magnetotransport measurements in electron-doped $Sr(Fe_{1-x}Co_x)_2As_2$ (x = 0, 0.06 and 0.12) with emphasis on its scaling analysis. Magnetotransport scaling techniques have been extensively used in high-Tc cuprates and heavy fermion systems. The Kohler and Modified Kohler's rule are some of the most widely used scaling methods of the magnetotransport. As mentioned in chapter one, the Kohler's rule states that the orbital magnetoresistance of a system can be expressed as a function of $H/\rho_{xx}(0)$, i.e., $[\rho_{xx}(H) - \rho_{xx}(0)]/\rho_{xx}(0) = F(H/\rho_{xx}(0))$, where $\rho_{xx}(H)$ is the resistivity at magnetic field H, $\rho_{xx}(0)$ is the zero-field resistivity and H is the applied magnetic field [61, 63, 62]. However, Kohler's rule is only valid when certain preconditions are fulfilled [64]. For example, there should be only one species of charge carriers that dominate the transport, relaxation rate should not vary for different points on the Fermi surface, etc. Kohler's rule is valid for a number of conventional metals and even some region of the phase diagram of high-Tc cuprates [8], heavy fermions [66], and iron-based superconductors [67]. To account for the anomalous transport properties of high Tc cuprates (including the violation of Kohler's rule in the strange metal phase of cuprates), the existence of two different relaxation rates was proposed. This led to the reformulation of Kohler's rule in terms of Hall angle i.e., $[\rho_{xx}(H) - \rho_{xx}(0)]/\rho_{xx}(0) = F(\tan\theta_H)$ [65]. This is referred to as the modified Kohler's rule. This modified Kohler's rule has been found to be valid in a number of high-Tc cuprates, FeSCs and heavy fermions systems

[51, 66, 72, 75, 84, 67, 214, 129]. We observed that both the Kohler and the modified Kohler's scaling are violated for the parent (x = 0) and optimally doped system (x = 0.12). Interestingly, the Hall angle displays quadratic temperature dependence in the optimally doped composition. Also, for the first time, we observed a linear magnetoresistance in the optimally doped system (x = 0.12). Unfortunately, despite several trials in a number of underdoped samples (x = 0.06), we were unable to get any measurable signal for the magnetoresistance in this system, even in the magnetic regime. We suspect that extremely low magnetoresistance may be an intrinsic behavior of the underdoped composition of $Sr(Fe_{1-x}Co_x)_2As_2$, which is probably the reason that despite the tremendous amount of work that has been done in this system using other techniques, no study reported its magnetoresistance so far.

3.2 Results and discussion

Transport properties of all three compositions of $Sr(Fe_{1-x}Co_x)_2As_2$ studied in this chapter are summarized in Figure 3.1. Additional details about the characterization and single crystal growth can be found in our work [215]. The parent compound ($SrFe_2As_2$) undergoes a combined magnetic/structural transition around $\sim$ 190 K, which is evidenced by a sharp drop in the resistivity. The magnetostructural transition is suppressed to $\sim$ 91 K by electron (Cobalt) doping, and superconductivity is observed at $\sim$ 11 K for this underdoped composition (x = 0.06). At optimal doping, the magnetostructural transition is completely suppressed and superconductivity is observed at $\sim$ 16 K. These observations are consistent with literature [215, 192, 205]. We would like to point out that the superconducting members of the $Sr(Fe_{1-x}Co_x)_2As_2$ series studied in this chapter display bulk superconductivity, where $\sim$ 100 % superconducting volume fractions are observed, for details, see our work [215].

3.2.1 Parent compound $SrFe_2As_2$

Magnetoresistance (MR) for the parent compound is shown in Figure 3.2(a). At low temperatures, within the magnetic state (below $\sim$ 190 K), a linear magnetoresistance is observed. However, MR is non-linear at low fields, and this non-linearity shifts to higher fields for higher temperatures within the magnetic state. As the temperature is increased, the MR decreases rapidly and vanishes near the magnetostructural transition and is negligible in the paramagnetic regime (see Figure 3.2(b)). This linear magnetoresistance in

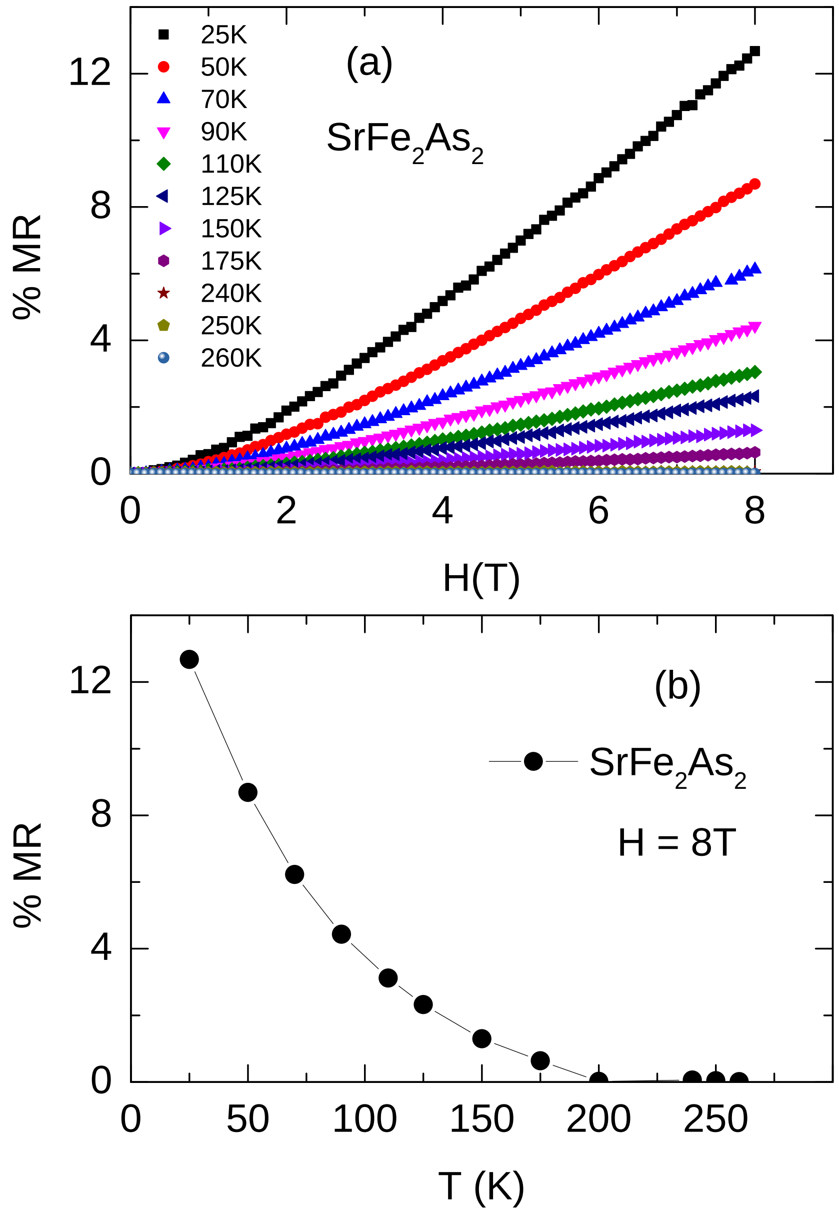

Figure 3.2: In (a), the magnetoresistance as a function the applied magnetic field is shown. In (b) the magnetoresistance at 8 T magnetic field is shown as a function of the temperature.

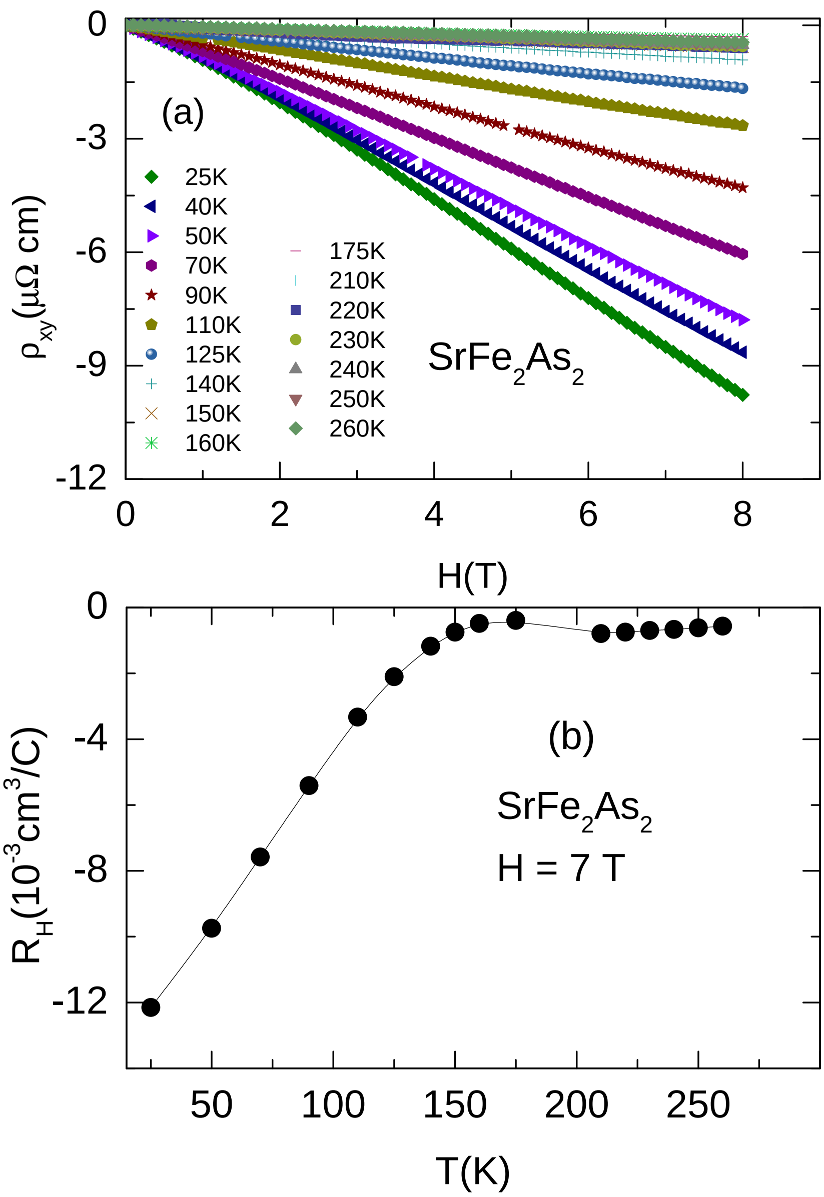

Figure 3.3: The Hall resistivity for the parent compound encompassing the magnetic as well as the paramagnetic region is shown in (a). In (b), the Hall coefficient ($R_H = \rho_{xy}/H$) calculated at 7 T magnetic is shown.

the magnetic state is well reported [125, 127, 128, 24, 130, 131, 132, 133, 134, 69, 135, 136] and is often reported to arise as a consequence of Dirac cone states [133, 113, 126, 128]. Dirac states have been observed in the magnetic regime of several FeSCs families [140, 137, 138, 139, 141, 143, 145, 146]. In Figure 3.3(a), the Hall resistivity ρ_{xy} for the parent compound is shown from 25-260 K, which spans the magnetic as well as the paramagnetic regime. The Hall resistivity is non-linear at low fields for temperatures within the magnetically ordered state, however, this non-linearity is absent in the paramagnetic regime similar to many other FeSCs [130, 126]. Microscopic origin of this nonlinear ρ_{xy} remains unclear, however the multiband character of FeSCs has been suggested as a possible reason for this non-linearity [130]. It was also suggested that this non-linear Hall resistivity might also arise as a consequence of Dirac states, which is also supported by a rapid decrease in non-linearity in Hall resistivity and reduced linear MR in doped compositions [126]. Figure 3.3(b), the Hall coefficient ($R_H = \rho_{xy}/H$) calculated using 7 T magnetic field is shown. Hall coefficient remains almost constant in the paramagnetic regime, however, its magnitude increases rapidly below the magnetostructural transition. This increase in $|R_H|$ is consistent with a spin density wave reconstructed (partially gapped) Fermi surface [144, 139, 216].

In Figure 3.4, we present the scaling of magnetoresistance for $SrFe_2As_2$. Figure 3.4(a) and (b) depicts the Kohler and modified Kohler's plots respectively. Evidently, the magnetoresistance isotherms do not collapse on to a single curve (in both (a) and (b)), indicating that both scalings are violated in the temperature range shown (25-260 K). Since the reconstruction of the Fermi-surface at the magnetic transition is reported to produce high mobility Dirac carriers [141] (in addition to already existing normal carriers), this coexistence of two (at least [130]) different type of carriers can be a possible reason for the violation of Kohler's rule. Another possible reason for the violation of Kohler's rule can be the temperature dependence of carrier concentration. Strongly temperature dependent Hall coefficient (as can be seen in Figure 3.3(b)) would support such a scenario. Indeed, the temperature variation of carrier concentration in some FeSCs has been inferred from photoemission experiments [217]. In order to explain the violation of Kohler's rule in cuprates, the existence of two relaxation rates was proposed, where transport relaxation rate τ_{tr}^{-1} governs the resistivity and the magnetoresistance and Hall angle are governed by the so-called Hall scattering rate τ_H^{-1} [76, 65, 77]. Since the modified Kohler's scaling is invalid for the parent compound (see Figure 3.4(b)), this scenario does not seem to be applicable here.

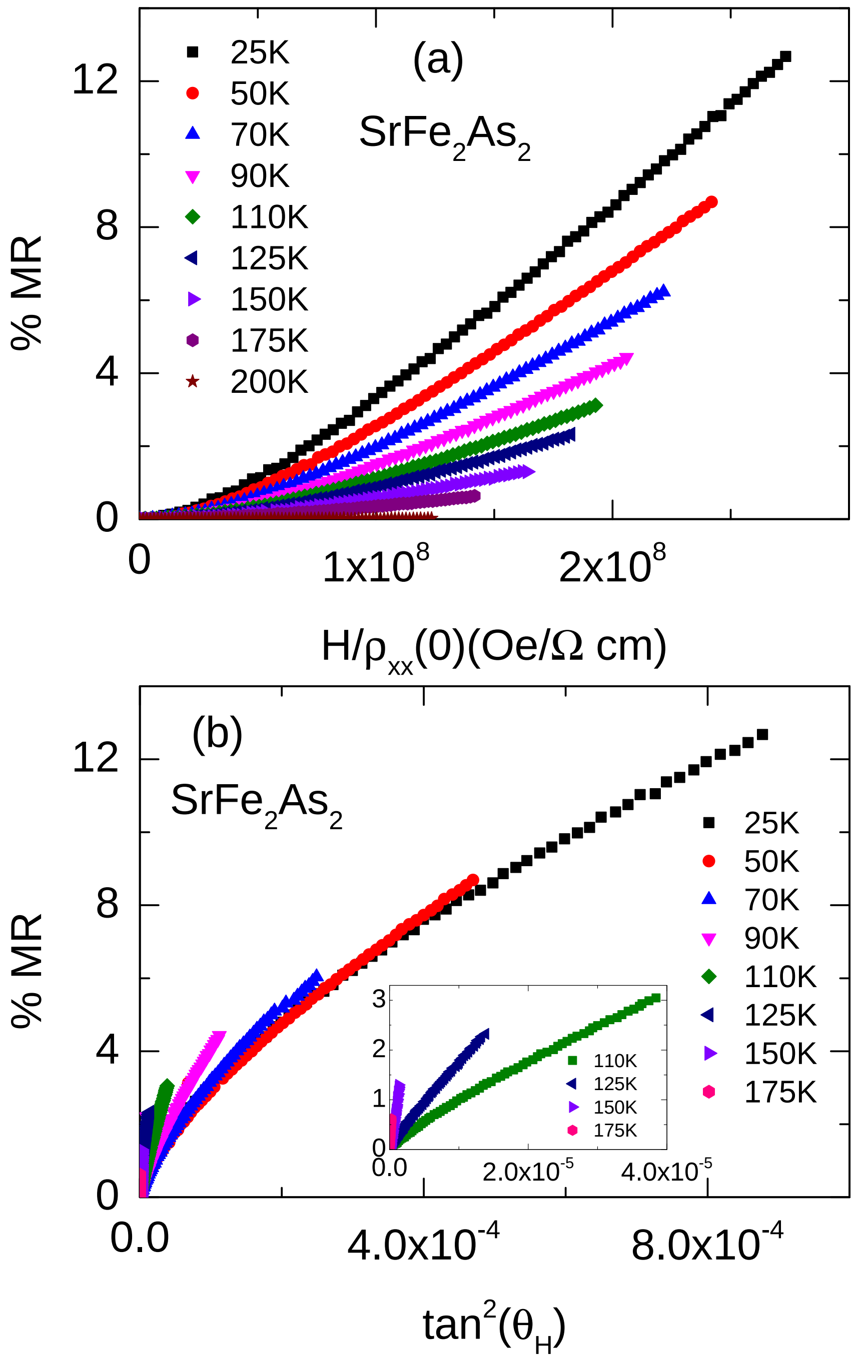

Figure 3.4: The Kohler's scaling of magnetoresistance is depicted in (a). In (b), the modified Kohler's scaling is shown. In the inset of (b), expanded view of the some (110 K, 125 K, 150 K, and 175 K) high-temperature data points is presented for clarity.

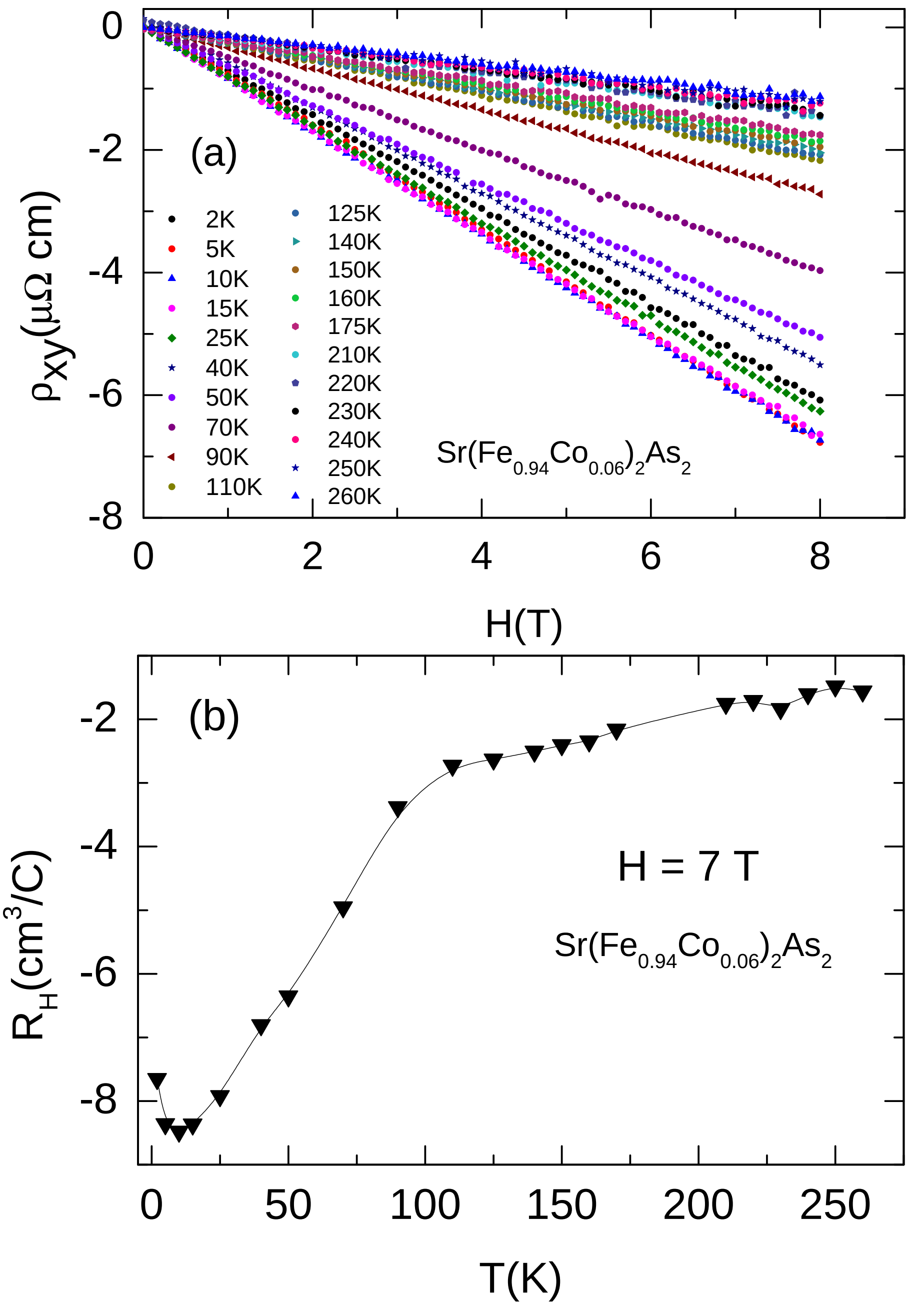

Figure 3.5: Hall resistivity as a function of the applied magnetic field is shown in (a). In (b), the Hall coefficient calculated using 7 T magnetic field shown.

3.2.2 Underdoped composition ($x = 0.06$)

A comprehensive data set for the Hall resistivity spanning the superconducting, magnetic and paramagnetic region for the underdoped (6%Co) composition is shown in Figure 3.5(a). ρ_{xy} is nearly linear in the entire temperature range shown in Figure 3.5(a). This is in contrast to the magnetic state of the parent compound (see Figure 3.3(a)) where the non-linear Hall resistivity is observed at low temperatures and magnetic fields. Figure 3.5(b) depicts the Hall coefficient from 2-260 K. Similar to the parent compound, a sharp increase in the magnitude of the Hall coefficient is observed at the onset of magnetostructural transition at $\sim$ 91 K. The low-temperature upturn (Figure 3.5(b)) around 11 K correspond to the onset of superconductivity. Also, the magnitude of the Hall coefficient at low temperatures is considerably smaller than the parent compound (see Figure 3.3(b)), which is consistent with the fact that doping electrons will lead to the reduction in the Hall coefficient. Reduction in the Hall coefficient after doping does not support some of the previous theoretical proposals where it was suggested that the transition metals doped at the iron site do not dope carriers but rather their charge remains localized at the dopant site [218]. Interestingly, the Hall coefficient in the paramagnetic region has now acquired a temperature dependence which is stronger than what is observed in the paramagnetic regime of the parent compound (see Figure 3.3(b)) indicating pronounced non-Fermi liquid behavior in this system.

3.2.3 The optimally doped system ($x = 0.12$)

The Hall resistivity for the $Sr(Fe_{0.88}Co_{0.12})_2As_2$ system is shown in Figure 3.6(a). ρ_{xy} is linear in magnetic field in the entire temperature range presented in Figure 3.6(a). In the Figure 3.6(b), the Hall coefficient at a 7 T magnetic field is shown. Interestingly, R_H is constant up to 40 K, after which it acquires a strong temperature dependence. Interestingly, temperature dependence of R_H is stronger than what was observed in the paramagnetic regime of the $SrFe_2As_2$ (Figure 3.3(b)) and underdoped composition (Figure 3.5(b)). This suggests that non-Fermi liquid behavior is more pronounced in the optimally doped composition. In this context, it should be noted that it is this region of the phase diagram of other strongly correlated electron systems, like high-T_C cuprates, heavy fermions and many other iron-based superconductors, where the most pronounced non-Fermi liquid behaviors are observed.

In Figure 3.7, we present the scaling of the magnetotransport for the optimally doped $Sr(Fe_{0.88}Co_{0.12})_2As_2$ system. In (a), the Kohler's scaling is

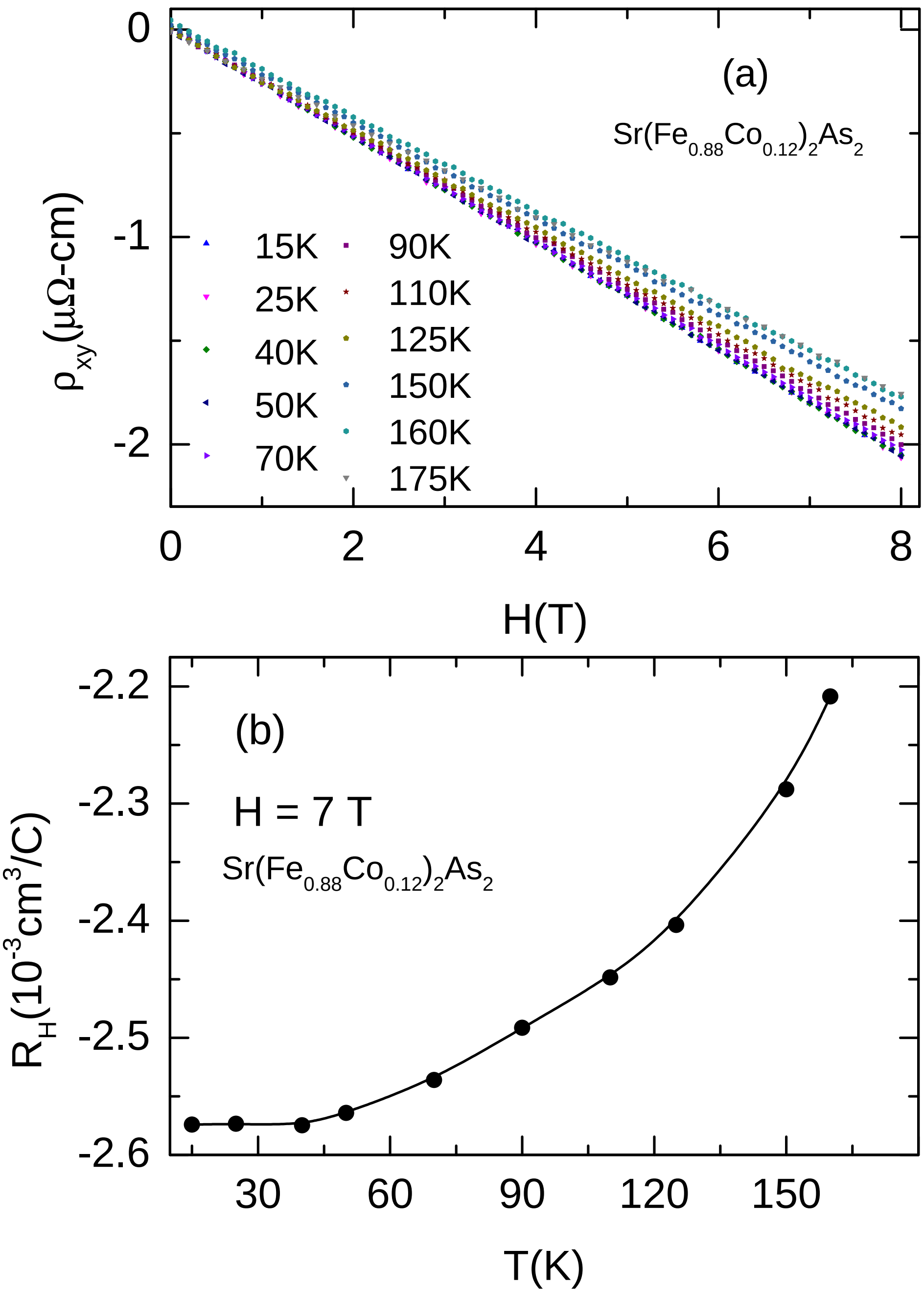

Figure 3.6: The Hall resistivity for the $Sr(Fe_{0.88}Co_{0.12})_2As_2$ system is shown in Figure (a). In (b), the Hall coefficient calculated at 7 T magnetic field is shown.

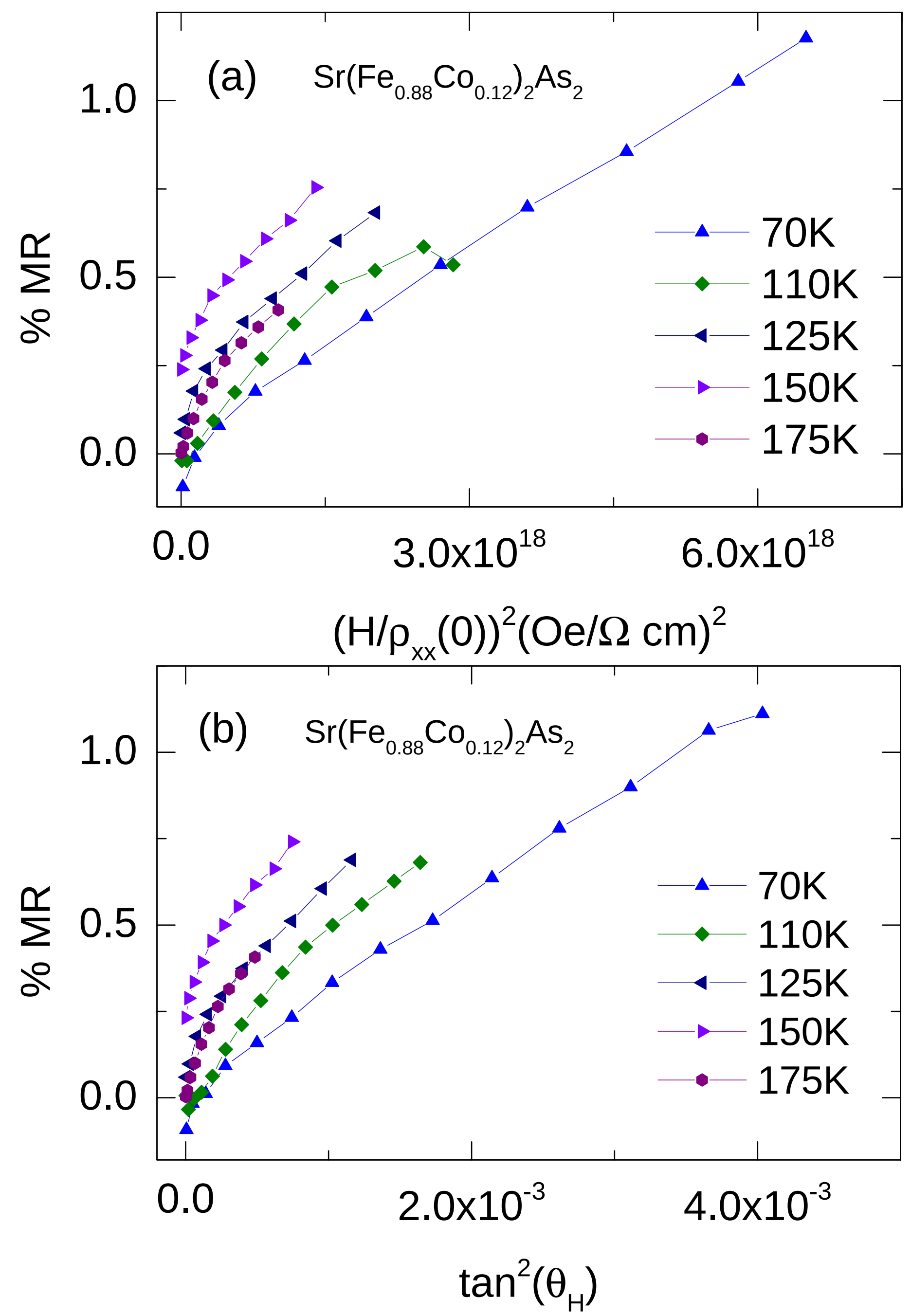

Figure 3.7: The Kohler and modified Kohler's scaling for $Sr(Fe_{0.88}Co_{0.12})_2As_2$ are shown in (a) and (b) respectively.

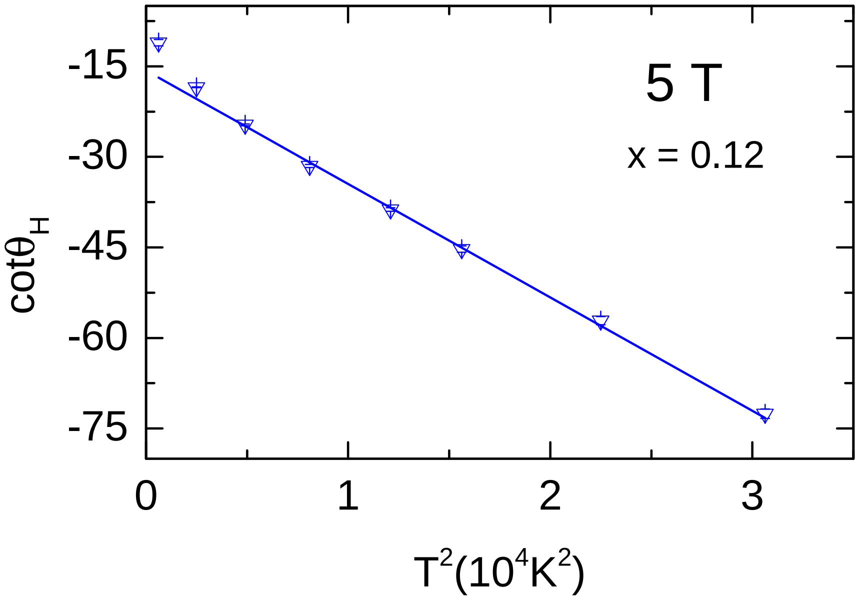

Figure 3.8: $\cot\theta_H$ determined using 5 T magnetic field is plotted as a function of T^2 for $Sr(Fe_{0.88}Co_{0.12})_2As_2$. The straight line is a linear fit to the data.

shown, where the magnetoresistance plots at different temperatures do not collapse onto a single curve, indicating its violation similar to the parent compound (Figure 3.4(a)). Out of a number of factors that could result in the violation of the Kohler's rule, like the variation of carrier concentration with temperature, multiple carriers contributing to the transport, anisotropic reconstruction of the Fermi surface, etc., it is difficult to pinpoint the exact mechanism for its violation. A number of these aforementioned factors (that can lead to the violation of Kohler's rule) add to the complexity of the problem.

Interestingly, the modified Kohler's scaling is also violated as can be seen in Figure 3.7(b). The modified Kohler's rule is based on the idea that the magnetoresistance and Hall angle are governed by the Hall scattering rate τ_H^{-1}, not the transport relaxation rate τ_{tr}^{-1} that appears in the Kohler's rule. Numerous theoretical approaches were put forth to explain the validity of modified Kohler's rule and separation of relaxation rates in high-Tc cuprates and several heavy fermion systems. In one approach, the separation of relaxation rates arises as a consequence of the anisotropic reconstruction of the Fermi surface in terms of the so-called 'hot' and 'cold' regions on the Fermi surface [53, 219, 94, 220, 52, 92, 221]. Charge carriers scatter rather strongly on the 'hot' spots (due to the scattering from antiferromagnetic

(AF) spin fluctuations), which determine the resistivity. On the other hand, the 'cold' regions determine the Hall resistivity ($\rho_{xy} \sim \tau_{cold}^2$). The existence of the 'hot' and 'cold' regions in FeSCs has been invoked in theoretical as well as in experimental studies [55, 67, 56, 222, 57, 223, 224]. In another approach, Hiroshi Kontani and co-workers have derived many non-Fermi liquid behaviors (including the modified Kohler's rule) on a model based on the Fermi liquid ground state. They argue that if the current vertex corrections (which are ignored in the relaxation time approximation) in the presence of antiferromagnetic (AF) spin fluctuations are taken into account, then most anomalous transport properties can be derived without assuming a non-Fermi liquid ground state in strongly correlated electron systems like high-Tc cuprates [97]. Vertex correction refers to the induced current by quasiparticle excitations in a Fermi liquid. In this approach, transport coefficients are renormalized due to the temperature dependence of AF spin fluctuation correlation length, e.g., $R_H \sim \xi_{AF}^2$ [98, 225]. In Kontani's approach, violation of the Kohler's rule and validity of modified Kohler's rule is a natural consequence of the temperature dependence of AF spin fluctuation correlation length.

The complexity associated with the microscopic origin of the violation of the modified Kohler's rule is further increased by the Hall angle measurements. In Figure 3.8, $\cot(\theta_H)$ as a function of the temperature is shown. $\cot(\theta_H)$ display a quadratic temperature dependence. Deviation from the T^2 behaviors is observed below 40 K, which we suspect arises due to the superconducting fluctuations. It should be noted that the quadratic temperature dependence of $\cot(\theta_H)$ along with a non-quadratic temperature dependence of resistivity (see Figure 3.1) suggests a separation of relaxation rates. Also, since magnetoresistance and $\cot(\theta_H)$ are governed by the same scattering time τ_H in the relaxation rate separation picture, modified Kohler's scaling should have been valid (which is not the case, see Figure 3.7(b)). Violation of modified Kohler's rule in the presence of T^2 dependent Hall angle suggests that these two quantities are not governed by the same scattering mechanism. We would like to point out that similar observations where modified Kohler's rule was violated in the presence of T^2 dependent Hall angle were reported early on in high-T_C cuprates [226, 227, 228, 229], and it was suggested that the modified Kohler's rule may not be universally applicable to all high-T_C cuprates [226, 227, 229]. These observations, however, did not attract much attention. Our observations suggest, for the first time that the modified Kohler's rule may not be universally applicable to iron-based superconductors as well.

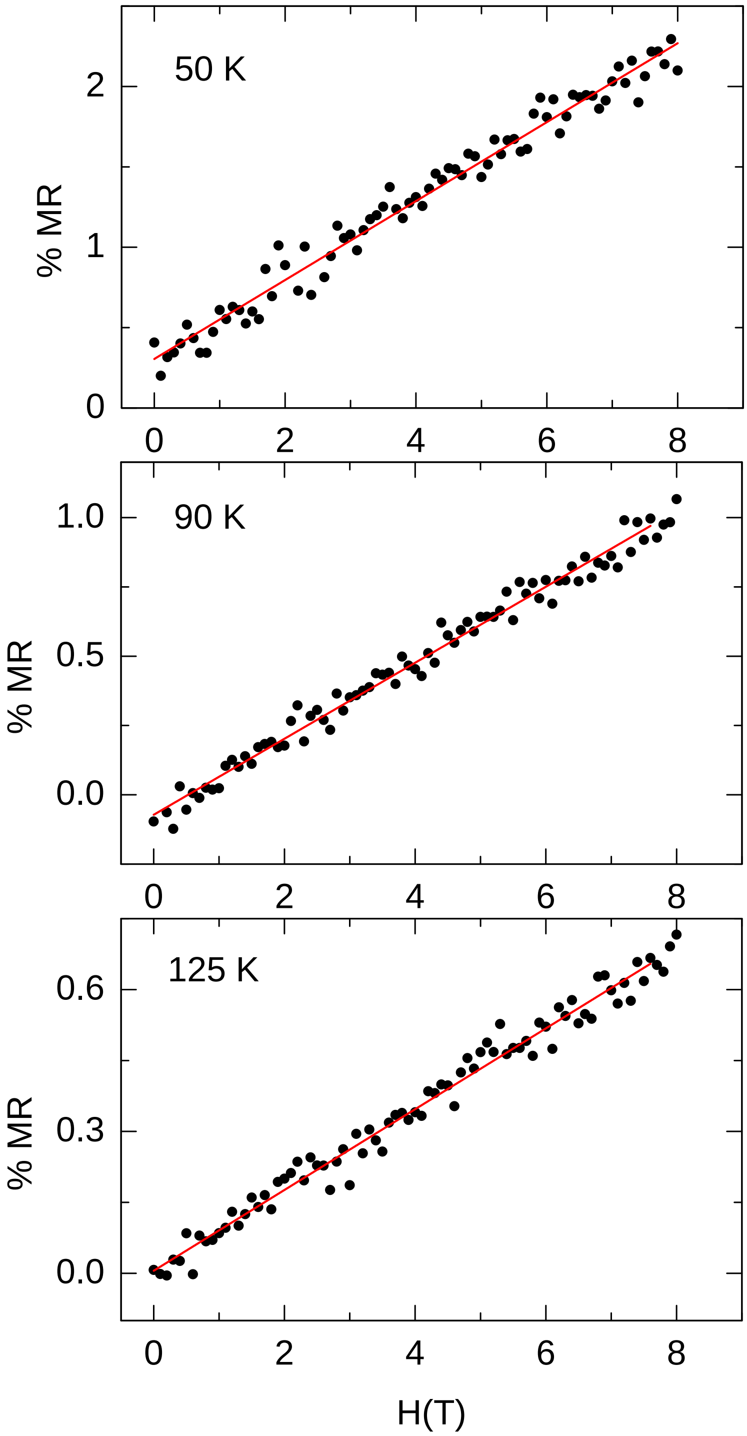

Figure 3.9: Magnetoresistance as a function of the applied magnetic field at three representative temperatures is shown.

Linear magnetoresistance

A striking observation is that of a positive linear magnetoresistance (LMR) in the optimally doped $Sr(Fe_{0.88}Co_{0.12})_2As_2$ system; see Figure 3.9. LMR is reported in the antiferromagnetic state of several FeSCs [125, 127, 128, 24, 130, 131, 132, 133, 134, 69, 135, 136], where it is attributed to the presence of linearly dispersing (E $\sim$ K) Dirac cone states, which is often interpreted using the quantum linear magnetoresistance model of the Abrikosov [157, 158, 159]. In Abrikosov's model, LMR is predicted in the 'quantum limit' when all carriers occupy the lowest Landau band [157]. Quantum limit conditions are: n $\ll (eH/c\hbar)^{3/2}$ and T $\ll eH\hbar/m^*$, here, H is the applied magnetic field, n is carrier density, m^* is the effective electron mass. Since Dirac pockets in the SDW state are reported to be small and have very low carrier concentration [142], QLM conditions can be fulfilled even at the typical laboratory magnetic fields ($\sim$ 9 T) under which linear magnetoresistance is often reported. However, as $Sr(Fe_{0.88}Co_{0.12})_2As_2$ does not show any long-range magnetic order, hence linear magnetoresistance, in this case, is even more intriguing since Dirac cone states are reported to be a feature of the magnetically ordered state. Interestingly, linear magnetoresistance in the paramagnetic phase of $Fe_{1+y}Te_{0.6}Se_{0.4}$ was also observed [69]. It should be noted that $Fe_{1+y}Te_{0.6}Se_{0.4}$ is an optimally doped system and does not have any long-range magnetic order [230]. Interestingly, violation of the Kohler as well as modified Kohler's scaling for $Fe_{1+y}Te_{0.6}Se_{0.4}$ was also reported in this study [69], indicating striking similarity between $Fe_{1+y}Te_{0.6}Se_{0.4}$ and $Sr(Fe_{0.88}Co_{0.12})_2As_2$.

It is evident that the phenomenological approaches where the linear magnetoresistance arises from the Dirac states do not seem to be valid for the $Sr(Fe_{0.88}Co_{0.12})_2As_2$, since Dirac states are unlikely to be present in the absence of any long-range magnetic order. In a recent theoretical work, a linear magnetoresistance due to scattering from the hot-spots was predicted in the paramagnetic regime of the iron-based superconductors [222]. In this work, the conventional magnetotransport (e.g., MR $\sim H^2$) is limited to low magnetic fields, and a linear magnetoresistance is predicted at higher fields. This linear magnetoresistance arises as a consequence of the linear growth of the Fermi surface area affected by the scattering from hot spots after the application of a magnetic field. This model, however, also predict the Hall conductivity to be quadratic in the same magnetic field range in which a linear MR is predicted, which is contradictory to what is seen in optimally doped $Sr(Fe_{0.88}Co_{0.12})_2As_2$ (see Figure 3.6(a)) and other FeSCs [201], where Hall resistivity shows a nearly linear in magnetic field dependence. In conclusion, a satisfactory theory of the normal state magnetotransport for the multiband iron-based superconductors is lacking, which may be partly due to the fact that there have not been many experimental studies in this regime which are needed to elucidate the nature of FeSCs in this regime.

3.3 Conclusions

In conclusion, we report detailed magnetotransport studies of three representative compositions of $Sr(Fe_{1-x}Co_x)_2As_2$ series. We observed that both the Kohler and modified Kohler's scaling are violated for the parent and optimally electron-doped system. Violation of modified Kohler's rule and quadratic temperature dependence of the Hall angle suggests that the modified Kohler's rule may not be universally applicable to all iron-based superconductors. Interestingly, we observed for the first time, a linear magnetoresistance in the $Sr(Fe_{0.88}Co_{0.12})_2As_2$ system, which does not harbor a magnetic ground state.

Chapter 4

Magnetotransport in $Ba(Fe_{1-x}Co_x)_2As_2$ series

Besides the high-T_C cuprates, iron-based superconductors are the only known high-T_C superconducting materials class. These fascinating materials have several striking similarities and differences with other, more extensively studied strongly correlated electron materials like heavy fermions and high-T_C cuprates. For instance, a single band (Cu $d_{x^2-y^2}$ band) description is adequate to describe the normal state transport properties of high-T_C cuprates, whereas for the FeSCs a multiband model is essential to describe the physics since all five Fe 3d bands cross the Fermi level [231]. Also, as opposed to the parent compounds of cuprates, where strong onsite coulomb repulsion (U) leads to an antiferromagnetic Mott insulating state, parent compounds of FeSCs are more itinerant like (somewhat similar to the heavy fermions) having a spin density wave ground state [2, 18]. Similar to cuprates and heavy fermion systems, transport properties of FeSCs show pronounced non-Fermi liquid behaviors, including, quasi-linear resistivity [144], and strongly temperature dependent Hall coefficient, etc. Despite apparent differences in the physical properties of their parent compounds (like the itinerant nature of heavy fermions and FeSCs in contrast to Mott insulating state of cuprates), a number of similarities have been pointed out, especially in their magnetotransport behavior. Also, FeSCs are layered materials, where the FeAs layers dominate the physical properties, similar to high-T_C cuprates, where the physical properties, to a large extent, are determined by the CuO_2 layers.

It has been suggested that the spin fluctuations play a key role in the physics of high-T_C cuprates and heavy fermions, and might even be responsible for the unconventional behaviors seen in their phase diagram. Interestingly, spin fluctuations have also been proposed to be a key factor for the physics of iron-based superconductors including their role in mediating the superconducting pairing interaction among electrons [232, 36]. Based on the scaling techniques of the magnetotransport, it has been shown that the magnetotransport behaviors of high-T_C cuprates and heavy fermions bear striking similarities, which are thought to be governed by spin fluctuations [225, 66, 72, 74]. Along the similar lines, we have taken up the scaling approach towards the magnetotransport in the iron-based superconductors. As is the case in other areas of physics and condensed matter, scaling relationships are a powerful tool to identify similarities among various materials classes. For instance, a large number of materials can be divided into different universality classes based on the values of their critical exponents. One of the most widely used scaling methods of the magnetotransport in simple metals is the Kohler's rule [64, 61, 62, 63]. It states that the magnetoresistance of a system can be expressed as a function of H/ρ_0, i.e., $[\rho(H) - \rho(0)]/\rho(0) = F[H/\rho_0]$, where, H is the applied magnetic field, $\rho(H)$ is the resistivity at magnetic field H and $\rho(0)$ is zero field resistivity. The Kohler's rule has been shown to be valid in the Fermi liquid regime of cuprates [8], heavy fermions [66] and even in some FeSCs [67]. A new scaling technique of the magnetotransport for high-T_C cuprates was put forth by Harris et al., that worked well even in the strange metal phase of high-T_C cuprates, where the Kohlers scaling is violated [65]. They proposed that the magnetoresistance can be scaled not by H/ρ_0, but by Hall angle $\tan\theta_H$, i.e., $[\rho(H) - \rho(0)]/\rho(0) = F[tan\theta_H]$. Modified Kohlers rule is a natural consequence of the apparent lifetime separation of charge carriers in cuprates, where the resistivity is governed by the so-called transport relaxation rate (τ_{tr}^{-1}), and the magnetoresistance by the Hall scattering rate (τ_H^{-1}) [93, 53, 92, 221].

In this chapter, we have investigated three distinctly different compositions of $Ba(Fe_{1-x}Co_x)_2As_2$ (x = 0, 0.038, and 0.074, see Figure 4.1) series to investigate upon the validity of these scaling techniques. We observed that the Kohler's scaling is violated for the parent compound as well as the underdoped composition. On the other hand, the modified Kohler's scaling is violated for the parent compound but is well obeyed by the underdoped composition. Also, a pseudogap like feature is observed in the Hall angle measurements in the high-temperature paramagnetic region of the underdoped composition, supportive evidence for which has also been reported in similar compositions in the interplane transport [233] as well as NMR [111] studies. The validity of modified Kohler's scaling and the presence of the pseudogap phase in this particular composition ($x = 0.038$) indicates its relative similarity to high-T_C cuprates.

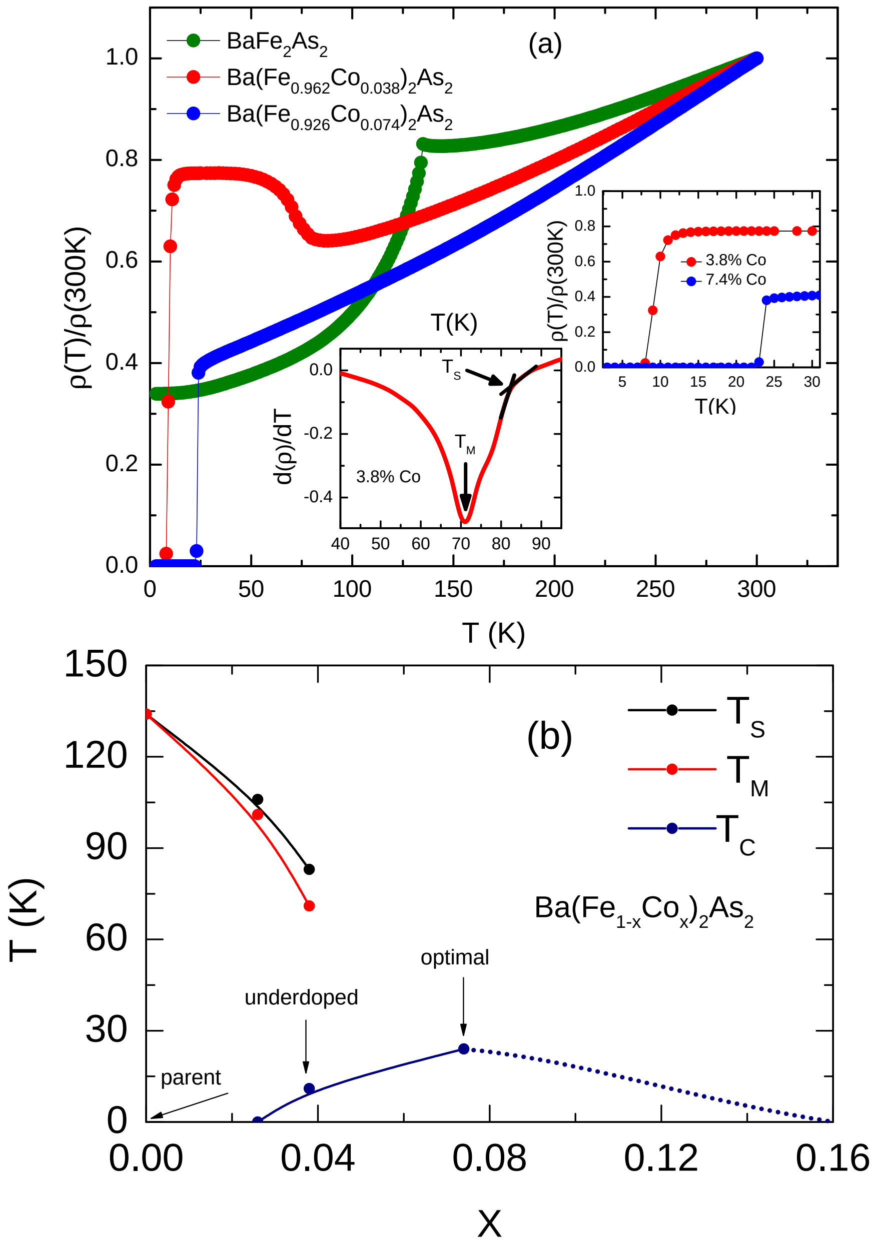

Figure 4.1: The normalized resistivity for three compositions of $Ba(Fe_{1-x}Co_x)_2As_2$ (x =, 0, 0.038, 0.074) series is shown in (a). The upper inset depicts the data near superconducting region for the $x = 0.038$ and $x = 0.074$. Lower inset depicts the temperature derivative of the normalized resistivity near the magnetic and structural transitions for the $x = 0.038$. In (b), T-x phase diagram derived from the transport measurements is shown. Arrows denote the compositions studied in this chapter. Dotted line represents the overdoped region not studied in this chapter. Labels T_S, T_M and T_C represent the structural, magnetic and superconducting transition temperatures respectively.

4.1 Results and discussion

Normalized resistivity for three compositions of $Ba(Fe_{1-x}Co_x)_2As_2$, i.e., the parent compound $BaFe_2As_2$, the underdoped composition $Ba(Fe_{0.962}Co_{0.038})_2$ -As_2 and the optimally doped composition $Ba(Fe_{0.926}Co_{0.074})_2As_2$ is shown in the main panel of Figure 4.1(a). The parent compound undergoes a combined magnetostructural transition at ~ 134 K, as indicated by the drop in the resistivity. By Co doping (x = 0.038), the magnetostructural transition gets suppressed and separated, i.e., two separate anomalies associated with the high temperature structural (T_S ~ 71 K) and low temperature magnetic transitions (T_M ~ 84 K) are now visible in the temperature derivative of normalized resistivity (lower inset of Figure 4.1(a)). Additionally, this underdoped composition undergoes a superconducting transition at ~ 11 K, as depicted in the upper inset of (a). The optimally doped composition x = 0.074 undergo a superconducting transition at ~ 24 K (upper inset of (a)) and do not show signatures of magnetic or structural transitions in the derivative (not shown), as expected at this doping level. In Figure 4.1(b), the phase diagram constructed for $Ba(Fe_{1-x}Co_x)_2As_2$ (x =, 0, 0.024, 0.038, 0.074) based on the transport measurements is shown. Arrows represent the compositions studied using the magnetotransport technique in this chapter. The dotted line in the dome-shaped region represents the region of phase diagram where the conventional behaviors are recovered gradually at higher doping levels (the compositions corresponding to the dotted region are not studied in this thesis). It should be noted that $Ba(Fe_{1-x}Co_x)_2As_2$ is a well-studied series, and magnetic, structural and superconducting transition temperatures depicted in Figure 4.1(a) matches well with the existing literature [188, 40, 47, 234]. Details about the magnetic characterization of $Ba(Fe_{1-x}Co_x)_2As_2$ can be found in Chapter 2, Section 2.9. Both the underdoped and the optimally doped compositions display bulk superconductivity where the superconducting volume fraction of ~100% is observed.

4.1.1 The parent compound: $BaFe_2As_2$

The magnetoresistance for the parent compound is shown in Figure 4.2(a). Magnetoresistance decreases rapidly as the temperature is increased and vanish near the magnetostructural transition (T ~ 134 K). The magnetoresistance is linear, and this linearity is pronounced at low temperatures and high magnetic fields, which coexist with a non-linear contribution at low magnetic fields. This linear magnetoresistance, which is also observed in the magnetically ordered state of many other FeSCs, is often reported to originate from the Dirac cone states [133, 113, 126, 128]. In Figure 4.2(b), the Hall resistivity from 5-250 K, covering the magnetic as well as the paramagnetic regime is shown.

ρ_{xy} is nonlinear at low fields within the magnetically ordered state, however, this non-linearity is pronounced at low temperatures. Hall resistivity is linear in the high-temperature paramagnetic phase and is weakly temperature dependent. Although the microscopic origin of this non-linear Hall resistivity in the magnetically ordered state of FeSCs is an unsettled issue, the presence of Dirac states has been proposed to be a possible reason for this [188]. This proposal is based on the observation that the non-linearity in Hall resistivity is suppressed just as the linear magnetoresistance is suppressed at higher temperatures within the magnetically ordered state, suggesting a common microscopic origin. In Figure 4.3, the Hall coefficient R_H as a function of the temperature is shown for the parent compound. As is evident, R_H remains almost constant in the paramagnetic regime, however, a sharp increase in $|R_H|$ is seen below the magnetostructural transition at $\sim$ 134 K. Magnitude of the Hall coefficient increases by a factor of $\sim$ 54 between 5 K and 250 K. The increase in the Hall coefficient below the magnetostructural transition occurs due to the partial gapping of the spin density wave reconstructed Fermi surface, which leads to the reduced carrier concentration [144, 139, 216].

In Figure 4.4, we present the scaling of magnetoresistance for the parent compound. Figure 4.4(a) depicts the Kohler's scaling, where the magnetoresistance is plotted as a function of $H/\rho_{xx}(0)$. Clearly, the magnetoresistance isotherms do not collapse on a single curve, indicating a violation of Kohler's scaling for $BaFe_2As_2$. As we have discussed in chapter one and three, the Kohler's scaling relies on a uniform scattering of a single species of charge carriers across the whole Fermi surface. Also, the temperature independent carrier concentration is a prerequisite for its validity [64]. Since, FeSCs are known to be multiband systems, where multiple bands cross the Fermi level and contribute to the charge transport, the violation of Kohler's rule is not surprising. Also, a strongly temperature dependent Hall coefficient (see Figure 4.3) suggests that the carrier concentration is changing with temperature, which is unfavorable for Kohler's scaling. Strong temperature dependence of charge carriers has also been reported in some angle-resolved photoemission experiments [217]. In Figure 4.4(b), the modified Kohler's scaling is shown, where magnetoresistance isotherms do not collapse on a single curve, indicating its violation. As discussed in chapter one and three, modified Kohler's rule relies on the anisotropic scattering on the Fermi surface, giving rise to two separate relaxation rates namely the Hall (τ_H^{-1}) and transport scattering (τ_{tr}^{-1}) rates which govern the magnetoresistance and resistivity respectively. Violation of modified Kohler's scaling suggests that this scenario is not valid

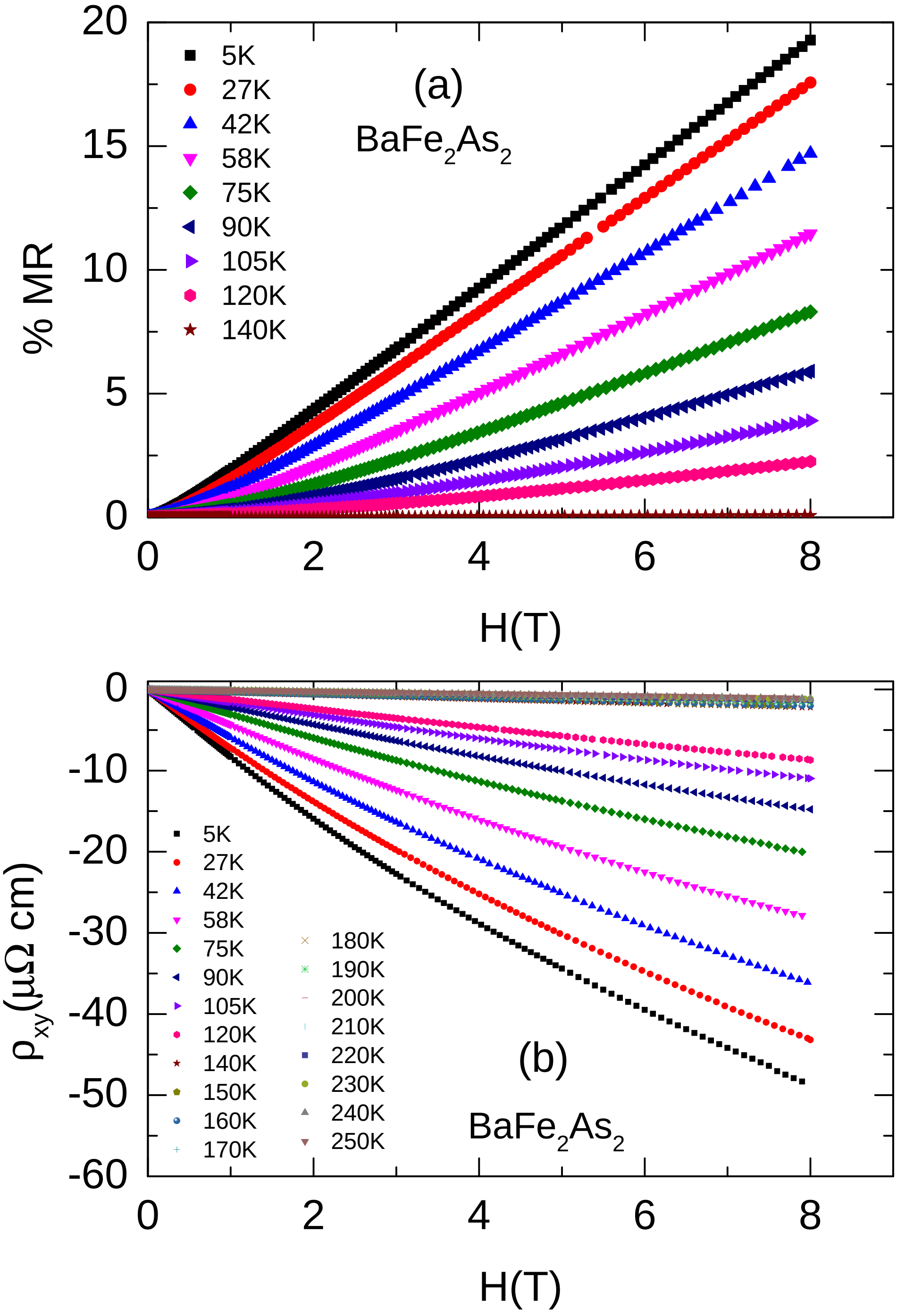

Figure 4.2: The magnetoresistance isotherms for the parent compound as a function of the magnetic field are shown in (a). In (b), the Hall resistivity as a function of the magnetic field is shown in an extended temperature range.

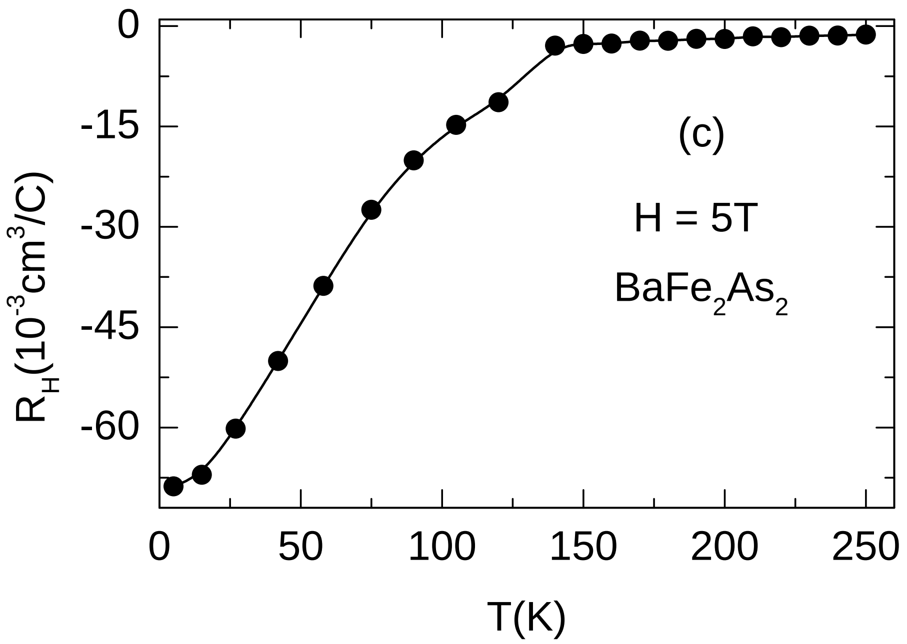

Figure 4.3: The Hall coefficient R_H calculated using a magnetic field of 5 T is shown for the parent compound $BaFe_2As_2$.

for $BaFe_2As_2$.

4.1.2 The underdoped composition $x = 0.038$

The magnetoresistance and Hall resistivity for the underdoped composition $Ba(Fe_{0.962}Co_{0.038})_2As_2$ are depicted in Figure 4.5(a) and (b) respectively. The magnetoresistance is substantially reduced by cobalt doping, i.e., MR is $\sim$ 5% at 19 K for this underdoped composition, whereas the MR is $\sim$ 20% at 5 K for the parent compound (see Figure 4.2(a)). The magnetoresistance is linear at high magnetic fields and low temperatures; however, the non-linear contribution which exists at low fields, increases to higher fields at higher temperatures. Similar to the parent compound, the Hall resistivity is non-linear in the magnetic state (below 71 K), however, this non-linearity is relatively weak. It is possible to understand the suppressed linear magnetoresistance and non-linearity in Hall resistivity in this underdoped composition if we examine the quantum limit conditions of Abrikosov's model [160]. As we mentioned earlier, the linear magnetoresistance in the magnetic state of FeSCs (and possibly the nonlinear Hall resistivity) is often thought to emerge from the Dirac cone states [188]. Its origin is often interpreted using the quantum linear magnetoresistance model of Abrikosov, where a linear mag-

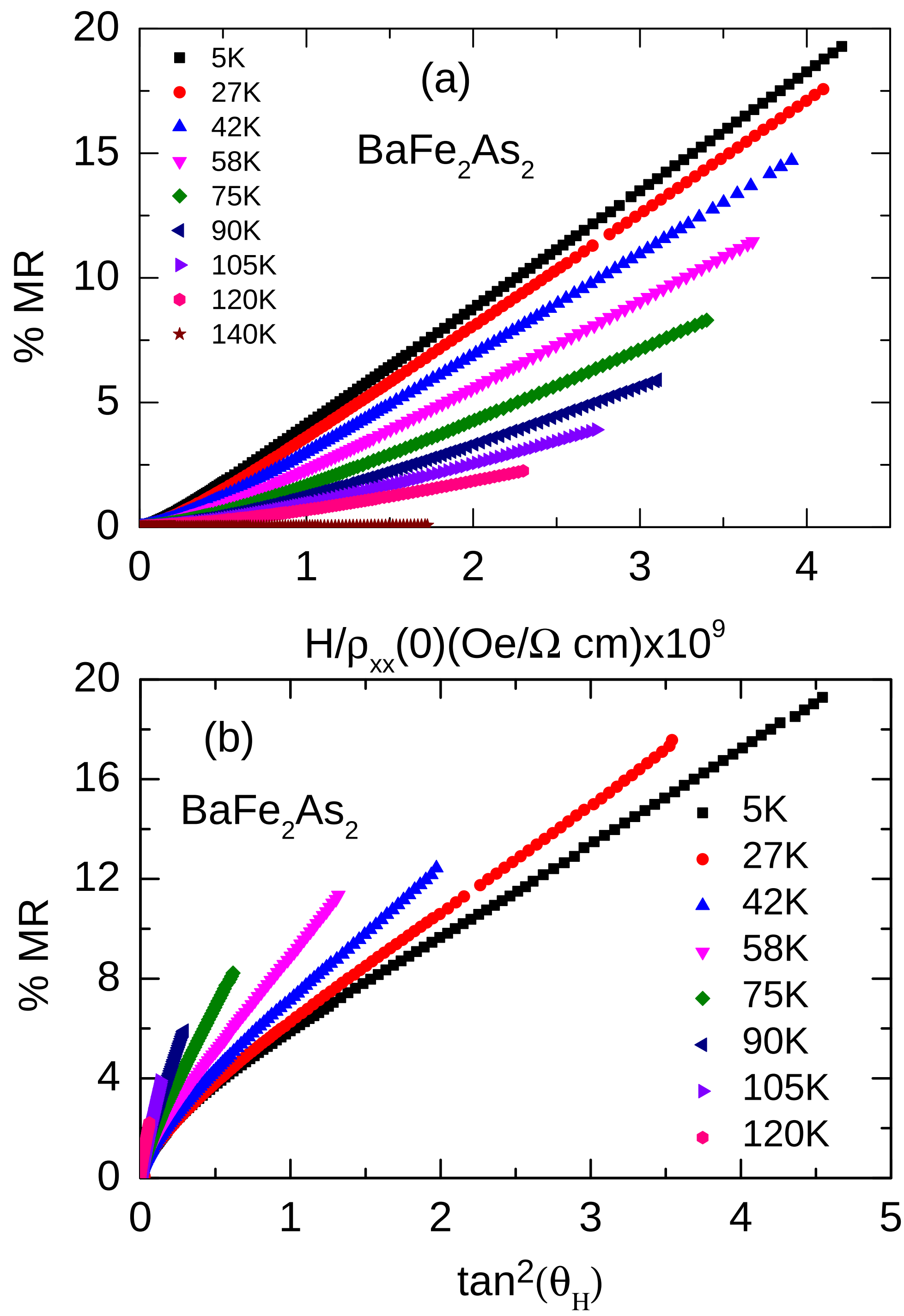

Figure 4.4: The Kohler and the modified Kohler's scaling of the magnetoresistance for the $BaFe_2As_2$ are shown in (a) and (b) respectively.

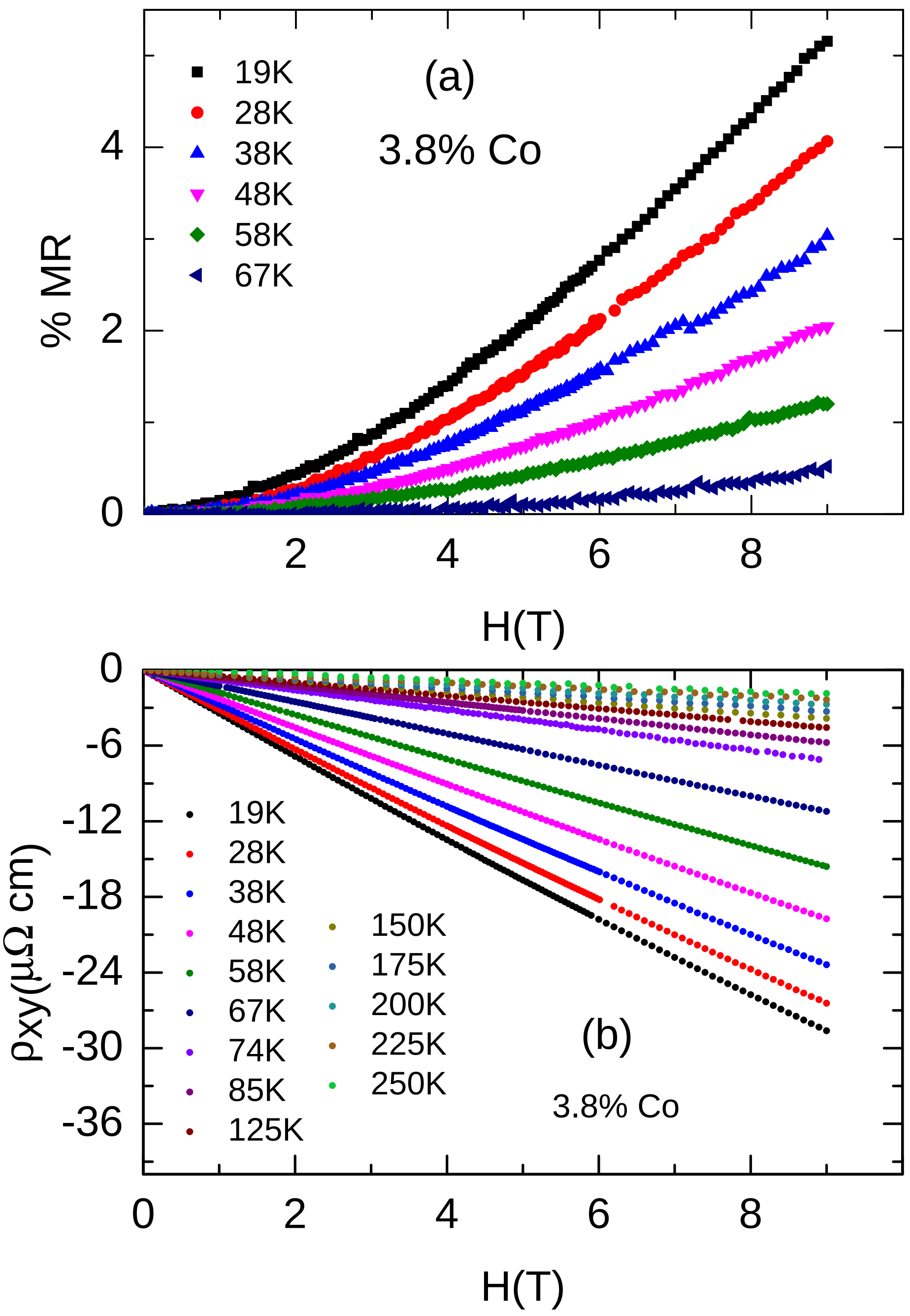

Figure 4.5: The magnetoresistance for the underdoped composition is shown in Figure 4.5(a). In (b), the Hall resistivity as a function of the applied magnetic field is shown for composition $x = 0.038$.

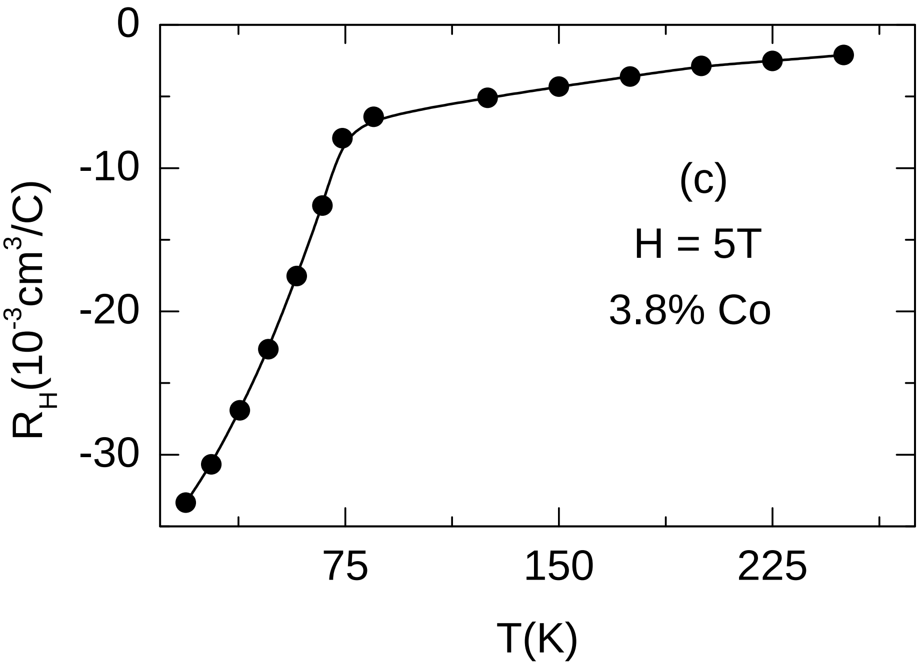

Figure 4.6: The Hall coefficient for the underdoped composition ($x = 0.038$) calculated using a magnetic field of 5 T is shown in Figure 4.6.

netoresistance is predicted in the quantum limit [156, 158, 159, 160]. The quantum limit conditions are: n $\ll$ $(eH/c\hbar)^{3/2}$ and T $\ll$ $eH\hbar/m^*$, where n is the density of charge carriers, and m^* is the effective carrier mass. Clearly, a low carrier density is a favorable condition for the linear magnetoresistance. Since the cobalt doping at Fe cites introduces extra electrons, thereby a reduced linear magnetoresistance (and Hall resistivity) is observed in this underdoped composition. The increase in carrier concertation is also supported by the Hall coefficient measurements, as can be seen in Figure 4.6.

The Hall coefficient ($|R_H|$) is substantially reduced (see Figure 4.6) by Co doping (compare with Figure 4.3), suggesting that Co doping leads to an increase in carrier concertation. Interestingly, the Hall coefficient has acquired a relatively stronger temperature dependence in the paramagnetic state, as opposed to the paramagnetic regime of the parent compound (see Figure 4.3) where, R_H is almost constant. Similar temperature dependent Hall coefficient in the paramagnetic regime of the underdoped composition of Sr($Fe_{1-x}Co_x$)$_2$$As_2$ was also observed (Chapter 3, Figure 3.5(b)), indicating that the unconventional behaviors in the underdoped (and optimally doped, as we will see in next section) compositions is a common feature of the 122 iron-pnictide superconducting families.

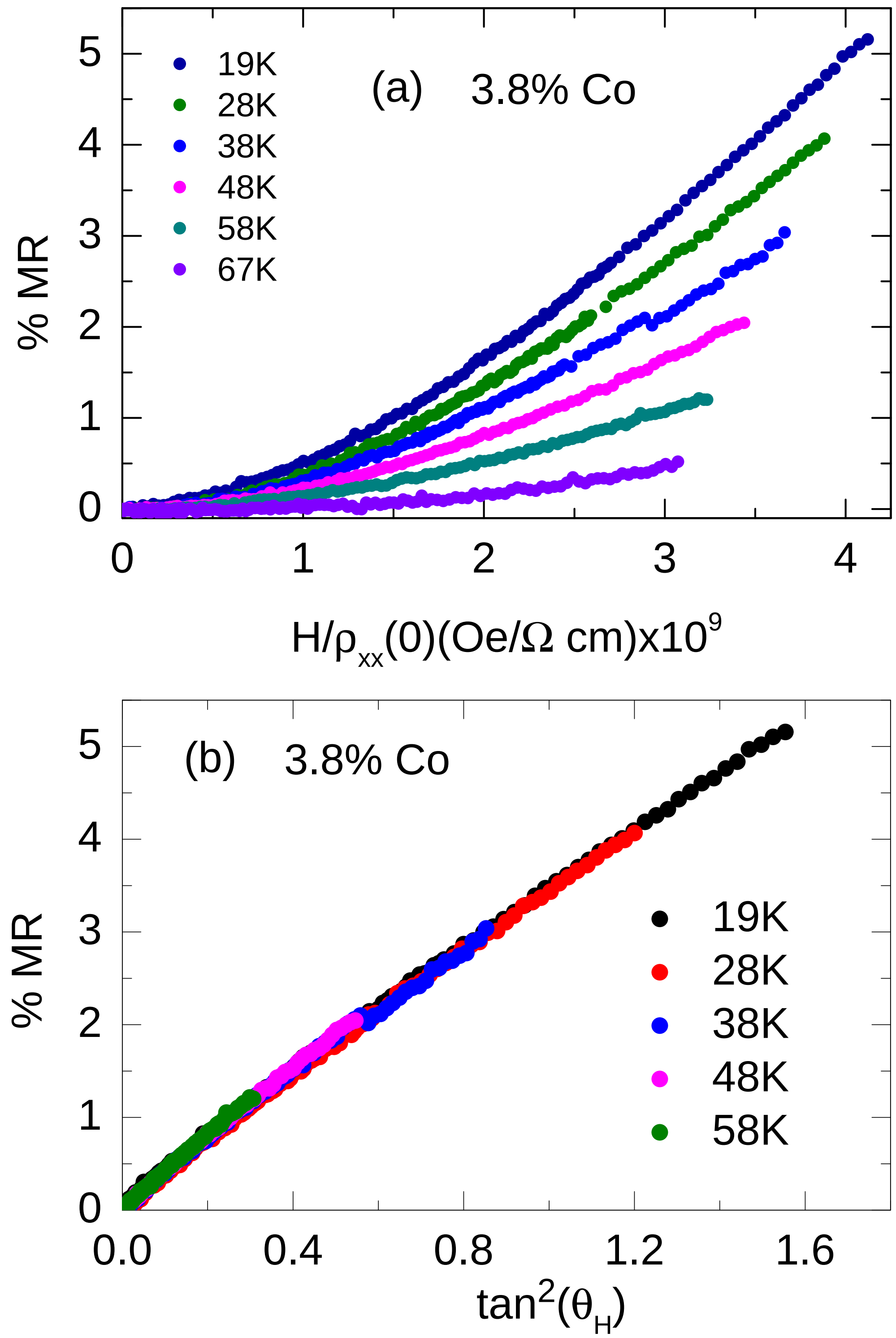

Figure 4.7: The Kohler and Modified Kohler's scaling of magnetoresistance for the underdoped composition ($x = 0.038$) are shown in (a) and (b) respectively.

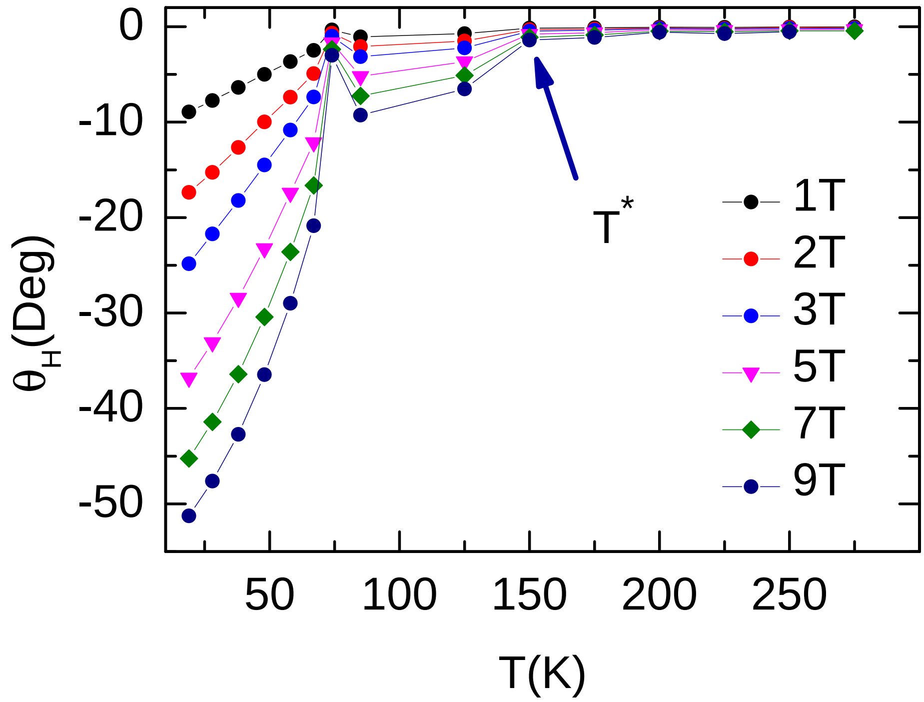

Figure 4.8: The Hall angle ($\theta_H = tan^{-1}(\rho_{xy}/\rho_{xx})$), as measured at several magnetic fields (as indicated in the inset) is shown for the $Ba(Fe_{0.962}Co_{0.038})_2As_2$ system. T* represent the anomaly associated with the pseudogap.

In Figure 4.7, we present the results of scaling analysis of the magnetoresistance for the underdoped composition $Ba(Fe_{0.962}Co_{0.038})_2As_2$. The Kohler's scaling of magnetoresistance is shown in Figure 4.7(a), where a clear violation of this scaling is observed. As mentioned earlier, multiband nature of FeSCs and strongly temperature dependent carrier concertation, which is also supported by the Hall coefficient measurements (see Figure 4.6) are all unfavorable conditions for the Kohler's rule [235], hence its violation in these systems is expected. In Figure 4.7(b), the modified Kohler's scaling of magnetoresistance is shown. As is evident, all magnetoresistance isotherms collapse onto a single curve, indicating that the modified Kohler's scaling is obeyed. This is the first report of the scaling analysis of magnetoresistance in any underdoped superconducting composition of $Ba(Fe_{1-x}Co_x)_2As_2$ series. Originally, the modified Kohler's scaling in cuprates is thought to be valid as a consequence of the anisotropic reconstructions of the Fermi Surface due to the 2D-antiferromagnetic spin fluctuations, in terms of the so-called 'hot' and 'cold' spots [93, 53, 92, 221]. Such anisotropic reconstruction gives rise to two relaxation rates τ_{tr} and τ_H, where the resistivity and magnetoresistance are governed by τ_{tr} and τ_H respectively. The hot (cold) spots are the regions of the Fermi surface where the charge carriers scatter rather strongly (weakly) due to the scattering from antiferromagnetic spin fluctuations [77]. It should be noted that in addition to high-T_C cuprates, the modified Kohler's scaling has been found to be valid in a number of heavy fermions as well [66, 72, 75]. Spin fluctuations have not only been proposed (and observed) to exist in the phase diagram of FeSCs but are also thought to be the pairing glue for the unconventional superconductivity in these systems [236, 42, 36, 232]. These observations (validity of modified Kohler's scaling) indicates that the magnetotransport in the underdoped region of $Ba(Fe_{1-x}Co_x)_2As_2$ series bears similarities to high-T_C cuprates and some heavy fermions. Interestingly, in a related underdoped $Ba(Fe_{1.96}Ni_{0.04})_2As_2$ system ($T_C \sim 15$ K), neutron scattering experiments have suggested that the effect of Ni doping is essentially to reduce the dimensionality of the $BaFe_2As_2$ system giving rise to quasi-2D spin fluctuations [42]. This might also be the case with the composition in the present study, and the reason for the apparent similarity of the magnetotransport of this system to some high-T_C cuprates and heavy fermions.

In figure 4.8, we present the Hall angle measurements for the underdoped system at several values of the magnetic field. In addition to an anomaly associated with the magnetic transition at ~ 74 K, an additional anomaly (indicated by T^*) is observed at ~ 150 K. This anomaly bears striking resemblance to the broad crossover seen in the interplane transport measurements for a very similar composition, which was ascribed to the presence of a pseudogap in this system [233]. Signatures of the pseudogap in similar compositions were also seen in Angle-resolved Photoemission (ARPES) [237] and Nuclear Magnetic Resonance (NMR) experiments [111]. It should be noted that the Hall angle is sensitive to the changes in electronic scattering and effective masses of charge carriers and has been extensively used to infer upon the presence of pseudogap in the phase diagram of high- T_C cuprates [121, 119, 120, 122, 78, 123, 124]. Although the Hall angle studies of iron-based superconductors have been limited, a few reports exist where the deviations from the power law behavior of Hall angle have been used to indicate the onset of a pseudogap phase [105, 106]. Presence of the pseudogap phase and the validity of modified Kohler's scaling suggests striking similarities between the underdoped regime of iron-based superconductors and high-T_C curates.

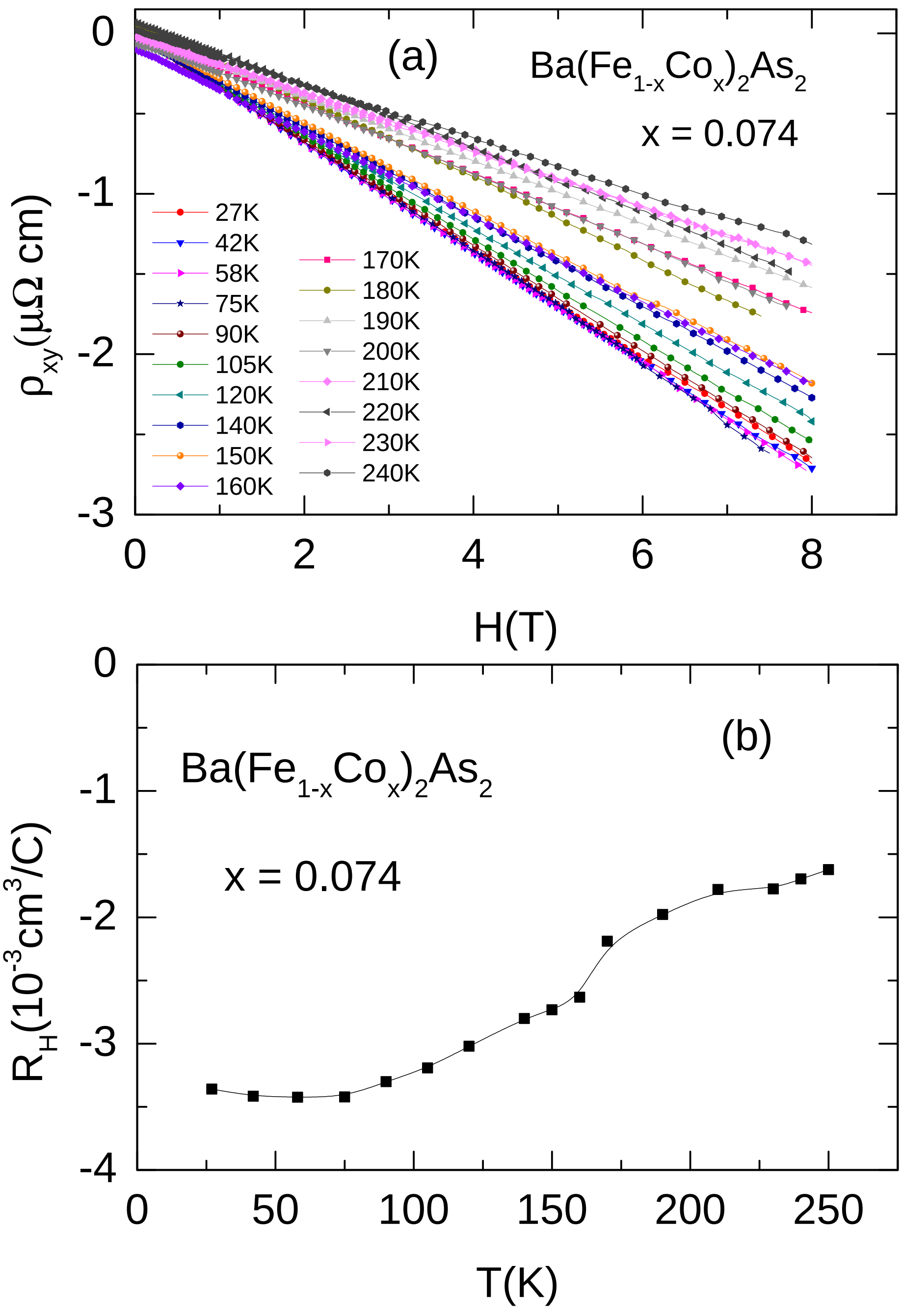

Figure 4.9: The Hall resistivity for the optimally doped composition $x = 0.074$ measured at several temperatures is shown in (a). In (b), the Hall coefficient calculated as a slope of the linear fit to the Hall resistivity is shown.

4.1.3 The optimally doped system: $x = 0.074$

In Figure 4.9(a), a comprehensive Hall resistivity data set for the optimally doped composition is shown. The Hall resistivity is linear in the magnetic field, in the entire temperature range shown in Figure 4.9(a). A similar H-linear Hall resistivity is also observed for the optimally doped composition of the $Sr(Fe_{1-x}Co_x)_2As_2$ series (see Figure 3.6(a), chapter3). Interestingly, the Hall coefficient as shown in Figure 4.9, has a pronounced temperature dependence, which is stronger than what is observed in the paramagnetic regime of the parent compound $BaFe_2As_2$ (Figure 4.3) and the underdoped composition $Ba(Fe_{0.962}Co_{0.038})_2As_2$ (Figure 4.6). This indicates an increasingly pronounced non-Fermi liquid behavior in the optimally doped composition, similar to that observed in the optimally doped composition of the $Sr(Fe_{1-x}Co_x)_2As_2$ series (Figure 3.6(b), Chapter 3) and some literature reports [201]. Another interesting observation is that, though the Hall coefficient has a strong temperature dependence above $\sim$ 70 K, it is almost constant below this temperature. Interestingly, a similar behavior was also observed for the optimally doped composition of the $Sr(Fe_{1-x}Co_x)_2As_2$ series (Figure 3.6(b), Chapter 3), where the Hall coefficient is approximately constant below $\sim$ 45 K. We suspect, this may be due to the presence of superconducting fluctuations, which somehow does not seem to affect the Hall resistivity. This proposal is supported by the following observations. The T_C in the optimally doped $Sr(Fe_{1-x}Co_x)_2As_2$ system is 15 K [192, 215, 205], which is $\sim$ 10 K lesser than the optimally doped composition of $Ba(Fe_{1-x}Co_x)_2As_2$ where the T_C is $\sim$ 25 K [188, 178, 198]. Since, superconducting transition temperature is higher for the optimally doped composition of the $Ba(Fe_{1-x}Co_x)_2As_2$ series (by $\sim$ 10 K), it is likely that the superconducting fluctuations (which apparently, does not affect R_H) also persist up to higher temperatures (up to $\sim$ 75 K) as compared the optimally doped composition of the $Sr(Fe_{1-x}Co_x)_2As_2$ series ($\sim$ 45 K). Unfortunately, the magnetoresistance in this optimally doped composition is very small, which did not allow us to carry out the scaling analysis of magnetotransport in this composition.

4.2 Conclusions

In conclusion, we reported the detailed magnetotransport studies of three distinctly different compositions of the $Ba(Fe_{1-x}Co_x)_2As_2$ series. We observed that both the Kohler as well as the modified Kohler's scaling does not work for the parent compound. On the other hand, though the Kohler's scaling is violated for the underdoped composition as well, modified Kohler's scaling works extremely well in this system. In the Hall angle measurements, an anomaly associated with the pseudogap like phase is observed in the underdoped composition, suggesting its relative similarity to the underdoped high-T_C cuprates.

Chapter 5

Thermodynamic and transport studies of $Ca_{1-x}Eu_xFe_2As_2$ series

5.1 Introduction

Parent compounds RFe_2As_2 (R = Ba, Sr etc.) of the 122 family of iron-based superconductors have been extensively studied in the past. These systems develop a superconducting ground state at low temperatures not only by charge doping but even by isovalent substitution and under pressure [238, 239, 240, 241, 242, 243, 244, 245, 206, 246, 247, 248, 249]. This flexibility provides a fertile ground to study the interplay of superconductivity and magnetism in the presence of substitutional disorder. However; the solid solutions of the type $R_{1-x}R'_xFe_2As_2$ (e.g., $Ca_{1-x}Eu_xFe_2As_2$) have been much less studied. Interestingly, these systems do not undergo a superconducting transition by chemical doping unlike the rich superconducting phase diagram shown by the doped RFe_2As_2 systems; however, the reports of superconductivity under pressure exist [250, 251, 252, 253]. So far there has only been a few studies where the $R_{1-x}R'_xFe_2As_2$ type solid solutions like $Ba_{1-x}Sr_xFe_2As_2$ [250, 254, 255], $Sr_{1-x}Ca_xFe_2As_2$ [250, 254, 255], $Ba_{1-x}Eu_xFe_2As_2$ [256] and $Eu_{1-x}Ca_xFe_2As_2$ [257] have been studied. Here we report detailed thermodynamic and transport properties of the $Ca_{1-x}Eu_xFe_2As_2$ (x = 0, 0.31, 0.48, 0.75, 0.9, 1) series in a much wider temperature-composition phase space.

There exists a solitary report where the magnetic properties of three compositions of Sn flux grown members of $Ca_{1-x}Eu_xFe_2As_2$ were studied [257]. Here we report detailed physical properties of six members of $Ca_{1-x}Eu_xFe_2As_2$ series grown by superior FeAs self-flux method. Here we present the trans-

Table 5.1: Nominal and actual composition x of the Eu for the samples investigated here.

Nominal composition	Actual composition
$x = 1$	1
$x = 0.8$	0.9
$x = 0.6$	0.75
$x = 0.40$	0.48
$x = 0.2$	0.31
$x = 0$	0

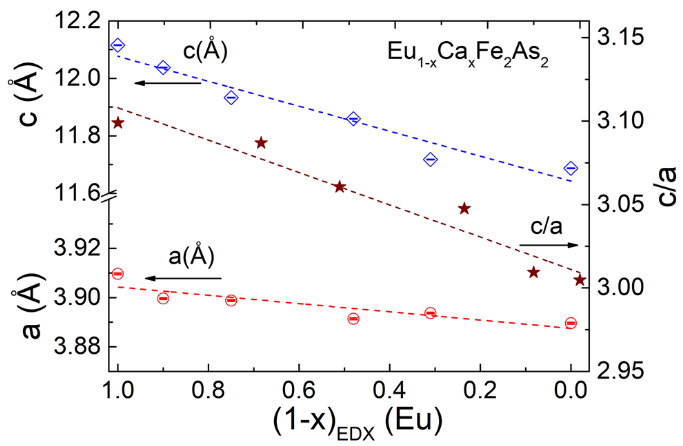

Figure 5.1: Variation of lattice parameters 'a' and 'c', and their ratio c/a for all the $Eu_{1-x}Ca_xFe_2As_2$ samples.

port and thermodynamic characterization of these systems. The lattice parameters variation as a function of x is shown in Figure 5.1; and table 5.1 summarizes the nominal (x) and actual or EDX concentration of Eu for various samples investigated here. In the rest of this chapter, we will use the EDX composition to designate these samples.

We have found that at higher doping levels ($x \geq 0.75$), the combined magnetostructural transition at T_0 associated with Fe moments remains almost constant. However, it decreases gradually below this critical concentration $x_c = 0.75$. On the other hand, antiferromagnetic ordering temperature T_N of Eu moments decreases from $\sim$ 18 K rather smoothly with x and vanishes at x_c. These observations suggest a subtle coupling between Eu and Fe magnetic sublattices.

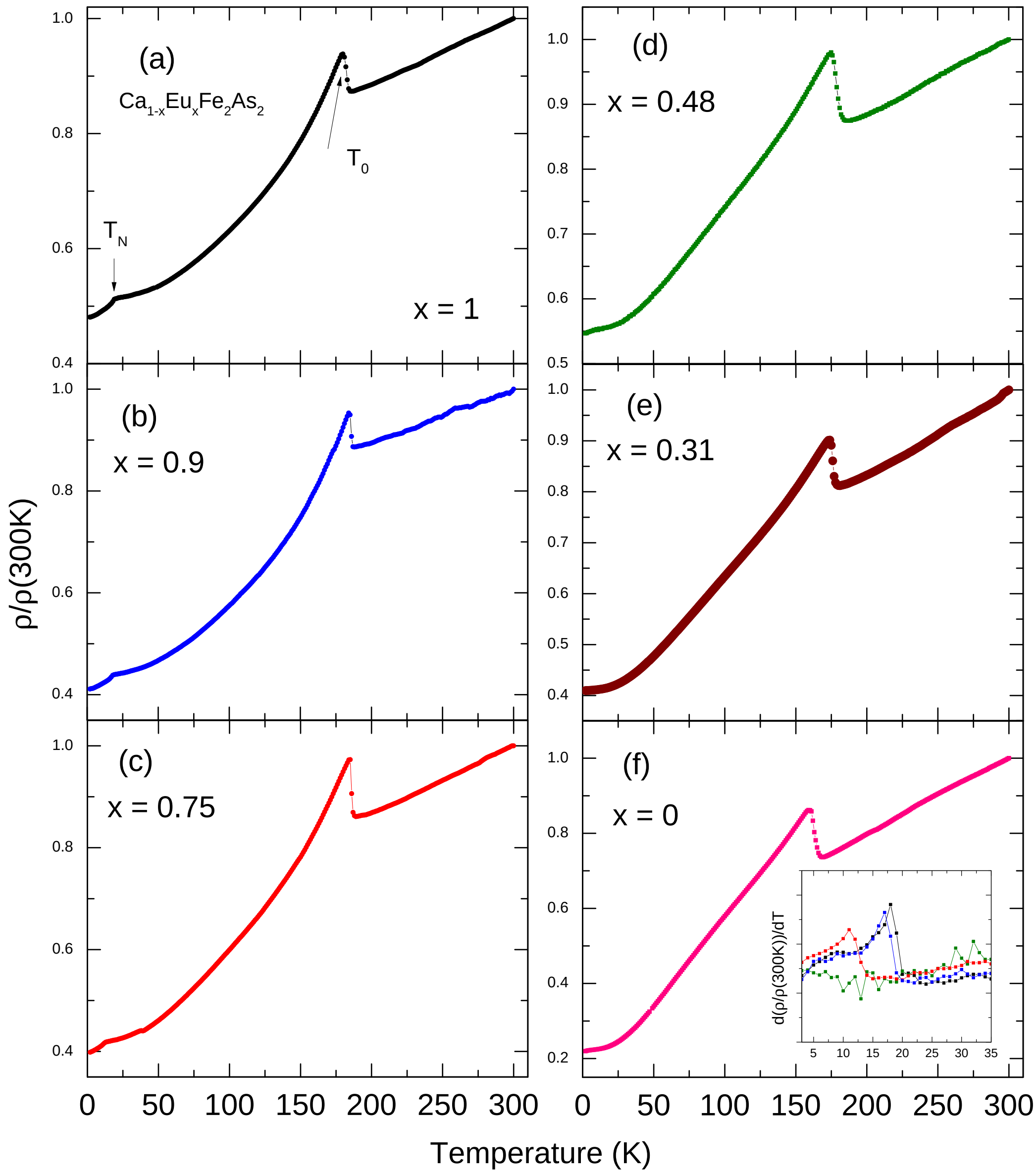

Figure 5.2: (a)-(f) depicts the in-plane resistivity of $Ca_{1-x}Eu_xFe_2As_2$ samples. Inset in Figure 5.2(f) depicts d(ρ/ρ(300K)/dT at low temperatures for all six compositions with same color coding as used in the main panels.

5.2 Results and discussion

In Figure 5.2(a)-(f), we present the normalized resistivity $\rho(T)/\rho(300K)$ for all six compositions of $Ca_{1-x}Eu_xFe_2As_2$ series where the doping level for each composition is indicated in the inset of the corresponding subfigure. As is evident, the resistivity decreases with temperature indicating a metallic behavior in all compositions. Sharp anomaly in the temperature range $\sim$ 190-160 K (highlighted by an arrow and denoted by T_0 in (a)), which is seen for all compositions, correspond to the magnetic/structural transition. An additional anomaly associated with the ordering of Eu moments [245, 241, 258, 259] at low temperatures below $\sim$ 20 K is also seen in (a), (b) and (c) (highlighted by an arrow and denoted by T_N in (a)). It should be noted that at the anomaly associated with the ordering of Eu^{2+} magnetic moments ($4f^7$ configuration, S = 7/2 [259, 260]) is not visible at low Eu concentration (below $\sim x < 0.75$). This is highlighted in the inset of Figure 5.2(f), where the first temperature derivative of the normalized resistivity ($d(\rho/\rho(300K))/dT$) is plotted in the low temperature region, where no anomaly is visible for $x = 0.48$ (Olive color).

In Figure 5.3, we present the specific heat (C_P) data for $Ca_{1-x}Eu_xFe_2As_2$ (x = 0, 0.31, 0.48, 0.75, 0.9, 1) series. The pronounced anomaly at high temperatures ($\sim$160-190 K) corresponds to the magnetic/structural transition. An additional anomaly at low temperatures is also apparent for the compositions $x \geq 0.75$. These observations are consistent with transport measurements presented in Figure 5.2. In the inset, low-temperature data is shown to depict the ordering temperature of Eu^{2+} moments more clearly. It is evident that there is no clear anomaly at low temperatures for $x \leq 0.75$. However, excess specific heat is apparent in compositions $x = 0.48$ and 0.31, which is not present in $x = 0$, i.e., $CaFe_2As_2$, indicating its magnetic origin related to the short-range ordering of the Eu^{2+} moments.

To illustrate the evolution of magnetic/structural transition at T_0; and the antiferromagnetic ordering of Eu^{2+} moments at low temperatures, a phase diagram is constructed from the transport as well as thermodynamic measurements, which is shown in Figure 5.4.

T_0 is almost constant for $x \geq 0.75$ and decreases gradually below x_c from $\sim$184 K at $x = 1$ ($EuFe_2As_2$) to $\sim$ 163 K at $x = 0$ ($CaFe_2As_2$). Interestingly, T_N decreases from 19.1 K to being undetectable at compositions below x_c. The vertical line in Figure 5.4, indicates the critical composition x_c below which a gradual decrease in T_0 is observed and at which point T_N becomes unobservable in our experiments. Interestingly, the measurements on some annealed crystals also indicated a similar evolution of T_N and T_0, as reported in our work [261]. These observations are also in agreement with some mag-

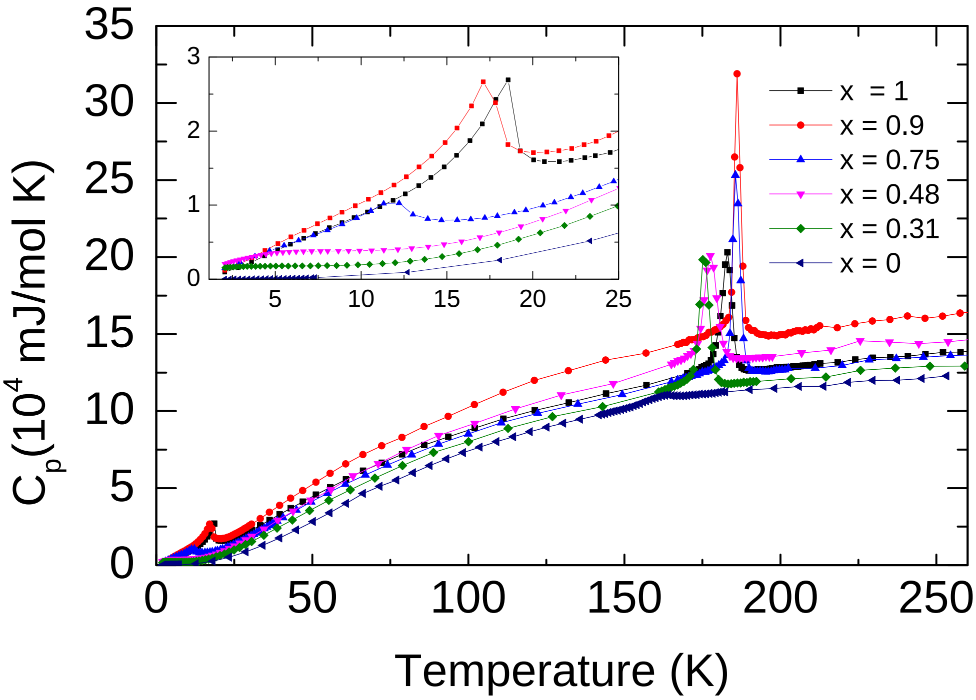

Figure 5.3: Specific heat for all six members of the $Ca_{1-x}Eu_xFe_2As_2$ ($x = 0$, 0.31, 0.48, 0.75, 0.9, 1) series is shown as a function of temperature (T). The inset depicts low temperature anomaly associated with the Eu^{2+} moments. Identical color coding is used to represent the data in the main panel and the inset.

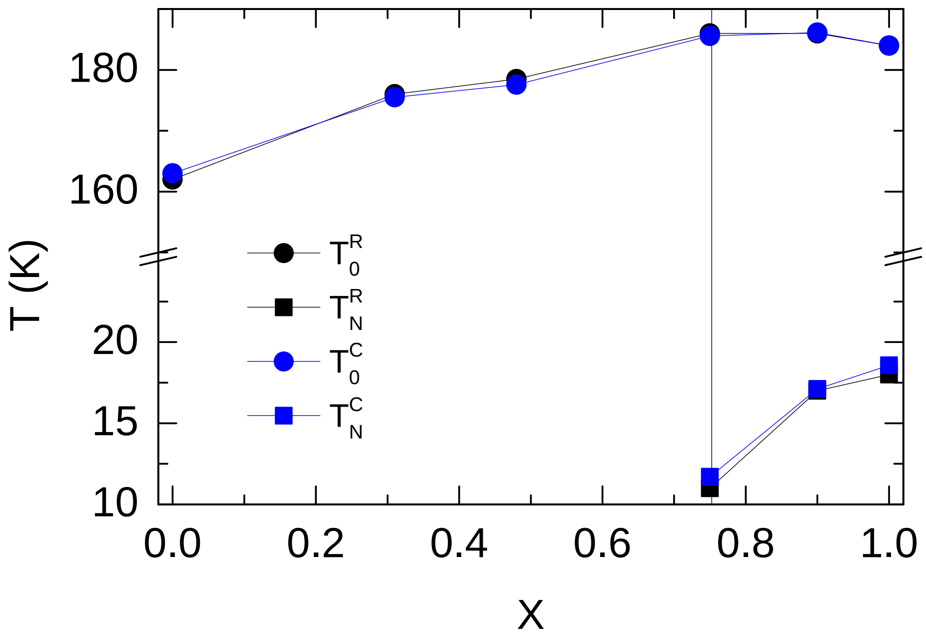

Figure 5.4: Temperature versus composition phase diagram for $Ca_{1-x}Eu_xFe_2As_2$. Black and blue symbols correspond to the data points obtained from the transport and thermodynamic probes, respectively. Superscripts R and C in T_0 and T_N refers to the resistivity and heat capacity probes. Vertical line at $x_c = 0.75$ is drawn as a guide to the eye.

Table 5.2: The list of transition temperatures associated with the magnetic/structural transition of the Fe sub lattice at T_0 and antiferromagnetic order of Eu sublattices a T_N is shown. Superscripts 'R' and 'C' refers to the transport and thermodynamic probes respectively.

x	T_0^R	T_N^R	T_0^C	T_N^C
$x = 1$	184 K	18 K	186 K	18.57 K
$x = 0.9$	186 K	17 K	186.1 K	17.1 K
$x = 0.75$	186 K	11 K	185.57 K	11.7 K
$x = 0.48$	178.5 K	–	177.5 K	–
$x = 0.31$	176 K	–	175.5	–
$x = 0$	162 K	–	163 K	–

netic studies on Sn flux grown crystals of $Ca_{1-x}Eu_xFe_2As_2$ [257]. In table 5.2, the transition temperatures corresponding to the magnetic ordering of Fe and Eu sublattices are listed, where a good agreement between the transport and thermodynamic measurements is observed. It should be noted that the results presented here for the end members of this series (i.e., $EuFe_2As_2$ and $CaFe_2As_2$) are also consistent with literature [247, 253, 257].

Prior neutron studies have shown that Eu moments align ferromagnetically in the crystallographic ab plane and order into the so-called A-type antiferromagnetic structure where Eu spins align antiferromagnetically along the c axis [259]. To further understand the nature of low-temperature anomaly at T_N, we have carrier out magnetic field dependent thermodynamic measurements. Figure 5.5 (a) and (b) depicts the evolution of magnetic order of Eu^{+2} moments under the applied magnetic field for $EuFe_2As_2$ ($x = 1$) and $Ca_{0.25}Eu_{0.75}Fe_2As_2$ ($x = 0.75$) respectively. T_N quickly gets suppressed to lower temperatures after the application of the magnetic field, and transition becomes broad and ill-defined at higher magnetic fields. For instance, the value of T_N, which is 18.6 and 11.7 K for the $x = 1$, and 0.75, respectively, shifted to 15.1 K and 6.7 K at H = 1T. Such reduction of T_N with the application of magnetic field is consistent with what is typically seen in conventional antiferromagnets [262]. Interestingly, at even higher fields, an additional feature in the form of a broad hump can be seen above 20 K in both (a) and (b). This suggests the possibility of a magnetic field induced metamagnetic transition. Field-induced metamagnetic transition is also manifested in the isothermal magnetization at T = 2 K shown in Figure 5.6 (Figure is taken from our publication [261]). It is evident from Figure 5.6, that the M-H isotherms (at 2 K) for samples with high Eu concentration ($x > 0.75$) changes slope before saturating at higher magnetic fields,

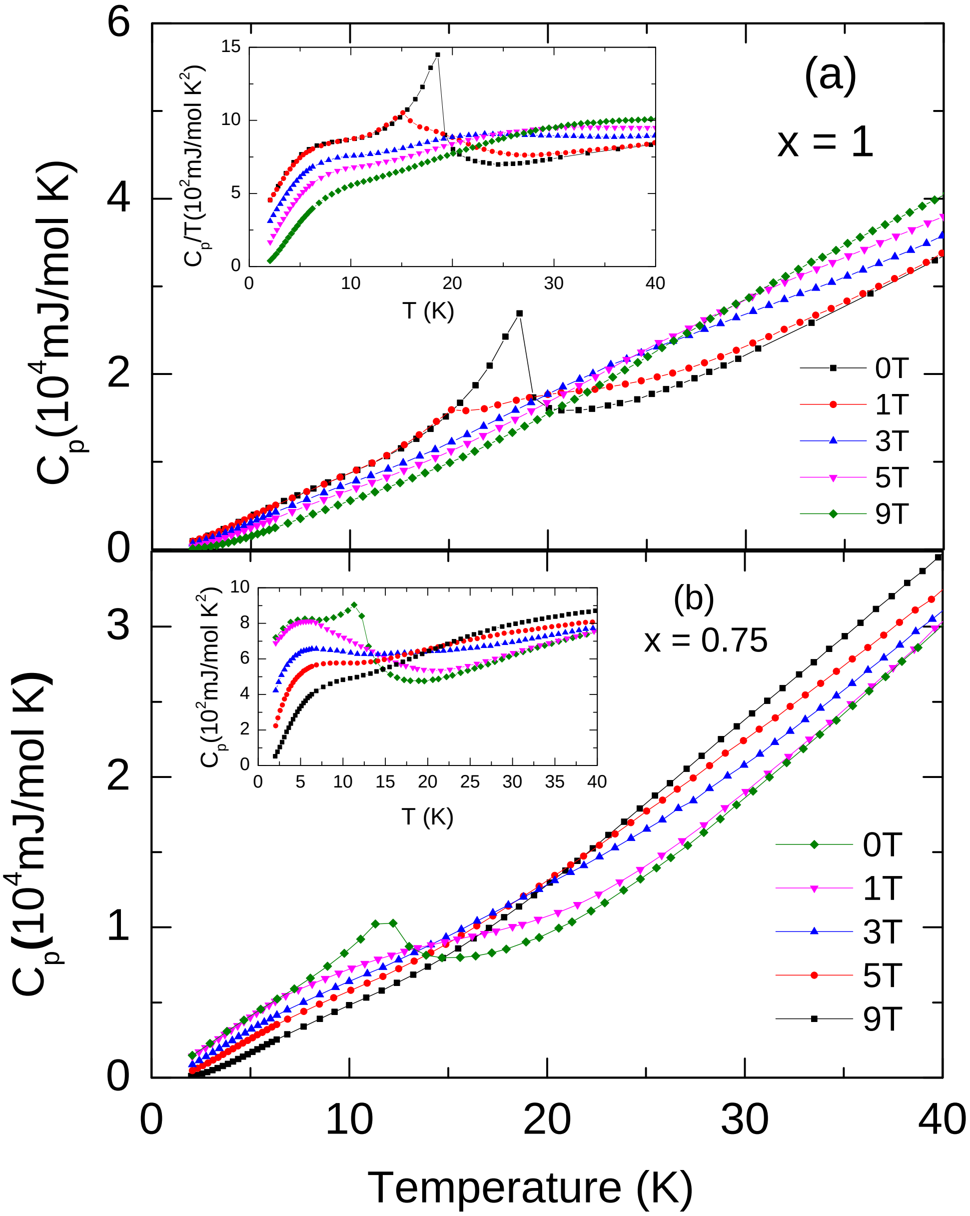

Figure 5.5: Specific heat (C_p) as a function of temperature at several values of applied magnetic field is shown for the $x = 1$ and $x = 0.75$ compositions in (a) and (b), respectively. The insets in (a) and (b) depicts C_p/T as a function of temperature at different magnetic fields as indicated by the legends in lower right corner of each Figure.

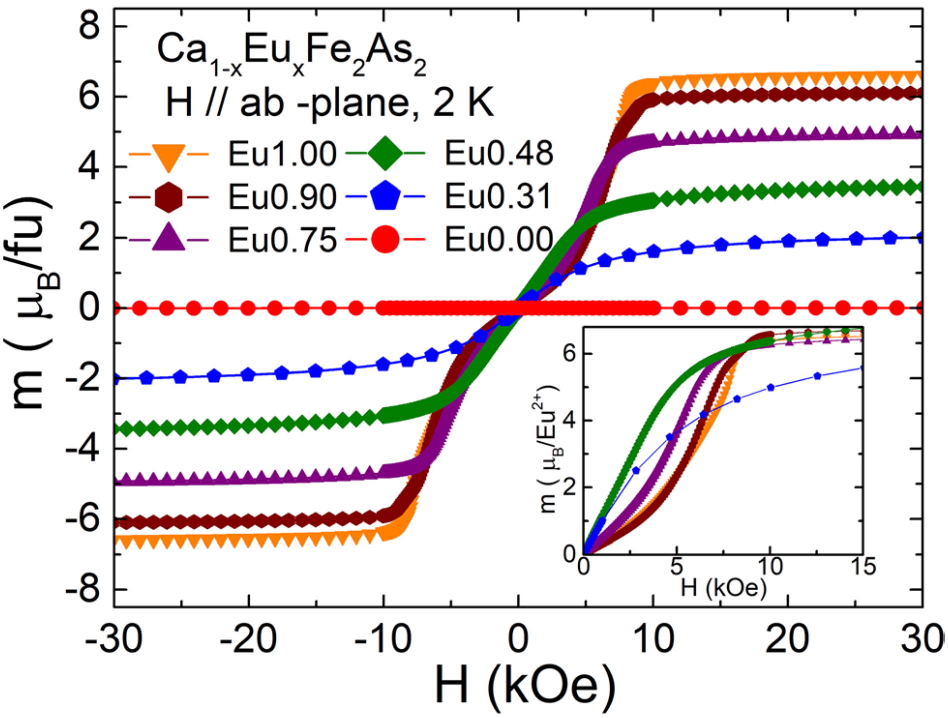

Figure 5.6: Magnetization versus magnetic field data at 2 K for all samples studied here is shown in Figure 5.6. Eu1.00 etc., in the inset, depicts the actual Eu concentration. The inset depicts a low field view of the data (in μ_B/Eu^{2+} units on the Y-axis.). Same color coding is used for data in the main panel as well as in the inset.

whereas this behavior is not present in samples with low Eu concentration (x < 0.75). This possibility has been previously discussed in the literature in neutron and magnetic measurements on $EuFe_2As_2$, and our results support such a scenario [260, 263].

5.3 Conclusions

In conclusion, we performed detailed transport and thermodynamic measurements on six members of the $Ca_{1-x}Eu_xFe_2As_2$ series. We observed that although the antiferromagnetic ordering temperature of Eu moments decreases gradually with decreasing x, magnetostructural transition remains almost constant until the Eu moment ordering is completely suppressed at a critical concentration x_c. Once Eu^{+2} order is destroyed, the magnetostructural transition associated with Fe^{+2} moments decreases gradually with x. These observations suggest a subtle coupling between the Fe and Eu magnetic sublattices. Also, a magnetic field induced metamagnetic like transition above ~ 20 K is observed for the $x = 1$ and $x = 0.75$ compositions.

Chapter 6

Conclusions and future directions

6.1 Conclusions

Comprehensive magnetotransport studies of two electron-doped $Ba(Fe_{1-x}Co_x)_2As_2$ and $Sr(Fe_{1-x}Co_x)_2As_2$ families were carried in this thesis. Three distinctly different compositions, i.e., the parent compound $Ba(Sr)Fe_2As_2$, underdoped composition ($x = 0.038$ for Ba series and $x = 0.06$ for Sr series) and the optimally doped compositions ($x = 0.074$ for Ba series and $x = 0.12$ for Sr series) were studied for each family. The motivation was to put these systems in perspective with the other unconventional superconductors like high-T_C cuprates and heavy fermions. For this purpose, scaling techniques of the magnetotransport were employed, which have also been a powerful tool to identify the commonalities between heavy fermions, high-T_C cuprates and other strongly correlated electron systems in the past.

Our observations indicated that the Kohler's scaling is violated in all these systems, which might be due to the multiband nature and temperature evolution of carrier concentration in these systems. Interestingly, the modified Kohler's scaling was found to be valid in the underdoped composition ($x = 0.038$) of $Ba(Fe_{1-x}Co_x)_2As_2$ series. This composition also shows an anomaly in the Hall angle measurements, which we believe may indicate the presence of a pseudogap like phase in this system. Supportive evidence for the pseudogap feature for this particular composition was also reported in the interplane transport [233], ARPES [237] and NMR studies [111]. These observations suggest that the magnetotransport behavior of this underdoped composition is similar to what is typically seen in high-Tc cuprates where not only the modified Kohler's scaling is valid, but the presence of pseudogap is also well established [102, 54]. An analogous study in the $Sr(Fe_{1-x}Co_x)_2As_2$ series could not be done because of extremely small magnetoresistance for the underdoped sample of this series.

Scaling analysis of the magnetotransport in $Sr(Fe_{1-x}Co_x)_2As_2$ series reveals its rather unusual behavior. We discovered that although the modified Kohler's scaling is invalid in the optimally doped system, the Hall angle has a T^2 dependent behavior. These observations are self-contradictory and suggest that the magnetoresistance and Hall angle may be governed by two different relaxation rates. Interestingly, similar behavior was observed in the magnetotransport behavior of high-T_C cuprates in a number of studies, where authors proposed that modified Kohler's rule may not be universally applicable to all high-T_C cuprates, however much attention was not given to these observations. Our observations are the first in iron-based superconductors which also points to the non-universality of the modified Kohler's rule. Another interesting observation is that of a linear magnetoresistance in the optimally doped composition ($x = 0.12$) of $Sr(Fe_{1-x}Co_x)_2As_2$ series. This linear magnetoresistance is discussed in the context of several existing models of magnetoresistance.

Another observation is that the Hall resistivity is non-linear in the magnetic state of all member of the $Ba(Fe_{1-x}Co_x)_2As_2$ and $Sr(Fe_{1-x}Co_x)_2As_2$ series, however it is linear in the paramagnetic regime of all of these compositions, including the optimally doped compositions which do not have any magnetic ground state. These observations suggest that the magnetism may be responsible for this non-linearity, however, the microscopic mechanism behind this anomalous behavior remains unknown.

We have also determined detailed thermodynamic and transport properties of a relatively understudied $Ca_{1-x}Eu_xFe_2As_2$ (x =1, 0.9, 075, 048, 0.31, 0) series. We have observed that superconductivity is not shown by any member of this series. Also, a subtle coupling between Eu and Fe magnetic sublattices is observed. It is found that transition temperature associated with the ordering of Eu moments decreases gradually and vanish at a critical concentration x_c. Interestingly, the transition temperature associated with Fe sublattice remains constant in this doping range and decreases only below x_c. Magnetic field dependent specific heat measurements also suggest the presence of a field-induced metamagnetic transition above $\sim$ 20 K.

6.2 Future directions

Our extensive magnetotransport studies in 122 iron pnictide families highlighted new avenues, and certain aspects of these materials, which can be further explored. Additionally, over the past few years, some interesting new superconducting materials classes have also been discovered, which seems to have the potential to be used as model systems to study long-standing issues in the field of high-T_C superconductivity. We will briefly discuss some these here.

As we have seen from the magnetotransport in three distinctly different compositions of $Ba(Fe_{1-x}Co_x)_2As_2$ and $Sr(Fe_{1-x}Co_x)_2As_2$ series in this thesis, underdoped composition $x = 0.038$ of $Ba(Fe_{1-x}Co_x)_2As_2$ series stands out. Magnetotransport behavior in the magnetic state of this underdoped composition bears a striking similarity to underdoped high-Tc cuprates and some heavy fermions because it not only obeys the modified Kohler's rule but also depicts an anomaly presumably associated with the pseudogap. Interestingly, a similar underdoped composition of $Ba(Fe_{1-x}Ni_x)_2As_2$ series, namely the $BaFe_{2-x}Ni_xAs_2$ ($x = 0.04$, $T_C = 15$ K) was shown to have 2D- anisotropic spin fluctuations in neutron studies [42], which are thought be responsible for the unconventional behavior in high-T_C cuprates and heavy fermions. Since, the magnetoresistance in the paramagnetic regime in most FeSCs is very small, which hampers the scaling analysis of its magnetotransport, magnetically ordered state of underdoped compositions serves as an important platform for magnetotransport studies, where the magnetoresistance is measurable. We believe, underdoped (transition metal doped) superconducting compositions of other families like (Ca, Eu, Ba, Sr)$(Fe_{1-x}T_x)_2As_2$ (T = Co, Ni, Zn, etc.) should be studied. This will help understand whether a magnetotransport behavior similar to $x = 0.038$ of $Ba(Fe_{1-x}Co_x)_2As_2$ series is observed in the underdoped compositions of these families or not. Such a study will be of great importance for future theoretical developments as well.

Surprisingly, the studies that discuss the influence of superconducting fluctuations on the normal state transport properties of FeSCs have been very limited [264, 265, 266]. This is in contrast to the high-T_C cuprates, where the tremendous amount of work has been devoted to study the influence of superconducting fluctuations on normal state transport properties [8, 267, 268, 269, 270, 271, 272, 273, 274]. As we have discussed in chapter 3 and 4, superconducting fluctuations apparently affect the normal state magnetotransport in $Ba(Fe_xCo_x)_2As_2$ and $Sr(Fe_xCo_x)_2As_2$ series. Magnetotransport in these systems (in the immediate vicinity and possibly up to 40-50

K above the superconducting transition) should be investigated in detail. It will be interesting to quantify and eliminate the contribution of superconducting fluctuations, and reevaluate the validity (or lack thereof) of Kohler and modified Kohler's rule in these systems.

Since the scaling analysis of magnetotransport has been very limited in FeSCs in general, it will be very interesting to extend it to other families, particularly the recently discovered $RAFe_4As_4$ (A = K, Rb, Cs, R = Ca, Sr) type systems [275]. These systems are considered as the hybrid of RFe_2As_2 and AFe_2As_2 type Fe Pnictides. However, due to the large size difference between the R and A type cations, R and A cations occupy nonequivalent crystallographic sites (unlike the solid solutions of the type $Ba_{1-x}K_xFe_2As_2$ and $Sr_{1-x}Na_xFe_2As_2$, where Ba(Sr) and K(Na) occupy equivalent crystallographic sites). These systems show the superconductivity with $T_C \sim$ 31-36 K without even doping. Although the magnetotransport studies of these systems are nonexistent, their unconventional behavior is seemingly clear in other measurements. For instance, the resistivity above the superconducting transition in some of these systems is remarkably linear up to 100 K. Interestingly, the single crystals of centimeters size have been reported to be grown using the FeAs self-flux technique [276], which will facilitate detailed transport measurements.

Bibliography

[1] G. R. Stewart. Unconventional superconductivity. *Advances in Physics*, 66(2):75–196, 2017.

[2] Johnpierre Paglione and Richard L Greene. High-temperature superconductivity in iron-based materials. *Nature physics*, 6(9):645, 2010.

[3] A.V. Chubukov R. M. Fernandes and J. Schmalian. What drives nematic order in iron-based superconductors? *Nature Physics*, 10:97–104, 2014.

[4] Deepa Kasinathan, Alim Ormeci, Katrin Koch, Ulrich Burkhardt, Walter Schnelle, Andreas Leithe-Jasper, and Helge Rosner. AFe_2As_2 (A= Ca, Sr, Ba, Eu) and $SrFe_{2-x}TM_xAs_2$ (TM= Mn, Co, Ni): crystal structure, charge doping, magnetism and superconductivity. *New journal of physics*, 11(2):025023, 2009.

[5] C.H. Lee, K. Kihou, A. Iyo, H. Kito, P.M. Shirage, and H. Eisaki. Relationship between crystal structure and superconductivity in iron-based superconductors. *Solid State Communications*, 152(8):644 – 648, 2012. Special Issue on Iron-based Superconductors.

[6] Y Mizuguchi, Y Hara, K Deguchi, S Tsuda, T Yamaguchi, K Takeda, H Kotegawa, H Tou, and Y Takano. Anion height dependence of T_C for the Fe-based superconductor. *Superconductor Science and Technology*, 23(5):054013, 2010.

[7] A. V. Chubukov, D. V. Efremov, and I. Eremin. Magnetism, superconductivity, and pairing symmetry in iron-based superconductors. *Phys. Rev. B*, 78:134512, Oct 2008.

[8] T. Kimura, S. Miyasaka, H. Takagi, K. Tamasaku, H. Eisaki, S. Uchida, K. Kitazawa, M. Hiroi, M. Sera, and N. Kobayashi. In-plane and out-of-plane magnetoresistance in $La_{2-x}Sr_xCuO_4$ single crystals. *Phys. Rev. B*, 53:8733–8742, Apr 1996.

[9] Gang Xiao, Peng Xiong, and Marta Z. Cieplak. Universal Hall effect in $La_{1.85}Sr_{0.15}Cu_{1-x}A_xO_4$ systems ((A= Fe, Co, Ni, Zn, Ga). *Phys. Rev. B*, 46:8687–8690, Oct 1992.

[10] Hanno Essn and Miguel C. N. Fiolhais. Meissner effect, diamagnetism, and classical physics − a review. *American Journal of Physics*, 80(2):164–169, 2012.

[11] Dirk Van Delft and Peter Kes. The discovery of superconductivity. *Physics Today*, 63(9):38–43, 2010.

[12] Michael R. Norman. The challenge of unconventional superconductivity. *Science*, 332(6026):196–200, 2011.

[13] Igor I Mazin. Superconductivity gets an iron boost. *Nature*, 464(7286):183, 2010.

[14] Fa Wang and Dung-Hai Lee. The electron-pairing mechanism of iron-based superconductors. *Science*, 332(6026):200–204, 2011.

[15] Yoichi Kamihara, Hidenori Hiramatsu, Masahiro Hirano, Ryuto Kawamura, Hiroshi Yanagi, Toshio Kamiya, and Hideo Hosono. Iron-based layered superconductor: LaOFeP. *Journal of the American Chemical Society*, 128(31):10012–10013, 2006. PMID: 16881620.

[16] Yoichi Kamihara, Takumi Watanabe, Masahiro Hirano, and Hideo Hosono. Iron-based layered superconductor $La[O_{1-x}F_x]FeAs$ (x = 0.050.12) with $T_C = 26$ K. *Journal of the American Chemical Society*, 130(11):3296–3297, 2008. PMID: 18293989.

[17] Xianhui Chen, Pengcheng Dai, Donglai Feng, Tao Xiang, and Fu-Chun Zhang. Iron-based high transition temperature superconductors. *National Science Review*, 1(3):371–395, 2014.

[18] David C. Johnston. The puzzle of high temperature superconductivity in layered iron pnictides and chalcogenides. *Advances in Physics*, 59(6):803–1061, 2010.

[19] G. R. Stewart. Superconductivity in iron compounds. *Rev. Mod. Phys.*, 83:1589–1652, Dec 2011.

[20] D. J. Singh. Electronic structure and doping in $BaFe_2As_2$ and LiFeAs: Density functional calculations. *Phys. Rev. B*, 78:094511, Sep 2008.

[21] C.W. Chu and B. Lorenz. High pressure studies on Fe-pnictide superconductors. *Physica C: Superconductivity*, 469(9):385 – 395, 2009. Superconductivity in Iron-Pnictides.

[22] Athena S Sefat. Pressure effects on two superconducting iron-based families. *Reports on Progress in Physics*, 74(12):124502, 2011.

[23] Milton S. Torikachvili, Sergey L. Bud'ko, Ni Ni, and Paul C. Canfield. Pressure induced superconductivity in $CaFe_2As_2$. *Phys. Rev. Lett.*, 101:057006, Jul 2008.

[24] M. S. Torikachvili, S. L. Bud'ko, N. Ni, P. C. Canfield, and S. T. Hannahs. Effect of pressure on transport and magnetotransport properties in $CaFe_2As_2$ single crystals. *Phys. Rev. B*, 80:014521, Jul 2009.

[25] Patricia L Alireza, Y T Chris Ko, Jack Gillett, Chiara M Petrone, Jacqueline M Cole, Gilbert G Lonzarich, and Suchitra E Sebastian. Superconductivity up to 29 K in $SrFe_2As_2$ and $BaFe_2As_2$ at high pressures. *Journal of Physics: Condensed Matter*, 21(1):012208, 2009.

[26] Qimiao Si and Frank Steglich. Heavy fermions and quantum phase transitions. *Science*, 329(5996):1161–1166, 2010.

[27] Louis Taillefer. Scattering and pairing in cuprate superconductors. *Annual Review of Condensed Matter Physics*, 1(1):51–70, 2010.

[28] V. A. Sidorov, M. Nicklas, P. G. Pagliuso, J. L. Sarrao, Y. Bang, A. V. Balatsky, and J. D. Thompson. Superconductivity and quantum criticality in $CeCoIn_5$. *Phys. Rev. Lett.*, 89:157004, Sep 2002.

[29] Y. Mugino, S. Kawasaki, M. Yashima, H. Mukuda, Y. Kitaoka, H. Shishido, and Y. nuki. ^{115}In-NQR study of $CeRh_{1-x}Ir_xIn_5$ under pressure. *Journal of Magnetism and Magnetic Materials*, 310(2, Part 1):584 – 586, 2007. Proceedings of the 17th International Conference on Magnetism.

[30] Shinji Kawasaki, Mitsuharu Yashima, Yoichi Mugino, Hidekazu Mukuda, Yoshio Kitaoka, Hiroaki Shishido, and Yoshichika Ōnuki. Enhancing the superconducting transition temperature of $CeRh_{1-x}Ir_xIn_5$ due to the strong-coupling effects of antiferromagnetic spin fluctuations: An ^{115}In nuclear quadrupole resonance study. *Phys. Rev. Lett.*, 96:147001, Apr 2006.

[31] A. J. Schofield. Non-Fermi liquids. *Contemporary Physics*, 40(2):95–115, 1999.

[32] Rohit Kumar, Luminita Harnagea, Archana Lakhani, and Sunil Nair. Magnetotransport studies of optimally doped $Sr(Fe_{1-x}Co_x)_2As_2$. *Journal of Physics: Condensed Matter*, 30(50):505601, 2018.

[33] David Mandrus, Athena S. Sefat, Michael A. McGuire, and Brian C. Sales. Materials chemistry of $BaFe_2As_2$: A model platform for unconventional superconductivity. *Chemistry of Materials*, 22(3):715–723, 2010.

[34] Chul-Ho Lee, Akira Iyo, Hiroshi Eisaki, Hijiri Kito, Maria Teresa Fernandez-Diaz, Toshimitsu Ito, Kunihiro Kihou, Hirofumi Matsuhata, Markus Braden, and Kazuyoshi Yamada. Effect of structural parameters on superconductivity in fluorine-free $LnFeAsO_{1-y}$ (Ln=La, Nd). *Journal of the Physical Society of Japan*, 77(8):083704, 2008.

[35] H. Okabe, N. Takeshita, K. Horigane, T. Muranaka, and J. Akimitsu. Pressure-induced high-T_c superconducting phase in FeSe: Correlation between anion height and T_c. *Phys. Rev. B*, 81:205119, May 2010.

[36] Kazuhiko Kuroki, Hidetomo Usui, Seiichiro Onari, Ryotaro Arita, and Hideo Aoki. Pnictogen height as a possible switch between high-T_c nodeless and low-T_c nodal pairings in the iron-based superconductors. *Phys. Rev. B*, 79:224511, Jun 2009.

[37] Stephen D. Wilson, Z. Yamani, C. R. Rotundu, B. Freelon, E. Bourret-Courchesne, and R. J. Birgeneau. Neutron diffraction study of the magnetic and structural phase transitions in $BaFe_2As_2$. *Phys. Rev. B*, 79:184519, May 2009.

[38] Kentaro Kitagawa, Naoyuki Katayama, Kenya Ohgushi, Makoto Yoshida, and Masashi Takigawa. Commensurate itinerant antiferromagnetism in $BaFe_2As_2$: 75As-NMR studies on a self-flux grown single crystal. *Journal of the Physical Society of Japan*, 77(11):114709, 2008.

[39] C. R. Rotundu, B. Freelon, T. R. Forrest, S. D. Wilson, P. N. Valdivia, G. Pinuellas, A. Kim, J.-W. Kim, Z. Islam, E. Bourret-Courchesne, N. E. Phillips, and R. J. Birgeneau. Heat capacity study of $BaFe_2As_2$: Effects of annealing. *Phys. Rev. B*, 82:144525, Oct 2010.

[40] D. K. Pratt, W. Tian, A. Kreyssig, J. L. Zarestky, S. Nandi, N. Ni, S. L. Bud'ko, P. C. Canfield, A. I. Goldman, and R. J. McQueeney. Coexistence of competing antiferromagnetic and superconducting phases in the underdoped $Ba(Fe_{0.953}Co_{0.047})_2As_2$ compound using X-ray and Neutron scattering techniques. *Phys. Rev. Lett.*, 103:087001, Aug 2009.

[41] S. Nandi, M. G. Kim, A. Kreyssig, R. M. Fernandes, D. K. Pratt, A. Thaler, N. Ni, S. L. Bud'ko, P. C. Canfield, J. Schmalian, R. J. McQueeney, and A. I. Goldman. Anomalous suppression of the orthorhombic lattice distortion in superconducting $Ba(Fe_{1-x}Co_x)_2As_2$ single crystals. *Phys. Rev. Lett.*, 104:057006, Feb 2010.

[42] Leland W. Harriger, Astrid Schneidewind, Shiliang Li, Jun Zhao, Zhengcai Li, Wei Lu, Xiaoli Dong, Fang Zhou, Zhongxian Zhao, Jiangping Hu, and Pengcheng Dai. Transition from three-dimensional anisotropic spin excitations to two-dimensional spin excitations by electron doping the FeAs-based $BaFe_{1.96}Ni_{0.04}As_2$ superconductor. *Phys. Rev. Lett.*, 103:087005, Aug 2009.

[43] Gianluca Giovannetti, Carmine Ortix, Martijn Marsman, Massimo Capone, Jeroen Van Den Brink, and José Lorenzana. Proximity of iron pnictide superconductors to a quantum tricritical point. *Nature communications*, 2:398, 2011.

[44] C. R. Rotundu and R. J. Birgeneau. First and second-order magnetic and structural transitions in $BaFe_{2(1-x)}Co_{2x}As_2$. *Phys. Rev. B*, 84:092501, Sep 2011.

[45] Y. Su, P. Link, A. Schneidewind, Th. Wolf, P. Adelmann, Y. Xiao, M. Meven, R. Mittal, M. Rotter, D. Johrendt, Th. Brueckel, and M. Loewenhaupt. Antiferromagnetic ordering and structural phase transition in $BaFe_2As_2$ with Sn incorporated from the growth flux. *Phys. Rev. B*, 79:064504, Feb 2009.

[46] M D Lumsden and A D Christianson. Magnetism in Fe-based superconductors. *Journal of Physics: Condensed Matter*, 22(20):203203, 2010.

[47] C. Lester, Jiun-Haw Chu, J. G. Analytis, S. C. Capelli, A. S. Erickson, C. L. Condron, M. F. Toney, I. R. Fisher, and S. M. Hayden. Neutron scattering study of the interplay between structure and magnetism in $Ba(Fe_{1-x}Co_x)_2As_2$. *Phys. Rev. B*, 79:144523, Apr 2009.

[48] Norman Mannella. The magnetic moment enigma in Fe-based high temperature superconductors. *Journal of Physics: Condensed Matter*, 26(47):473202, 2014.

[49] Qimiao Si and Elihu Abrahams. Strong correlations and magnetic frustration in the high T_C iron pnictides. *Phys. Rev. Lett.*, 101:076401, Aug 2008.

[50] Qimiao Si, Elihu Abrahams, Jianhui Dai, and Jian-Xin Zhu. Correlation effects in the iron pnictides. *New Journal of Physics*, 11(4):045001, 2009.

[51] Sunil Nair, S Wirth, S Friedemann, F Steglich, Q Si, and AJ Schofield. Hall effect in heavy fermion metals. *Advances in Physics*, 61(5):583–664, 2012.

[52] Branko P. Stojković and David Pines. Anomalous Hall effect in $YBa_2Cu_3O_7$. *Phys. Rev. Lett.*, 76:811–814, Jan 1996.

[53] Branko P. Stojkovic-acute and David Pines. Theory of the longitudinal and Hall conductivities of the cuprate superconductors. *Phys. Rev. B*, 55:8576–8595, Apr 1997.

[54] Hiroshi Kontani. Anomalous transport phenomena in Fermi liquids with strong magnetic fluctuations. *Reports on Progress in Physics*, 71(2):026501, 2008.

[55] A. F. Kemper, M. M. Korshunov, T. P. Devereaux, J. N. Fry, H-P. Cheng, and P. J. Hirschfeld. Anisotropic quasiparticle lifetimes in Fe-based superconductors. *Phys. Rev. B*, 83:184516, May 2011.

[56] Seiichiro Onari and Hiroshi Kontani. Non-Fermi-liquid transport phenomena and superconductivity driven by orbital fluctuations in iron pnictides: Analysis by fluctuation-exchange approximation. *Phys. Rev. B*, 85:134507, Apr 2012.

[57] Maxim Breitkreiz, P. M. R. Brydon, and Carsten Timm. Transport in multiband systems with hot spots on the Fermi surface: Forward-scattering corrections. *Phys. Rev. B*, 89:245106, Jun 2014.

[58] P Coleman, C Pépin, Qimiao Si, and R Ramazashvili. How do Fermi liquids get heavy and die? *Journal of Physics: Condensed Matter*, 13(35):R723, 2001.

[59] M. Lee, A. Husmann, T. F. Rosenbaum, and G. Aeppli. High resolution study of magnetic ordering at absolute zero. *Phys. Rev. Lett.*, 92:187201, May 2004.

[60] Silke Paschen, Thomas Lühmann, Steffen Wirth, Philipp Gegenwart, Octavio Trovarelli, Christoph Geibel, Frank Steglich, Piers Coleman, and Qimiao Si. Hall-effect evolution across a heavy-fermion quantum critical point. *Nature*, 432(7019):881, 2004.

[61] Max Kohler. Zur magnetischen widerstandsänderung reiner metalle. *Annalen der Physik*, 424(1-2):211–218, 1938.

[62] Alfred Brian Pippard. *Magnetoresistance in metals*, volume 2. Cambridge University Press, 1989.

[63] Colin Hurd. *The Hall effect in metals and alloys.* Springer Science & Business Media, 2012.

[64] Nie Luo and GH Miley. Kohler's rule and relaxation rates in high-T_C superconductors. *Physica C: Superconductivity*, 371(4):259–269, 2002.

[65] J. M. Harris, Y. F. Yan, P. Matl, N. P. Ong, P. W. Anderson, T. Kimura, and K. Kitazawa. Violation of Kohler's rule in the normal-state magnetoresistance of $YBa_2Cu_3O_{7-\delta}$ and $La_2Sr_xCuO_4$. *Phys. Rev. Lett.*, 75:1391–1394, Aug 1995.

[66] Y Nakajima, H Shishido, H Nakai, T Shibauchi, K Behnia, K Izawa, M Hedo, Y Uwatoko, T Matsumoto, R Settai, et al. Non-Fermi liquid behavior in the magnetotransport of $CeMIn_5$ (M: Co and Rh): Striking similarity between quasi two-dimensional heavy fermion and high-T_C cuprates. *Journal of the Physical Society of Japan*, 76(2):024703, 2007.

[67] M. J. Eom, S. W. Na, C. Hoch, R. K. Kremer, and J. S. Kim. Evolution of transport properties of $BaFe_{2-x}Ru_xAs_2$ in a wide range of isovalent Ru substitution. *Phys. Rev. B*, 85:024536, Jan 2012.

[68] S. Kasahara, T. Shibauchi, K. Hashimoto, Y. Nakai, H. Ikeda, T. Terashima, and Y. Matsuda. Abrupt recovery of Fermi-liquid transport following the collapse of the *c* axis in $CaFe_2(As_{1-x}P_x)_2$ single crystals. *Phys. Rev. B*, 83:060505, Feb 2011.

[69] Yue Sun, Toshihiro Taen, Tatsuhiro Yamada, Sunseng Pyon, Terukazu Nishizaki, Zhixiang Shi, and Tsuyoshi Tamegai. Multiband effects and possible Dirac fermions in $Fe_{1+y}Te_{0.6}Se_{0.4}$. *Phys. Rev. B*, 89:144512, Apr 2014.

[70] L. M. Wang, Un-Cheong Sou, H. C. Yang, L. J. Chang, Cheng-Maw Cheng, Ku-Ding Tsuei, Y. Su, Th. Wolf, and P. Adelmann. Mixed-state Hall effect and flux pinning in $Ba(Fe_{1-x}Co_x)_2As_2$ single crystals (x= 0. 08 and 0. 10). *Phys. Rev. B*, 83:134506, Apr 2011.

[71] Peng Cheng, Huan Yang, Ying Jia, Lei Fang, Xiyu Zhu, Gang Mu, and Hai-Hu Wen. Hall effect and magnetoresistance in single crystals of $NdFeAsO_{1-x}F_x$ ($x = 0$ and 0.18). *Phys. Rev. B*, 78:134508, Oct 2008.

[72] Y. Nakajima, H. Shishido, H. Nakai, T. Shibauchi, M. Hedo, Y. Uwatoko, T. Matsumoto, R. Settai, Y. Onuki, H. Kontani, and Y. Matsuda. Magnetotransport properties governed by antiferromagnetic fluctuations in the heavy-fermion superconductor $CeIrIn_5$. *Phys. Rev. B*, 77:214504, Jun 2008.

[73] Y. Nakajima, K. Izawa, Y. Matsuda, S. Uji, T. Terashima, H. Shishido, R. Settai, Y. Onuki, and H. Kontani. Normal-state Hall angle and magnetoresistance in quasi-2D heavy fermion $CeCoIn_5$ near a quantum critical point. *Journal of the Physical Society of Japan*, 73(1):5–8, 2004.

[74] Koichi Izawa, Y. Nakajima, Y. Kasahara, R. Bel, K. Behnia, H. Shishido, R. Settai, Y. Onuki, H. Kontani, and Y. Matsuda. Striking similarities between HTSC and quasi-2D HF $CeRIn_5$. *Physica C: Superconductivity and its Applications*, 460-462:145 – 148, 2007. Proceedings of the 8th International Conference on Materials and Mechanisms of Superconductivity and High Temperature Superconductors.

[75] Daniel Gnida, Marcin Matusiak, and Dariusz Kaczorowski. Anomalous magnetotransport in the heavy-fermion superconductor Ce_2PdIn_8. *Phys. Rev. B*, 85:060508, Feb 2012.

[76] P. W. Anderson. Hall effect in the two-dimensional Luttinger liquid. *Phys. Rev. Lett.*, 67:2092–2094, Oct 1991.

[77] P Coleman, A J Schofield, and A M Tsvelik. How should we interpret the two transport relaxation times in the cuprates? *Journal of Physics: Condensed Matter*, 8(48):9985, 1996.

[78] Yoichi Ando, Y. Kurita, Seiki Komiya, S. Ono, and Kouji Segawa. Evolution of the Hall coefficient and the peculiar electronic structure of the cuprate superconductors. *Phys. Rev. Lett.*, 92:197001, May 2004.

[79] S. Ono, Seiki Komiya, and Yoichi Ando. Strong charge fluctuations manifested in the high-temperature Hall coefficient of high-T_c cuprates. *Phys. Rev. B*, 75:024515, Jan 2007.

[80] M. F. Hundley, A. Malinowski, P. G. Pagliuso, J. L. Sarrao, and J. D. Thompson. Anomalous f-electron Hall effect in the heavy-fermion system $CeTIn_5$ (T = Co, Ir, or, Rh). *Phys. Rev. B*, 70:035113, Jul 2004.

[81] Yu.V. Sushko, N. Shirakawa, K. Murata, Y. Kubo, N.D. Kushch, and E.B. Yagubskii. Temperature-dependent Hall effect of $-(BEDT-TTF)_2Cu[N(CN)_2]Cl$ under pressure. *Synthetic Metals*, 85(1):1541 – 1542, 1997.

[82] J.A. Clayhold, Z.H. Zhang, and A.J. Schofield. Two lifetimes without a magnetic field in the normal state of cuprate superconductors. *Journal of Physics and Chemistry of Solids*, 59(10):2114 – 2117, 1998.

[83] J. A. Clayhold, A. W. Linnen, F. Chen, and C. W. Chu. Normal-state Nernst effect in a $Tl_2Ba_2CaCu_2O_{8+\delta}$ epitaxial film. *Phys. Rev. B*, 50:4252–4255, Aug 1994.

[84] S. Kasahara, T. Shibauchi, K. Hashimoto, K. Ikada, S. Tonegawa, R. Okazaki, H. Shishido, H. Ikeda, H. Takeya, K. Hirata, T. Terashima, and Y. Matsuda. Evolution from non-Fermi- to Fermi-liquid transport via isovalent doping in $BaFe_2(As_{1-x}P_x)_2$ superconductors. *Phys. Rev. B*, 81:184519, May 2010.

[85] T. F. Rosenbaum, A. Husmann, S. A. Carter, and J. M. Honig. Temperature dependence of the Hall angle in a correlated three-dimensional metal. *Phys. Rev. B*, 57:R13997–R13999, Jun 1998.

[86] Evgeny Mikheev, Christopher R. Freeze, Brandon J. Isaac, Tyler A. Cain, and Susanne Stemmer. Separation of transport lifetimes in $SrTiO_3$-based two-dimensional electron liquids. *Phys. Rev. B*, 91:165125, Apr 2015.

[87] Susanne Stemmer and S James Allen. Non-Fermi liquids in oxide heterostructures. *Reports on Progress in Physics*, 81(6):062502, 2018.

[88] Patrick B Marshall, Honggyu Kim, and Susanne Stemmer. Disorder versus two transport lifetimes in a strongly correlated electron liquid. *Scientific reports*, 7(1):10312, 2017.

[89] Y. A. Ying, Y. Liu, T. He, and R. J. Cava. Magnetotransport properties of $BaRuO_3$: Observation of two scattering rates. *Phys. Rev. B*, 84:233104, Dec 2011.

[90] M. S. Laad, I. Bradarić, and F. V. Kusmartsev. Orbital non-Fermi-liquid behavior in cubic ruthenates. *Phys. Rev. Lett.*, 100:096402, Mar 2008.

[91] A. Carrington, A. P. Mackenzie, C. T. Lin, and J. R. Cooper. Temperature dependence of the Hall angle in single-crystal $YBa_2(Cu_{1-x}Co_x)_3O_{7-\delta}$. *Phys. Rev. Lett.*, 69:2855–2858, Nov 1992.

[92] R. Hlubina and T. M. Rice. Resistivity as a function of temperature for models with hot spots on the Fermi surface. *Phys. Rev. B*, 51:9253–9260, Apr 1995.

[93] Branko P. Stojković and David Pines. Anomalous Hall effect in $YBa_2Cu_3O_7$. *Phys. Rev. Lett.*, 76:811–814, Jan 1996.

[94] Hiroshi Kontani, Kazuki Kanki, and Kazuo Ueda. Hall effect and resistivity in high-T_c superconductors: The conserving approximation. *Phys. Rev. B*, 59:14723–14739, Jun 1999.

[95] Hiroshi Kontani. Magnetoresistance in high-T_C superconductors: The role of vertex corrections. *Journal of the Physical Society of Japan*, 70(7):1873–1876, 2001.

[96] Hiroshi Kontani. Theory of magnetoresistance in correlated electron systems: modified Kohler rule in high-T_C superconductors. *Physica B: Condensed Matter*, 312:25–27, 2002.

[97] Hiroshi Kontani. Optical conductivity and Hall coefficient in high-T_C superconductors: Significant role of current vertex corrections. *Journal of the Physical Society of Japan*, 75(1):013703–013703, 2006.

[98] Hiroshi Kontani. *Transport phenomena in strongly correlated Fermi liquids*, volume 251. Springer, 2013.

[99] M. Shi, A. Bendounan, E. Razzoli, S. Rosenkranz, M. R. Norman, J. C. Campuzano, J. Chang, M. Mnsson, Y. Sassa, T. Claesson, O. Tjernberg, L. Patthey, N. Momono, M. Oda, M. Ido, S. Guerrero, C. Mudry, and J. Mesot. Spectroscopic evidence for preformed Cooper pairs in the pseudogap phase of cuprates. *EPL (Europhysics Letters)*, 88(2):27008, 2009.

[100] Jhinhwan Lee, K. Fujita, A. R. Schmidt, Chung Koo Kim, H. Eisaki, S. Uchida, and J. C. Davis. Spectroscopic fingerprint of phase-incoherent superconductivity in the underdoped $Bi_2Sr_2CaCu_2O_{8+\delta}$. *Science*, 325(5944):1099–1103, 2009.

[101] M. A. Surmach, F. Brückner, S. Kamusella, R. Sarkar, P. Y. Portnichenko, J. T. Park, G. Ghambashidze, H. Luetkens, P. K. Biswas, W. J. Choi, Y. I. Seo, Y. S. Kwon, H.-H. Klauss, and D. S. Inosov. Superconducting properties and pseudogap from preformed Cooper pairs in the triclinic $(CaFe_{1-x}Pt_xAs)_{10}pt_3as_8$. *Phys. Rev. B*, 91:104515, Mar 2015.

[102] Tom Timusk and Bryan Statt. The pseudogap in high-temperature superconductors: an experimental survey. *Reports on Progress in Physics*, 62(1):61, 1999.

[103] R. Khasanov, Takeshi Kondo, S. Strässle, D. O. G. Heron, A. Kaminski, H. Keller, S. L. Lee, and Tsunehiro Takeuchi. Evidence for a competition between the superconducting state and the pseudogap state of $(BiPb)_2(SrLa)_2CuO_{6+\delta}$ from muon spin rotation experiments. *Phys. Rev. Lett.*, 101:227002, Nov 2008.

[104] Takeshi Kondo, Rustem Khasanov, Tsunehiro Takeuchi, Jörg Schmalian, and Adam Kaminski. Competition between the pseudogap and superconductivity in the high-T_C copper oxides. *Nature*, 457(7227):296, 2009.

[105] A F Wang, J J Ying, X G Luo, Y J Yan, D Y Liu, Z J Xiang, P Cheng, G J Ye, L J Zou, Z Sun, and X H Chen. A crossover in the phase diagram of $NaFe_{1-x}Co_xAs$ determined by electronic transport measurements. *New Journal of Physics*, 15(4):043048, 2013.

[106] R. H. Liu, G. Wu, T. Wu, D. F. Fang, H. Chen, S. Y. Li, K. Liu, Y. L. Xie, X. F. Wang, R. L. Yang, L. Ding, C. He, D. L. Feng, and X. H. Chen. Anomalous transport properties and phase diagram of the FeAs-based $SmFeAsO_{1-x}F_x$ superconductors. *Phys. Rev. Lett.*, 101:087001, Aug 2008.

[107] C. Hess, A. Kondrat, A. Narduzzo, J. E. Hamann-Borrero, R. Klingeler, J. Werner, G. Behr, and B. Büchner. The intrinsic electronic phase diagram of iron-oxypnictide superconductors. *Europhysics Letters*, 87(1):17005, 2009.

[108] Rohit Kumar, Surjeet Singh, and Sunil Nair. Scaling of magnetotransport in the $Ba(Fe_{1-x}Co_x)_2As_2$ series. *Journal of Physics: Condensed Matter*, 31(11):115601, 2019.

[109] S. J. Moon, A. A. Schafgans, S. Kasahara, T. Shibauchi, T. Terashima, Y. Matsuda, M. A. Tanatar, R. Prozorov, A. Thaler, P. C. Canfield, A. S. Sefat, D. Mandrus, and D. N. Basov. Infrared measurement of the pseudogap of P-doped and Co-doped high-temperature $BaFe_2As_2$ superconductors. *Phys. Rev. Lett.*, 109:027006, Jul 2012.

[110] Yong Seung Kwon, Jong Beom Hong, Yu Ran Jang, Hyun Jin Oh, Yun Young Song, Byeong Hun Min, Takeuya Iizuka, Shin ichi Kimura, A V Balatsky, and Yunkyu Bang. Evidence of a pseudogap for superconducting iron-pnictide $Ba_{0.6+}K_{0.4}Fe_2As_2$ single crystals from optical conductivity measurements. *New Journal of Physics*, 14(6):063009, 2012.

[111] Fanlong Ning, Kanagasingham Ahilan, Takashi Imai, Athena S Sefat, Ronying Jin, Michael A McGuire, Brian C Sales, and David Mandrus. ^{59}Co and ^{75}As NMR investigation of electron-doped high T_C superconductor $BaFe_{1.8}Co_{0.2}As_2$ (T_C=22 K). *Journal of the Physical Society of Japan*, 77(10):103705–103705, 2008.

[112] S.-H. Baek, H.-J. Grafe, L. Harnagea, S. Singh, S. Wurmehl, and B. Büchner. Pseudogap-like phase in $Ca(Fe_{1-x}Co_x)_2As_2$ revealed by ^{75}As NQR. *Phys. Rev. B*, 84:094510, Sep 2011.

[113] I. Pallecchi, M. Tropeano, C. Ferdeghini, G. Lamura, A. Martinelli, A. Palenzona, and M. Putti. Pseudogap analysis of normal state transport behavior of 11 and 1111 Fe-based superconductors. *Journal of Superconductivity and Novel Magnetism*, 24(5):1751–1760, Jul 2011.

[114] R. Klingeler, N. Leps, I. Hellmann, A. Popa, U. Stockert, C. Hess, V. Kataev, H.-J. Grafe, F. Hammerath, G. Lang, S. Wurmehl, G. Behr, L. Harnagea, S. Singh, and B. Büchner. Local antiferromagnetic correlations in the iron pnictide superconductors $LaFeAsO_{1-x}F_x$ and $Ca(Fe_{1-x}Co_x)_2As_2$ as seen via normal-state susceptibility. *Phys. Rev. B*, 81:024506, Jan 2010.

[115] T. Shimojima, T. Sonobe, W. Malaeb, K. Shinada, A. Chainani, S. Shin, T. Yoshida, S. Ideta, A. Fujimori, H. Kumigashira, K. Ono, Y. Nakashima, H. Anzai, M. Arita, A. Ino, H. Namatame, M. Taniguchi, M. Nakajima, S. Uchida, Y. Tomioka, T. Ito, K. Kihou,

C. H. Lee, A. Iyo, H. Eisaki, K. Ohgushi, S. Kasahara, T. Terashima, H. Ikeda, T. Shibauchi, Y. Matsuda, and K. Ishizaka. Pseudogap formation above the superconducting dome in iron pnictides. *Phys. Rev. B*, 89:045101, Jan 2014.

[116] Takafumi Sato, Seigo Souma, Kosuke Nakayama, Kensei Terashima, Katsuaki Sugawara, Takashi Takahashi, Yoichi Kamihara, Masahiro Hirano, and Hideo Hosono. Superconducting gap and pseudogap in iron-based layered superconductor $La(O_{1-x}F_x)FeAS$. *Journal of the Physical Society of Japan*, 77(6):063708, 2008.

[117] Y-M Xu, P Richard, K Nakayama, T Kawahara, Y Sekiba, T Qian, M Neupane, S Souma, T Sato, T Takahashi, et al. Fermi surface dichotomy of the superconducting gap and pseudogap in underdoped pnictides. *Nature communications*, 2:394, 2011.

[118] Marcin Matusiak and Thomas Wolf. Violation of the Wiedemann-Franz law as evidence of the pseudogap in the iron-based superconductor $Ba(Fe_{1-x}Co_x)_2As_2$. *Phys. Rev. B*, 92:020507, Jul 2015.

[119] A. Malinowski, Marta Z. Cieplak, S. Guha, Q. Wu, B. Kim, A. Krickser, A. Perali, K. Karpińska, M. Berkowski, C. H. Shang, and P. Lindenfeld. Magnetotransport in the normal state of $La_{1.85}Sr_{0.15}Cu_{1-y}Zn_yO_4$ films. *Phys. Rev. B*, 66:104512, Sep 2002.

[120] Z. Konstantinović, Z. Z. Li, and H. Raffy. Temperature dependence of the Hall effect in single-layer and bilayer $Bi_2Sr_2Ca_{n-1}Cu_nO_y$ thin films at various oxygen contents. *Phys. Rev. B*, 62:R11989–R11992, Nov 2000.

[121] Yasushi Abe, Kouji Segawa, and Yoichi Ando. Hall effect in Zn-doped $YBa_2Cu_3O_{7-\delta}$ revisited: Hall angle and the pseudogap. *Phys. Rev. B*, 60:R15055–R15058, Dec 1999.

[122] Yoichi Ando, T. Murayama, and S. Ono. Systematic evolution of the magnetotransport properties of $Bi_2Sr_{2-x}La_xCuO_6$ with carrier concentration. *Journal of Low Temperature Physics*, 117(5):1117–1121, Dec 1999.

[123] ZA Xu, Y Zhang, and NP Ong. Effect of the pseudogap on the Hall conductivity in underdoped $YBa_2Cu_3O_{6+x}$. *arXiv preprint cond-mat/9903123*, 1999.

[124] F. F. Balakirev, I. E. Trofimov, S. Guha, Marta Z. Cieplak, and P. Lindenfeld. Orbital magnetoresistance in the $La_{2-x}Sr_xCuO_4$ system. *Phys. Rev. B*, 57:R8083–R8086, Apr 1998.

[125] I. Pallecchi, F. Bernardini, M. Tropeano, A. Palenzona, A. Martinelli, C. Ferdeghini, M. Vignolo, S. Massidda, and M. Putti. Magnetotransport in La(Fe,Ru)AsO as a probe of band structure and mobility. *Phys. Rev. B*, 84:134524, Oct 2011.

[126] Hsueh-Hui Kuo, Jiun-Haw Chu, Scott C. Riggs, Leo Yu, Peter L. McMahon, Kristiaan De Greve, Yoshihisa Yamamoto, James G. Analytis, and Ian R. Fisher. Possible origin of the nonmonotonic doping dependence of the in-plane resistivity anisotropy of $Ba(Fe_{1-x}T_x)_2As_2$ (T= Co, Ni and Cu). *Phys. Rev. B*, 84:054540, Aug 2011.

[127] SV Chong, GVM Williams, J Kennedy, F Fang, JL Tallon, and K Kadowaki. Large low-temperature magnetoresistance in $SrFe_2As_2$ single crystals. *EPL (Europhysics Letters)*, 104(1):17002, 2013.

[128] D Bhoi, P Mandal, Pranab Choudhury, S Pandya, and V Ganesan. Quantum magnetoresistance of the PrFeAsO oxypnictide. *Applied Physics Letters*, 98(17):172105, 2011.

[129] D. A. Moseley, K. A. Yates, N. Peng, D. Mandrus, A. S. Sefat, W. R. Branford, and L. F. Cohen. Magnetotransport of proton-irradiated $BaFe_2As_2$ and $BaFe_{1.985}Co_{0.015}As_2$ single crystals. *Phys. Rev. B*, 91:054512, Feb 2015.

[130] S. Ishida, T. Liang, M. Nakajima, K. Kihou, C. H. Lee, A. Iyo, H. Eisaki, T. Kakeshita, T. Kida, M. Hagiwara, Y. Tomioka, T. Ito, and S. Uchida. Manifestations of multiple-carrier charge transport in the magnetostructurally ordered phase of $BaFe_2As_2$. *Phys. Rev. B*, 84:184514, Nov 2011.

[131] Y. Tanabe, K. K. Huynh, S. Heguri, G. Mu, T. Urata, J. Xu, R. Nouchi, N. Mitoma, and K. Tanigaki. Coexistence of Dirac-cone states and superconductivity in iron pnictide $Ba(Fe_{1-x}Ru_xAs)_2$. *Phys. Rev. B*, 84:100508, Sep 2011.

[132] Khuong K. Huynh, Yoichi Tanabe, and Katsumi Tanigaki. Both electron and hole Dirac cone states in $Ba(FeAs)_2$ confirmed by magnetoresistance. *Phys. Rev. Lett.*, 106:217004, May 2011.

[133] I. Pallecchi, F. Bernardini, F. Caglieris, A. Palenzona, S. Massidda, and M. Putti. Role of Dirac cones in magnetotransport properties of REFeAsO (RE = rare earth) oxypnictides. *The European Physical Journal B*, 86(8):338, Aug 2013.

[134] R. S. Meena, Shiva Kumar Singh, Anand Pal, Anuj Kumar, R. Jha, K. V. R. Rao, Y. Du, X. L. Wang, and V. P. S Awana. High field (14 T) magneto transport of Sm/PrFeAsO. *Journal of Applied Physics*, 111(7):07E323, 2012.

[135] T. Urata, Y. Tanabe, K. K. Huynh, H. Oguro, K. Watanabe, S. Heguri, and K. Tanigaki. Kondo-like mass enhancement of Dirac fermions in $Ba(Fe_{1-x}Mn_xAs)_2$. *Phys. Rev. B*, 89:024503, Jan 2014.

[136] Yue Sun, Sunseng Pyon, and Tsuyoshi Tamegai. Electron carriers with possible Dirac-cone-like dispersion in $FeSe_{1-x}S_x$ (x = 0 and 0.14) single crystals triggered by structural transition. *Phys. Rev. B*, 93:104502, Mar 2016.

[137] Z. P. Yin, K. Haule, and G. Kotliar. Magnetism and charge dynamics in iron pnictides. *Nature Physics*, 7:294–297, 2011.

[138] Takao Morinari, Eiji Kaneshita, and Takami Tohyama. Topological and transport properties of Dirac fermions in an antiferromagnetic metallic phase of iron-based superconductors. *Phys. Rev. Lett.*, 105:037203, Jul 2010.

[139] Ying Ran, Fa Wang, Hui Zhai, Ashvin Vishwanath, and Dung-Hai Lee. Nodal spin density wave and band topology of the FeAs-based materials. *Phys. Rev. B*, 79:014505, Jan 2009.

[140] P. Richard, K. Nakayama, T. Sato, M. Neupane, Y.-M. Xu, J. H. Bowen, G. F. Chen, J. L. Luo, N. L. Wang, X. Dai, Z. Fang, H. Ding, and T. Takahashi. Observation of Dirac cone electronic dispersion in $BaFe_2As_2$. *Phys. Rev. Lett.*, 104:137001, Mar 2010.

[141] Mike Sutherland, D. J. Hills, B. S. Tan, M. M. Altarawneh, N. Harrison, J. Gillett, E. C. T. O'Farrell, T. M. Benseman, I. Kokanovic, P. Syers, J. R. Cooper, and Suchitra E. Sebastian. Evidence for Dirac nodes from quantum oscillations in $SrFe_2As_2$. *Phys. Rev. B*, 84:180506, Nov 2011.

[142] Taichi Terashima, Hishiro T. Hirose, David Graf, Yonghui Ma, Gang Mu, Tao Hu, Katsuhiro Suzuki, Shinya Uji, and Hiroaki Ikeda. Fermi

surface with Dirac fermions in CaFeAsF determined via quantum oscillation measurements. *Phys. Rev. X*, 8:011014, Feb 2018.

[143] N. Harrison and S. E. Sebastian. Dirac nodal pockets in the antiferromagnetic parent phase of feas superconductors. *Phys. Rev. B*, 80:224512, Dec 2009.

[144] James G. Analytis, Ross D. McDonald, Jiun-Haw Chu, Scott C. Riggs, Alimamy F. Bangura, Chris Kucharczyk, Michelle Johannes, and I. R. Fisher. Quantum oscillations in the parent pnictide $BaFe_2As_2$: Itinerant electrons in the reconstructed state. *Phys. Rev. B*, 80:064507, Aug 2009.

[145] Suchitra E Sebastian, J Gillett, N Harrison, PHC Lau, David J Singh, CH Mielke, and GG Lonzarich. Quantum oscillations in the parent magnetic phase of an iron arsenide high temperature superconductor. *Journal of Physics: Condensed Matter*, 20(42):422203, 2008.

[146] A Carrington. Quantum oscillation studies of the Fermi surface of iron-pnictide superconductors. *Reports on Progress in Physics*, 74(12):124507, 2011.

[147] K K Huynh, Y Tanabe, T Urata, S Heguri, K Tanigaki, T Kida, and M Hagiwara. Mobility spectrum analytical approach for intrinsic band picture of $Ba(FeAs)_2$. *New Journal of Physics*, 16(9):093062, 2014.

[148] Yoshinori Imai, Fuyuki Nabeshima, Daisuke Nakamura, Takayoshi Katase, Hidenori Hiramatsu, Hideo Hosono, and Atsutaka Maeda. Ultralow-dissipative conductivity by Dirac fermions in $BaFe_2As_2$. *Journal of the Physical Society of Japan*, 82(4):043709, 2013.

[149] Zhi-Guo Chen, Luyang Wang, Yu Song, Xingye Lu, Huiqian Luo, Chenglin Zhang, Pengcheng Dai, Zhiping Yin, Kristjan Haule, and Gabriel Kotliar. Two-dimensional massless Dirac fermions in antiferromagnetic AFe_2As_2 (A = Ba, Sr). *Phys. Rev. Lett.*, 119:096401, Aug 2017.

[150] Y. Tanabe, K. K. Huynh, T. Urata, S. Heguri, G. Mu, J. T. Xu, R. Nouchi, and K. Tanigaki. Suppression of backward scattering of Dirac fermions in iron pnictides $Ba(Fe_{1-x}Ru_xAs)_2$. *Phys. Rev. B*, 86:094510, Sep 2012.

[151] Marcin Matusiak, Zbigniew Bukowski, and Janusz Karpinski. Doping dependence of the Nernst effect in $Eu(Fe_{1-x}Co_x)_2As_2$: Departure from Dirac-fermion physics. *Phys. Rev. B*, 83:224505, Jun 2011.

[152] T. Urata, Y. Tanabe, K. K. Huynh, S. Heguri, H. Oguro, K. Watanabe, and K. Tanigaki. Emergence of high-mobility minority holes in the electrical transport of the $Ba(Fe_{1-x}Mn_xAs)_2$ iron pnictides. *Phys. Rev. B*, 91:174508, May 2015.

[153] M. Lee, T. F. Rosenbaum, M.-L. Saboungi, and H. S. Schnyders. Band-gap tuning and linear magnetoresistance in the silver chalcogenides. *Phys. Rev. Lett.*, 88:066602, Jan 2002.

[154] Gang Mu, Qiucheng Ji, Wei Li, Xuguang Xu, Tao Hu, Da Jiang, Zhi Wang, Bo Gao, Xiaoming Xie, and Mianheng Jiang. Quantum magnetoresistance in the Ca-intercalated graphite superconductor CaC_6. *Phys. Rev. B*, 90:214522, Dec 2014.

[155] Adam L. Friedman, Joseph L. Tedesco, Paul M. Campbell, James C. Culbertson, Edward Aifer, F. Keith Perkins, Rachael L. Myers-Ward, Jennifer K. Hite, Charles R. Eddy, Glenn G. Jernigan, and D. Kurt Gaskill. Quantum linear magnetoresistance in multilayer epitaxial graphene. *Nano Letters*, 10(10):3962–3965, 2010. PMID: 20804213.

[156] AA Abrikosov. Galvanomagnetic phenomena in metals in the quantum limit. *Sov. Phys. JETP*, 29:476, 1969.

[157] A. A. Abrikosov. Quantum magnetoresistance. *Phys. Rev. B*, 58:2788–2794, Aug 1998.

[158] AA Abrikosov. Quantum linear magnetoresistance. *EPL (Europhysics Letters)*, 49(6):789, 2000.

[159] AA Abrikosov. Quantum linear magnetoresistance; solution of an old mystery. *Journal of Physics A: Mathematical and General*, 36(35):9119, 2003.

[160] A. A. Abrikosov. Quantum magnetoresistance of layered semimetals. *Phys. Rev. B*, 60:4231–4234, Aug 1999.

[161] T. F. Rosenbaum M.-L. Saboungi J. E. Enderby R. Xu, A. Husmann and P. B. Littlewood. Large magnetoresistance in non-magnetic silver chalcogenides. *Nature*, 390:57–60, 1997.

[162] S. L. Bud'ko, P. C. Canfield, C. H. Mielke, and A. H. Lacerda. Anisotropic magnetic properties of light rare-earth diantimonides. *Phys. Rev. B*, 57:13624–13638, Jun 1998.

[163] J. C. Slonczewski and P. R. Weiss. Band structure of graphite. *Phys. Rev.*, 109:272–279, Jan 1958.

[164] N Harrison, R D McDonald, C H Mielke, E D Bauer, F Ronning, and J D Thompson. Quantum oscillations in antiferromagnetic $CaFe_2As_2$ on the brink of superconductivity. *Journal of Physics: Condensed Matter*, 21(32):322202, 2009.

[165] Amalia I. Coldea. Quantum oscillations probe the normal electronic states of novel superconductors. *Philosophical Transactions of the Royal Society of London A: Mathematical, Physical and Engineering Sciences*, 368(1924):3503–3517, 2010.

[166] N. Ni, S. L. Bud'ko, A. Kreyssig, S. Nandi, G. E. Rustan, A. I. Goldman, S. Gupta, J. D. Corbett, A. Kracher, and P. C. Canfield. Anisotropic thermodynamic and transport properties of single-crystalline $Ba_{1-x}K_xFe_2As_2$ (x=0 and 0.45). *Phys. Rev. B*, 78:014507, Jul 2008.

[167] H-S Lee, J-H Park, J-Y Lee, J-Y Kim, N-H Sung, T-Y Koo, B K Cho, C-U Jung, S Saini, S-J Kim, and H-J Lee. High-pressure growth of fluorine-free $SmFeAsO_{1-x}$ superconducting single crystals. *Superconductor Science and Technology*, 22(7):075023, 2009.

[168] Zhi-An Ren, Guang-Can Che, Xiao-Li Dong, Jie Yang, Wei Lu, Wei Yi, Xiao-Li Shen, Zheng-Cai Li, Li-Ling Sun, Fang Zhou, and Zhong-Xian Zhao. Superconductivity and phase diagram in iron-based arsenic-oxides $ReFeAsO_{1-\delta}$ (Re = rare-earth metal) without fluorine doping. *EPL (Europhysics Letters)*, 83(1):17002, 2008.

[169] N D Zhigadlo, S Katrych, Z Bukowski, S Weyeneth, R Puzniak, and J Karpinski. Single crystals of superconducting $SmFeAsO_{1-x}F_y$ grown at high pressure. *Journal of Physics: Condensed Matter*, 20(34):342202, 2008.

[170] G. L. Sun, D. L. Sun, M. Konuma, P. Popovich, A. Boris, J. B. Peng, K.-Y. Choi, P. Lemmens, and C. T. Lin. Single crystal growth and effect of doping on structural, transport and magnetic properties of $A_{1-x}K_xFe_2As_2$(A=Ba,Sr). *Journal of Superconductivity and Novel Magnetism*, 24(5):1773–1785, Jul 2011.

[171] Z. Bukowski, S. Weyeneth, R. Puzniak, P. Moll, S. Katrych, N. D. Zhigadlo, J. Karpinski, H. Keller, and B. Batlogg. Superconductivity

at 23 K and low anisotropy in Rb-substituted $BaFe_2As_2$ single crystals. *Phys. Rev. B*, 79:104521, Mar 2009.

[172] SB Zhang, YP Sun, XD Zhu, XB Zhu, BS Wang, G Li, HC Lei, X Luo, ZR Yang, WH Song, et al. Crystal growth and superconductivity of $FeSe_x$. *Superconductor Science and Technology*, 22(1):015020, 2008.

[173] MW Ma, DN Yuan, Y Wu, XL Dong, and F Zhou. Crystal growth of iron-based superconductor $FeSe_{0.94}$ by KCl flux method. *Physica C: Superconductivity and its Applications*, 506:154–157, 2014.

[174] J.-Q. Yan, S. Nandi, J. L. Zarestky, W. Tian, A. Kreyssig, B. Jensen, A. Kracher, K. W. Dennis, R. J. McQueeney, A. I. Goldman, R. W. McCallum, and T. A. Lograsso. Flux growth at ambient pressure of millimeter-sized single crystals of LaFeAsO, $LaFeAsO_{1-x}F_x$, and $LaFe_{1-x}Co_xAsO$. *Applied Physics Letters*, 95(22):222504, 2009.

[175] Chris Eckberg, Limin Wang, Halyna Hodovanets, Hyunsoo Kim, Daniel J. Campbell, Peter Zavalij, Philip Piccoli, and Johnpierre Paglione. Evolution of structure and superconductivity in $Ba(Ni_{1-x}Co_x)_2As_2$. *Phys. Rev. B*, 97:224505, Jun 2018.

[176] Athena S Sefat. Bulk synthesis of iron-based superconductors. *Current Opinion in Solid State and Materials Science*, 17(2):59–64, 2013.

[177] DP Chen and CT Lin. The growth of 122 and 11 iron-based superconductor single crystals and the influence of doping. *Superconductor Science and Technology*, 27(10):103002, 2014.

[178] S Aswartham, C Nacke, G Friemel, N Leps, S Wurmehl, N Wizent, C Hess, R Klingeler, G Behr, S Singh, et al. Single crystal growth and physical properties of superconducting ferro-pnictides $Ba(Fe,Co)_2As_2$ grown using self-flux and bridgman techniques. *Journal of Crystal Growth*, 314(1):341–348, 2011.

[179] Wikipedia contributors. Arsenic — Wikipedia, the free encyclopedia. 2018. [Online; accessed 15-December-2018].

[180] Thadeus B Massalski, H Okamoto, PR Subramanian, and Linda Kacprzak. Binary alloy phase diagrams (ASM International, Materials Park, Ohio, 1990). *Google Scholar*, page 3503, 1991.

[181] Juan Rodríguez-Carvajal. An introduction to the program. *FULLPROF Laboratoire Leon Brillouin, 2001, 35*, 2001.

[182] DL Sun, JZ Xiao, and CT Lin. Growth and annealing effect of Co-doped $BaFe_2As_2$ single crystals. *Journal of Crystal Growth*, 321(1):55–59, 2011.

[183] XF Wang, T Wu, G Wu, RH Liu, H Chen, YL Xie, and XH Chen. The peculiar physical properties and phase diagram of $BaFe_{2-x}Co_xAs_2$ single crystals. *New Journal of Physics*, 11(4):045003, 2009.

[184] Athena S Sefat, David J Singh, Rongying Jin, Michael A McGuire, Brian C Sales, Filip Ronning, and David Mandrus. BaT_2As_2 single crystals (T= Fe, Co, Ni) and superconductivity upon Co-doping. *Physica C: Superconductivity*, 469(9-12):350–354, 2009.

[185] Quantum Design. *Magnetic Property Measurement System: Reciprocating Sample Option Users Manual, Part number:1090-100C.*

[186] Fundamentals of Magnetism and Magnetic Materisls. Retrieved From. 1994.

[187] Magnetic Property Measurement System MPMS-XL. Retrieved From. 2011.

[188] Jiun-Haw Chu, James G. Analytis, Chris Kucharczyk, and Ian R. Fisher. Determination of the phase diagram of the electron-doped superconductor $Ba(Fe_{1-x}Co_x)_2As_2$. *Phys. Rev. B*, 79:014506, Jan 2009.

[189] P. C. Canfield, S. L. Bud'ko, Ni Ni, J. Q. Yan, and A. Kracher. Decoupling of the superconducting and magnetic/structural phase transitions in electron-doped $BaFe_2As_2$. *Phys. Rev. B*, 80:060501, Aug 2009.

[190] S. R. Saha, N. P. Butch, K. Kirshenbaum, and Johnpierre Paglione. Evolution of bulk superconductivity in $SrFe_2As_2$ with Ni substitution. *Phys. Rev. B*, 79:224519, Jun 2009.

[191] N. Ni, A. Thaler, J. Q. Yan, A. Kracher, E. Colombier, S. L. Bud'ko, P. C. Canfield, and S. T. Hannahs. Temperature versus doping phase diagrams for $Ba(Fe_{1-x}Tm_x)_2As_2$ (Tm = Ni, Cu, Cu/Co) single crystals. *Phys. Rev. B*, 82:024519, Jul 2010.

[192] Rongwei Hu, Sergey L. Bud'ko, Warren E. Straszheim, and Paul C. Canfield. Phase diagram of superconductivity and antiferromagnetism in single crystals of $Sr(Fe_{1-x}Co_x)_2As_2$ and $Sr_{1-y}Eu_y(Fe_{0.088}Co_{0.12})_2As_2$. *Phys. Rev. B*, 83:094520, Mar 2011.

[193] S. Ran, S. L. Bud'ko, W. E. Straszheim, J. Soh, M. G. Kim, A. Kreyssig, A. I. Goldman, and P. C. Canfield. Control of magnetic, nonmagnetic, and superconducting states in annealed $Ca(Fe_{1-x}Co_x)_2As_2$. *Phys. Rev. B*, 85:224528, Jun 2012.

[194] M. A. Tanatar, N. Ni, C. Martin, R. T. Gordon, H. Kim, V. G. Kogan, G. D. Samolyuk, S. L. Bud'ko, P. C. Canfield, and R. Prozorov. Anisotropy of the iron pnictide superconductor $Ba(Fe_{1-x}Co_x)_2As_2$ ($x = 0.074$, $T_c = 23$ K). *Phys. Rev. B*, 79:094507, Mar 2009.

[195] Quantum Design. *Physical Property Measurement System: Heat Capacity Option Users Manual, Part number:1085-150, M0.*

[196] JC Lashley, MF Hundley, A Migliori, JL Sarrao, PG Pagliuso, TW Darling, M Jaime, JC Cooley, WL Hults, L Morales, et al. Critical examination of heat capacity measurements made on a quantum design physical property measurement system. *Cryogenics*, 43(6):369–378, 2003.

[197] Jih Shang Hwang, Kai Jan Lin, and Cheng Tien. Measurement of heat capacity by fitting the whole temperature response of a heat-pulse calorimeter. *Review of Scientific Instruments*, 68(1):94–101, 1997.

[198] N. Ni, M. E. Tillman, J.-Q. Yan, A. Kracher, S. T. Hannahs, S. L. Bud'ko, and P. C. Canfield. Effects of Co substitution on thermodynamic and transport properties and anisotropic Hc_2 in $Ba(Fe_{1-x}Co_x)_2As_2$ single crystals. *Phys. Rev. B*, 78:214515, Dec 2008.

[199] S. L. Bud'ko, N. Ni, S. Nandi, G. M. Schmiedeshoff, and P. C. Canfield. Thermal expansion and anisotropic pressure derivatives of T_c in $Ba(Fe_{1-x}Co_x)_2As_2$ single crystals. *Phys. Rev. B*, 79:054525, Feb 2009.

[200] Bin Zeng, Bing Shen, Huiqian Luo, Gang Mu, Peng Cheng, Huan Yang, Lei Shan, Cong Ren, and Hai-Hu Wen. Specific heat of optimally doped $Ba(Fe_{1-x}TM_x)_2As_2$ (TM= Co and Ni) single crystals at low temperatures: A multiband fitting. *Phys. Rev. B*, 85:224514, Jun 2012.

[201] Yasuyuki Nakajima, Toshihiro Taen, and Tsuyoshi Tamegai. Possible superconductivity above 25 K in single-crystalline Co-doped $BaFe_2As_2$. *Journal of the Physical Society of Japan*, 78(2):023702, 2009.

[202] Lei Fang, Huiqian Luo, Peng Cheng, Zhaosheng Wang, Ying Jia, Gang Mu, Bing Shen, I. I. Mazin, Lei Shan, Cong Ren, and Hai-Hu Wen.

Roles of multiband effects and electron-hole asymmetry in the superconductivity and normal-state properties of $Ba(Fe_{1-x}Co_x)_2As_2$. *Phys. Rev. B*, 80:140508, Oct 2009.

[203] Yong Liu and Thomas A. Lograsso. Crossover in the magnetic response of single-crystalline $Ba_{1-x}K_xFe_2As_2$ and lifshitz critical point evidenced by Hall effect measurements. *Phys. Rev. B*, 90:224508, Dec 2014.

[204] Jack Gillett, Sitikantha D Das, Paul Syers, Alison KT Ming, Jose I Espeso, Chiara M Petrone, and Suchitra E Sebastian. Dimensional tuning of the magnetic-structural transition in $A(Fe_{1-x}Co_x)_2As_2$ (A= Sr, Ba). *arXiv:1005.1330*, 2010.

[205] Jun Sung Kim, Seunghyun Khim, Liqin Yan, N Manivannan, Yong Liu, Ingyu Kim, GR Stewart, and Kee Hoon Kim. Evidence for coexistence of superconductivity and magnetism in single crystals of Co-doped $SrFe_2As_2$. *Journal of Physics: Condensed Matter*, 21(10):102203, 2009.

[206] W. T. Jin, Y. Xiao, Z. Bukowski, Y. Su, S. Nandi, A. P. Sazonov, M. Meven, O. Zaharko, S. Demirdis, K. Nemkovski, K. Schmalzl, Lan Maria Tran, Z. Guguchia, E. Feng, Z. Fu, and Th. Brückel. Phase diagram of Eu magnetic ordering in Sn-flux-grown $Eu(Fe_{1-x}Co_x)_2As_2$ single crystals. *Phys. Rev. B*, 94:184513, Nov 2016.

[207] W. T. Jin, S. Nandi, Y. Xiao, Y. Su, O. Zaharko, Z. Guguchia, Z. Bukowski, S. Price, W. H. Jiao, G. H. Cao, and Th. Brückel. Magnetic structure of superconducting $Eu(Fe_{0.82}Co_{0.18})_2As_2$ as revealed by single-crystal neutron diffraction. *Phys. Rev. B*, 88:214516, Dec 2013.

[208] Mahmoud Abdel-Hafiez, Yuanyuan Zhang, Zheng He, Jun Zhao, Christoph Bergmann, Cornelius Krellner, Chun-Gang Duan, Xingye Lu, Huiqian Luo, Pengcheng Dai, and Xiao-Jia Chen. Nodeless superconductivity in the presence of spin-density wave in pnictide superconductors: The case of $BaFe_{2-x}Ni_xAs_2$. *Phys. Rev. B*, 91:024510, Jan 2015.

[209] A. Thaler, N. Ni, A. Kracher, J. Q. Yan, S. L. Bud'ko, and P. C. Canfield. Physical and magnetic properties of $Ba(Fe_{1-x}Ru_x)_2as_2$ single crystals. *Phys. Rev. B*, 82:014534, Jul 2010.

[210] Yusuke Nakai, Tetsuya Iye, Shunsaku Kitagawa, Shigeru Ishida, Kenji and, Takasada Shibauchi, Yuji Matsuda, and Takahito

Terashima. ^{31}P and ^{75}As NMR evidence for a residual density of states at zero energy in superconducting $BaFe_2(As_{0.67}P_{0.33})_2$. *Phys. Rev. B*, 81:020503, Jan 2010.

[211] Tatsuya Kobayashi, Shigeki Miyasaka, Setsuko Tajima, and Noriko Chikumoto. Electronic phase diagram of $SrFe_2(As_{1-x}P_x)_2$: Effect of structural dimensionality. *Journal of the Physical Society of Japan*, 83(10):104702, 2014.

[212] Marianne Rotter, Michael Pangerl, Marcus Tegel, and Dirk Johrendt. Superconductivity and crystal structures of $(Ba_{1-x}K_x)Fe_2As_2$ (x=0-1). *Angewandte Chemie International Edition*, 47(41):7949–7952.

[213] S. Avci, O. Chmaissem, D. Y. Chung, S. Rosenkranz, E. A. Goremychkin, J. P. Castellan, I. S. Todorov, J. A. Schlueter, H. Claus, A. Daoud-Aladine, D. D. Khalyavin, M. G. Kanatzidis, and R. Osborn. Phase diagram of $Ba_{1-x}K_xFe_2As_2$. *Phys. Rev. B*, 85:184507, May 2012.

[214] L M Wang, Chih-Yi Wang, Un-Cheong Sou, H C Yang, L J Chang, Caleb Redding, Yu Song, Pengcheng Dai, and Chenglin Zhang. Longitudinal and transverse Hall resistivities in $NaFe_{1-x}Co_xAs$ single crystals with x=0.022 and 0.0205: weak pinning and anomalous electrical transport properties. *Journal of Physics: Condensed Matter*, 25(39):395702, 2013.

[215] Luminita Harnagea, Giri Mani, Rohit Kumar, and Surjeet Singh. Magnetic disorder and gap symmetry in the optimally electron-doped $Sr(Fe,Co)_2As_2$ superconductor. *Phys. Rev. B*, 97:054514, Feb 2018.

[216] W. Z. Hu, J. Dong, G. Li, Z. Li, P. Zheng, G. F. Chen, J. L. Luo, and N. L. Wang. Origin of the spin density wave instability in AFe_2As_2 $(A = \mathrm{Ba}, \mathrm{Sr})$ as revealed by optical spectroscopy. *Phys. Rev. Lett.*, 101:257005, Dec 2008.

[217] V. Brouet, Ping-Hui Lin, Y. Texier, J. Bobroff, A. Taleb-Ibrahimi, P. Le Fèvre, F. Bertran, M. Casula, P. Werner, S. Biermann, F. Rullier-Albenque, A. Forget, and D. Colson. Large temperature dependence of the number of carriers in Co-doped $BaFe_2As_2$. *Phys. Rev. Lett.*, 110:167002, Apr 2013.

[218] H. Wadati, I. Elfimov, and G. A. Sawatzky. Where are the extra d electrons in transition-metal-substituted iron pnictides? *Phys. Rev. Lett.*, 105:157004, Oct 2010.

[219] L. B. Ioffe and A. J. Millis. Zone-diagonal-dominated transport in high-T_c cuprates. *Phys. Rev. B*, 58:11631–11637, Nov 1998.

[220] N.E. Hussey. The normal state scattering rate in high- cuprates. *The European Physical Journal B - Condensed Matter and Complex Systems*, 31(4):495–507, Feb 2003.

[221] Hilbert v. Löhneysen, Achim Rosch, Matthias Vojta, and Peter Wölfle. Fermi-liquid instabilities at magnetic quantum phase transitions. *Rev. Mod. Phys.*, 79:1015–1075, Aug 2007.

[222] A. E. Koshelev. Magnetotransport of multiple-band nearly antiferromagnetic metals due to hot-spot scattering. *Phys. Rev. B*, 94:125154, Sep 2016.

[223] Rafael M. Fernandes, Elihu Abrahams, and Jörg Schmalian. Anisotropic in-plane resistivity in the nematic phase of the iron pnictides. *Phys. Rev. Lett.*, 107:217002, Nov 2011.

[224] Maxim Breitkreiz, P. M. R. Brydon, and Carsten Timm. Resistive anisotropy due to spin-fluctuation scattering in the nematic phase of iron pnictides. *Phys. Rev. B*, 90:121104, Sep 2014.

[225] Y. Nakajima, K. Izawa, Y. Matsuda, K. Behnia, H. Kontani, M. Hedo, Y. Uwatoko, T. Matsumoto, H. Shishido, R. Settai, and Y. Onuki. Evolution of Hall coefficient in two-dimensional heavy fermion cecoin5. *Journal of the Physical Society of Japan*, 75(2):023705, 2006.

[226] Yasushi Abe, Yoichi Ando, J. Takeya, H. Tanabe, T. Watauchi, I. Tanaka, and H. Kojima. Normal-state magnetotransport in $La_{1.905}Ba_{0.095}CuO_4$ single crystals. *Phys. Rev. B*, 59:14753–14756, Jun 1999.

[227] Z Konstantinovic, O Laborde, P Monceau, ZZ Li, and H Raffy. Normal state magnetoresistance in $Bi_2Sr_2CaCu_2O_{8+\delta}$ thin films with different oxygen contents. *Physica B: Condensed Matter*, 259:569–570, 1999.

[228] I. Kokanović, J. R. Cooper, S. H. Naqib, R. S. Islam, and R. A. Chakalov. Effect of zn substitution on the normal-state magnetoresistivity of epitaxial $Y_{0.95}Ca_{0.05}Ba_2(Cu_{1-x}Znx_x)_3O_y$ and $Y_{0.9}Ca_{0.1}Ba_2Cu_3O_y$ films. *Phys. Rev. B*, 73:184509, May 2006.

[229] Yoichi Ando and T. Murayama. Nonuniversal power law of the Hall scattering rate in a single-layer cuprate $Bi_2Sr_{2-x}La_xCuO_6$. *Phys. Rev. B*, 60:R6991–R6994, Sep 1999.

[230] Chiheng Dong, Hangdong Wang, Zujuan Li, Jian Chen, H. Q. Yuan, and Minghu Fang. Revised phase diagram for the $FeTe_{1-x}Se_x$ system with fewer excess Fe atoms. *Phys. Rev. B*, 84:224506, Dec 2011.

[231] V. Cvetkovic and Z. Tesanovic. Multiband magnetism and superconductivity in fe-based compounds. *EPL (Europhysics Letters)*, 85(3):37002, 2009.

[232] Yu Shun-Li and Li Jian-Xin. Spin fluctuations and unconventional superconducting pairing in iron-based superconductors. *Chinese Physics B*, 22(8):087411, 2013.

[233] M. A. Tanatar, N. Ni, A. Thaler, S. L. Bud'ko, P. C. Canfield, and R. Prozorov. Pseudogap and its critical point in the heavily doped $Ba(Fe_{1-x}Co_x)_2As_2$ from c-axis resistivity measurements. *Phys. Rev. B*, 82:134528, Oct 2010.

[234] Paul C Canfield and Sergey L Bud'Ko. FeAs-based superconductivity: a case study of the effects of transition metal doping on $BaFe_2As_2$. *Annu. Rev. Condens. Matter Phys.*, 1(1):27–50, 2010.

[235] Ross H. McKenzie, J. S. Qualls, S. Y. Han, and J. S. Brooks. Violation of Kohler's rule by the magnetoresistance of a quasi-two-dimensional organic metal. *Phys. Rev. B*, 57:11854–11857, May 1998.

[236] Stephen D. Wilson, Z. Yamani, C. R. Rotundu, B. Freelon, P. N. Valdivia, E. Bourret-Courchesne, J. W. Lynn, Songxue Chi, Tao Hong, and R. J. Birgeneau. Antiferromagnetic critical fluctuations in $BaFe_2As_2$. *Phys. Rev. B*, 82:144502, Oct 2010.

[237] Y Sekiba, T Sato, K Nakayama, K Terashima, P Richard, J H Bowen, H Ding, Y-M Xu, L J Li, G H Cao, Z-A Xu, and T Takahashi. Electronic structure of heavily electron-doped $BaFe_{1.7}Co_{0.3}As_2$ studied by angle-resolved photoemission. *New Journal of Physics*, 11(2):025020, 2009.

[238] K. Prokeš, S. Mat'aš, L. Harnagea, S. Singh, S. Wurmehl, D. N. Argyriou, and B. Büchner. Effect of Co substitution on the magnetic order in $Ca(Fe_{1-x}Co_x)_2As_2$ single crystals studied by neutron diffraction. *Phys. Rev. B*, 83:104414, Mar 2011.

[239] M. G. Kim, R. M. Fernandes, A. Kreyssig, J. W. Kim, A. Thaler, S. L. Bud'ko, P. C. Canfield, R. J. McQueeney, J. Schmalian, and A. I. Goldman. Character of the structural and magnetic phase transitions

in the parent and electron-doped $BaFe_2As_2$ compounds. *Phys. Rev. B*, 83:134522, Apr 2011.

[240] Zhi Ren, Qian Tao, Shuai Jiang, Chunmu Feng, Cao Wang, Jianhui Dai, Guanghan Cao, and Zhu'an Xu. Superconductivity induced by phosphorus doping and its coexistence with ferromagnetism in $EuFe_2(As_{0.7}P_{0.3})_2$. *Phys. Rev. Lett.*, 102:137002, Apr 2009.

[241] Shuai Jiang, Yongkang Luo, Zhi Ren, Zengwei Zhu, Cao Wang, Xiangfan Xu, Qian Tao, Guanghan Cao, and Zhu'an Xu. Metamagnetic transition in $EuFe_2As_2$ single crystals. *New Journal of Physics*, 11(2):025007, 2009.

[242] Wen-He Jiao, Qian Tao, Jin-Ke Bao, Yun-Lei Sun, Chun-Mu Feng, Zhu-An Xu, I. Nowik, I. Felner, and Guang-Han Cao. Anisotropic superconductivity in $Eu(Fe_{0.75}Ru_{0.25})_2As_2$ ferromagnetic superconductor. *EPL (Europhysics Letters)*, 95(6):67007, 2011.

[243] Zhi Ren, Xiao Lin, Qian Tao, Shuai Jiang, Zengwei Zhu, Cao Wang, Guanghan Cao, and Zhu'an Xu. Suppression of spin-density-wave transition and emergence of ferromagnetic ordering of Eu^{+2} moments in $EuFe_{2-x}Ni_xAs_2$. *Phys. Rev. B*, 79:094426, Mar 2009.

[244] Vinh Hung Tran, Zbigniew Bukowski, Lan Maria Tran, and Andrzej J Zaleski. The electronic phase diagrams of the $Eu(Fe_{0.81}Co_{0.19})_2As_2$ superconductor. *New Journal of Physics*, 14(7):073052, 2012.

[245] H. S. Jeevan, Deepa Kasinathan, Helge Rosner, and Philipp Gegenwart. Interplay of antiferromagnetism, ferromagnetism, and superconductivity in $EuFe_2(As_{1-x}P_x)_2$ single crystals. *Phys. Rev. B*, 83:054511, Feb 2011.

[246] C. F. Miclea, M. Nicklas, H. S. Jeevan, D. Kasinathan, Z. Hossain, H. Rosner, P. Gegenwart, C. Geibel, and F. Steglich. Evidence for a reentrant superconducting state in $EuFe_2As_2$ under pressure. *Phys. Rev. B*, 79:212509, Jun 2009.

[247] Taichi Terashima, Motoi Kimata, Hidetaka Satsukawa, Atsushi Harada, Kaori Hazama, Shinya Uji, Hiroyuki S. Suzuki, Takehiko Matsumoto, and Keizo Murata. $EuFe_2As_2$ under high pressure: An antiferromagnetic bulk superconductor. *Journal of the Physical Society of Japan*, 78(8):083701, 2009.

[248] Nobuyuki Kurita, Motoi Kimata, Kota Kodama, Atsushi Harada, Megumi Tomita, Hiroyuki S. Suzuki, Takehiko Matsumoto, Keizo Murata, Shinya Uji, and Taichi Terashima. Phase diagram of pressure-induced superconductivity in $EuFe_2As_2$ probed by high-pressure resistivity up to 3.2 GPa. *Phys. Rev. B*, 83:214513, Jun 2011.

[249] Marianne Rotter, Christine Hieke, and Dirk Johrendt. Different response of the crystal structure to isoelectronic doping in $BaFe_2(As_{1-x}P_x)_2$ and $(Ba_{1-x}Sr_x)Fe_2As_2$. *Phys. Rev. B*, 82:014513, Jul 2010.

[250] Georgiy M Tsoi, Walter Malone, Walter Uhoya, Jonathan E Mitchell, Yogesh K Vohra, Lowell E Wenger, Athena S Sefat, and S T Weir. Pressure-induced superconductivity in $Ba_{0.5}Sr_{0.5}Fe_2As_2$. *Journal of Physics: Condensed Matter*, 24(49):495702, 2012.

[251] J. R. Jeffries, N. P. Butch, M. J. Lipp, J. A. Bradley, K. Kirshenbaum, S. R. Saha, J. Paglione, C. Kenney-Benson, Y. Xiao, P. Chow, and W. J. Evans. Persistent Fe moments in the normal-state collapsed-tetragonal phase of the pressure-induced superconductor $Ca_{0.67}Sr_{0.33}Fe_2As_2$. *Phys. Rev. B*, 90:144506, Oct 2014.

[252] Jonathan E. Mitchell, Bayrammurad Saparov, Wenzhi Lin, Stuart Calder, Qing Li, Sergei V. Kalinin, Minghu Pan, Andrew D. Christianson, and Athena S. Sefat. Temperature-composition phase diagrams for $Ba_{1-x}Sr_xFe_2As_2$ ($0\leq$ x $\leq$ 1) and superconducting $Ba_{0.5}Sr_{0.5}(Fe_{1-y}Co_y)_2As_2$ ($0\leq y \leq 0.141$). *Phys. Rev. B*, 86:174511, Nov 2012.

[253] S. Knöner, E. Gati, S. Köhler, B. Wolf, U. Tutsch, S. Ran, M. S. Torikachvili, S. L. Bud'ko, P. C. Canfield, and M. Lang. Combined effects of Sr substitution and pressure on the ground states in $CaFe_2As_2$. *Phys. Rev. B*, 94:144513, Oct 2016.

[254] S R Saha, K Kirshenbaum, N P Butch, J Paglione, and P Y Zavalij. Uniform chemical pressure effect in solid solutions $Ba_{1-x}Sr_xFe_2As_2$ and $Sr_{1-x}Ca_xFe_2As_2$. *Journal of Physics: Conference Series*, 273(1):012104, 2011.

[255] K. Kirshenbaum, N. P. Butch, S. R. Saha, P. Y. Zavalij, B. G. Ueland, J. W. Lynn, and J. Paglione. Tuning magnetism in FeAs-based materials via a tetrahedral structure. *Phys. Rev. B*, 86:060504, Aug 2012.

[256] P. F. S. Rosa, C. Adriano, W. Iwamoto, T. M. Garitezi, T. Grant, Z. Fisk, and P. G. Pagliuso. Evolution of Eu^{+2} spin dynamics in $Ba_{1-x}Eu_xFe_2As_2$. *Phys. Rev. B*, 86:165131, Oct 2012.

[257] A Mitsuda, S Seike, T Matoba, H Wada, F Ishikawa, and Y Yamada. Competition between Fe-based superconductivity and antiferromagnetism of Eu^{+2} in $Eu_{1-x}Ca_xFe_2As_2$. *Journal of Physics: Conference Series*, 273(1):012100, 2011.

[258] Javier Herrero-Martín, Valerio Scagnoli, Claudio Mazzoli, Yixi Su, Ranjan Mittal, Yinguo Xiao, Thomas Brueckel, Neeraj Kumar, S. K. Dhar, A. Thamizhavel, and Luigi Paolasini. Magnetic structure of $EuFe_2As_2$ as determined by resonant X-ray scattering. *Phys. Rev. B*, 80:134411, Oct 2009.

[259] Y. Xiao, Y. Su, M. Meven, R. Mittal, C. M. N. Kumar, T. Chatterji, S. Price, J. Persson, N. Kumar, S. K. Dhar, A. Thamizhavel, and Th. Brueckel. Magnetic structure of $EuFe_2As_2$ determined by single-crystal neutron diffraction. *Phys. Rev. B*, 80:174424, Nov 2009.

[260] Y. Xiao, Y. Su, W. Schmidt, K. Schmalzl, C. M. N. Kumar, S. Price, T. Chatterji, R. Mittal, L. J. Chang, S. Nandi, N. Kumar, S. K. Dhar, A. Thamizhavel, and Th. Brueckel. Field-induced spin reorientation and giant spin-lattice coupling in $EuFe_2As_2$. *Phys. Rev. B*, 81:220406, Jun 2010.

[261] Luminita Harnagea, Rohit Kumar, Surjeet Singh, S Wurmehl, Anja U B Wolter, and B Bchner. Evolution of the magnetic order of Fe and Eu sublattices in $Eu_{1-x}Ca_xFe_2As_2$ ($0 \leq x \leq 1$) single crystals. *Journal of Physics: Condensed Matter*, 30(41):415601, 2018.

[262] S. Blundell. *Magnetism in Condensed Matter*. Oxford Master Series in Condensed Matter Physics. OUP Oxford, 2001.

[263] Z. Guguchia, J. Roos, A. Shengelaya, S. Katrych, Z. Bukowski, S. Weyeneth, F. Murányi, S. Strässle, A. Maisuradze, J. Karpinski, and H. Keller. Strong coupling between Eu^{+2} spins and Fe_2As_2 layers in $EuFe_{1.9}Co_{0.1}As_2$ observed with NMR. *Phys. Rev. B*, 83:144516, Apr 2011.

[264] P Marra, A Nigro, Z Li, G F Chen, N L Wang, J L Luo, and C Noce. Paraconductivity of the K-doped $SrFe_2As_2$ superconductor. *New Journal of Physics*, 14(4):043001, 2012.

[265] A L Solovjov, L V Omelchenko, A V Terekhov, K Rogacki, R V Vovk, E P Khlybov, and A Chroneos. Fluctuation conductivity and possible pseudogap state in FeAs-based superconductor $EuFeAsO_{0.85}F_{0.15}$. *Materials Research Express*, 3(7):076001, 2016.

[266] D Ahmad, Y I Seo, W J Choi, and Yong Seung Kwon. Fluctuation-induced magnetoconductivity in pristine and proton-irradiated $Ca_{8.5}La_{1.5}(Pt_3As_8)(Fe_2As_2)_5$ single crystals. *Superconductor Science and Technology*, 30(2):025009, 2017.

[267] Kouichi Semba and Azusa Matsuda. Vanishingly small maki-thompson superconducting fluctuation in the magnetoresistance of high-T_C superconductors. *Phys. Rev. B*, 55:11103–11106, May 1997.

[268] W. Lang, G. Heine, P. Schwab, X. Z. Wang, and D. Bäuerle. Paraconductivity and excess Hall effect in epitaxial $YBa_2Cu_3O_7$ films induced by superconducting fluctuations. *Phys. Rev. B*, 49:4209–4217, Feb 1994.

[269] W. Holm, Yu. Eltsev, and Ö. Rapp. Paraconductivity along the a and b axes in $YBa_2Cu_3O_{7-\delta}$ single crystals. *Phys. Rev. B*, 51:11992–11995, May 1995.

[270] E M M Ibrahim and S A Saleh. Influence of sintering temperature on excess conductivity in Bi-2223 superconductors. *Superconductor Science and Technology*, 20(7):672, 2007.

[271] Wu Liu, T. W. Clinton, A. W. Smith, and C. J. Lobb. Hall-conductivity sign reversal and fluctuations in $YBa_2Cu_3O_{7-\delta}$ films. *Phys. Rev. B*, 55:11802–11805, May 1997.

[272] P K Nayak and S Ravi. Excess conductivity and magneto-conductivity studies in pure and Ag-doped $(La_{1-x}Y_x)_2Ba_2CaCu_5O_z$ superconductors. *Superconductor Science and Technology*, 19(11):1209, 2006.

[273] A. Wahl, D. Thopart, G. Villard, A. Maignan, Ch. Simon, J. C. Soret, L. Ammor, and A. Ruyter. Magnetotransport in $Bi_2Sr_2Ca_{1-x}Y_xCu_2O_{8+\delta}$ single crystals: From the underdoped to the overdoped regime. *Phys. Rev. B*, 60:12495–12501, Nov 1999.

[274] Yoichi Ando and Kouji Segawa. Magnetoresistance of untwinned $YBa_2Cu_3O_y$ single crystals in a wide range of doping: Anomalous hole-doping dependence of the coherence length. *Phys. Rev. Lett.*, 88:167005, Apr 2002.

[275] Akira Iyo, Kenji Kawashima, Tatsuya Kinjo, Taichiro Nishio, Shigeyuki Ishida, Hiroshi Fujihisa, Yoshito Gotoh, Kunihiro Kihou, Hiroshi Eisaki, and Yoshiyuki Yoshida. New-structure-type Fe-based superconductors: $CaAFe_4As_4$ (A = K, Rb, Cs) and $SrAFe_4As_4$ (A = Rb, Cs). *Journal of the American Chemical Society*, 138(10):3410–3415, 2016. PMID: 26943024.

[276] W. R. Meier, T. Kong, U. S. Kaluarachchi, V. Taufour, N. H. Jo, G. Drachuck, A. E. Böhmer, S. M. Saunders, A. Sapkota, A. Kreyssig, M. A. Tanatar, R. Prozorov, A. I. Goldman, Fedor F. Balakirev, Alex Gurevich, S. L. Bud'ko, and P. C. Canfield. Anisotropic thermodynamic and transport properties of single-crystalline $CaKFe_4As_4$. *Phys. Rev. B*, 94:064501, Aug 2016.

List of Publications

1. Scaling of magnetotransport in the $Ba(Fe_{1-x}Co_x)_2As_2$ series
Rohit Kumar, Surjeet Singh and, Sunil Nair
J. Phys.: Condens. Matter **31** (2019) 115601

2. Magnetotransport studies of optimally doped $Sr(Fe_{1-x}Co_x)_2As_2$
Rohit Kumar, Luminita Harnagea, Archana Lakhani and Sunil Nair
J. Phys.: Condens. Matter **30** (2018) 505601

3. Evolution of the magnetic order of Fe and Eu sublattices in $Eu_{1-x}Ca_xFe_2As_2$ $(0 \leq x \leq 1)$ single crystals
Luminita Harnagea, **Rohit Kumar**, Surjeet Singh, S Wurmehl, Anja U B Wolter and B Büchner
J. Phys.: Condens. Matter **30** (2018) 415601

4. Magnetic disorder and gap symmetry in the optimally electron doped $Sr(Fe, Co)_2As_2$ superconductor
Luminita Harnagea, Giri Mani, **Rohit Kumar**, and Surjeet Singh
Physical Review B **97**, 054514 (2018)